THESIS

A PLASTIC TOTAL INTERNAL REFLECTION-BASED PHOTOLUMINESCENCE DEVICE FOR ENZYMATIC BIOSENSORS

Submitted by

Ishan G. Thakkar

Department of Electrical and Computer Engineering

In partial fulfillment of the requirements

For the Degree of Master of Science

Colorado State University

Fort Collins, Colorado

Spring 2013

Master's Committee:

Advisor: Kevin L. Lear

Kenneth Reardon
George Collins

ABSTRACT

A PLASTIC TOTAL INTERNAL REFLECTION-BASED PHOTOLUMINESCENT DEVICE FOR ENZYMATIC BIOSENSORS

Growing concerns for quality of water, food and beverages in developing and developed countries drive sizeable markets for mass-producible, low cost devices that can measure the concentration of contaminant chemicals in water, food, and beverages rapidly and accurately. Several fiber-optic enzymatic biosensors have been reported for these applications, but they exhibit very strong presence of scattered excitation light in the signal for sensing, requiring expensive thin-film filters, and their non-planar structure makes them challenging to mass-produce. Several other planar optical waveguide-based biosensors prove to be relatively costly and more fragile due to constituent materials and the techniques involved in their fabrication. So, a plastic total internal reflection (TIR)-based low cost, low scatter, field-portable device for enzymatic biosensors is fabricated and demonstrated.

The design concept of the TIR-based photoluminescent enzymatic biosensor device is explained. An analysis of economical materials with appropriate optical and chemical properties is presented. PMMA and PDMS are found to be appropriate due to their high chemical resistance, low cost, high optical transmittance and low auto-fluorescence. The techniques and procedures used for device fabrication are discussed. The device incorporated a PMMA-based optical waveguide core and PDMS-based fluid cell with simple multi-mode fiber-optics using cost-effective fabrication techniques like molding and surface modification.

Several techniques of robustly depositing photoluminescent dyes on PMMA core surface are discussed. A pH-sensitive fluorescent dye, fluoresceinamine, and an O_2-sensitive

phosphorescent dye, Ru(dpp) both are successfully deposited using Si-adhesive gel-based as well as HydroThane-based deposition methods. Two different types of pH-sensors using two different techniques of depositing fluoresceinamine are demonstrated. Also, the effect of concentration of fluoresceinamine-dye molecules on fluorescence intensity and scattered excitation light intensity is investigated. The fluorescence intensity to the scattered excitation light intensity ratio for dye deposition is found to increase with increase in concentration. However, both the absolute fluorescence intensity and absolute scatter intensity are found to decrease in different amounts with an increase in concentration.

An enzymatic hydrogen peroxide (H_2O_2) sensor is made and demonstrated by depositing Ruthenium-based phosphorescent dye ($Ru(dpp)^3$) and catalase-enzyme on the surface of the waveguide core. The O_2-sensitive phosphorescence of $Ru(dpp)^3$ is used as a transduction signal and the catalase-enzyme is used as a bio-component for sensing. The H_2O_2 sensor exhibits a phosphorescence signal to scattered excitation light ratio of 100±18 without filtering. The unfiltered device demonstrates a detection limit of (2.20±0.6) µM with the linear range from 200µM to 20mM.

An enzymatic lactose sensor is designed and characterized using Si-adhesive gel based $Ru(dpp)^3$ deposition and oxidase enzyme. The lactose sensor exhibits the linear range of up to 0.8mM, which is too small for its application in industrial process control. So, a flow cell-based sensor device with a fluid reservoir is proposed and fabricated to increase the linear range of the sensor. Also, a multi-channel pH-sensor device with four channels is designed and fabricated for simultaneous sensing of multiple analytes.

ACKNOWLEDGEMENTS

I would like to thank my advisor Dr. Kevin L. Lear, for his enduring support and guidance through this great learning experience. I would like to gratefully acknowledge the support of the OptiEnz Sensors and Dr. Kenneth Reardon's research group without which none of this work would have been possible. Many thanks go to my committee members Dr. Kenneth Reardon and Dr. George Collins for their support and guidance while working on this project. Special thanks go to Dr. Brian Heinz and Dr. Jonathan Vickers for their invaluable guidance through very helpful discussions on various aspects of the project from the beginning till the end. I would like to thank the many Optoelectronics group members I have had the privilege of working with over the years. In particular, I would like to thank Iris Yi for introducing the key aspects of the project to me in the beginning. Gracious thanks to a member of Dr. David Dandy's research group Kelly for helping me use their plasma processing facility.

Most importantly, I would like to thank my family, without whose invaluable love and support I never would have finished.

TABLE OF CONTENTS

Chapter 1: Introduction

1.1 Motivation

Over the recent years, the resources of clean water have been increasingly contaminated due to careless dumping of pollutants near water reservoirs by several industries. Health concerns related to consumption of contaminated water are more aggravated in developing countries, where the principal resources of clean water are rivers, lakes and wells. It is because many communities in developing countries are unaware of the contamination and related hazards. A few individuals and communities that are aware of the contamination don't get access to clean water because the current laboratory based contamination measurement techniques are expensive and slow. It is envisioned that availability of clean water is to be a serious concern in near future [1]. According to the World Health Organization, nearly 1 billion people lack access to clean water today [2]. In Us and other developed countries, where the most of the communities are well aware of the contaminated water sites, many remediation schemes are implemented. But, these schemes are often haltered because of lack of information on contamination concentrations. The lack of information on contamination concentrations prevails due to expensive analysis techniques. Quality concerns for food and beverages are also high. Therefore, in developing and developed countries, there are sizeable markets for mass-producible devices that can measure the concentration of contaminant chemicals in water, food, and beverages, and that can do so rapidly, accurately, and inexpensively.

Over the last few years, a great surge of research activities focused on development of novel cost-effective and field-portable biosensors for real time measurements for environmental monitoring and bioprocess monitoring. Among them, enzymatic biosensors are very popular because of the availability of a large number of oxido-reductase enzymes which can act on sugars, amino acids, fatty acids, aldehydes, phenols etc. Many enzymatic biosensor designs

based on conductiometric transducers, potentiometric transducers, amperometric transducers, thermal transducers and based on fiber-optics have been reported [3]. Amongst them all, photoluminescence based fiber-optic biosensors have become particularly popular due to their flexibility and resistance to electric noise. These sensors use photoluminescent dye indicators as transducers and enzymes as bio-analytical component. But incorporating bio-analytical component and indicator dye into a fiber optic sensor becomes unwieldy due to the very small diameter of fibers and fabrication of such sensors demands for a great deal of skills which increases the labor cost. Moreover, these sensors exhibit very high excitation light interference enforcing the use of expensive optical rejection filters, increasing cost. So, there exists a need for mass-producible, low cost, low interference enzymatic biosensor devices which also exhibit the advantages of photoluminescence based fiber optic sensors.

Recently, total internal reflection (TIR) – based biosensors have attracted increasing attention due to the great reduction of background interference and suitability for studying biochemical kinetics near substrate surfaces. Several planar waveguide based TIR biosensors are reported [4, 5]. TIR-based biosensors incorporate optical components to properly direct the excitation light and fluidic channels for supplying reagents/analytes for sensing. Conventional TIR-based biosensors are made using micro-fabrication techniques with polymer/elastomer based fluidics and semiconductor/polymer based optics in general. Huang et al used photolithography and etching to fabricate on chip prisms to achieve efficient light coupling [6]. They used SU-8 to fabricate the waveguides and optics. Due to super hydrophobic nature of SU-8, it becomes very difficult to achieve firm irreversible immobilization of dye and enzyme on SU-8 surfaces. Whereas, Chronis et al used wet etching of Si and thin film deposition to fabricate mirror surfaces to launch the excitation light at desired incidence angle [7]. They used glass

material to make waveguides, which makes the device relatively costlier than fiber-optic system and it also makes the device less portable due to fragility of glass material.

So, the goal of the study is to develop a low cost, low noise enzymatic biosensor device using the total internal reflection (TIR) concept which also exhibits the advantages of photoluminescence based fiber optic sensors. For that, a plastic TIR-based photoluminescence sensing enzymatic biosensor device is made. PMMA based optical waveguide and PDMS based fluidics are developed with directly coupled fibers to simplify excitation and collection optics. The device is fabricated without using photolithography or etching but using relatively simpler fabrication techniques like molding of PDMS and surface modification of PMMA and PDMS to integrate the optics with fluidics. The device is a plastic TIR-based photoluminescence sensing device for enzymatic biosensors.

1.2 Overview of the chapters

In chapter 2, enzymatic biosensor related topics like photoluminescence, enzyme reaction, sensing scheme along with the total internal reflection concept for waveguides with plastic optical waveguides and evanescent field are discussed briefly. Chapter 3 reviews a few TIR-based fluorescence sensing devices available in literature. Chapter 4 discusses the design concept for the TIR-based enzymatic biosensor device with the quest for appropriate materials. Chapter 5 describes the unsuccessful and successful methods of firmly depositing a pH-sensitive dye (fluorescenamine) and an O_2-sensitive dye ($Ru(dpp)^3$) on the surface of the waveguide core. Chapter 6 elaborates fabrication of the plastic TIR-based device. Chapter 7 presents results for pH-sensors made by depositing pH-sensitive dye (fluorescenamine). Chapter 8 describes an enzymatic lactose sensor and hydrogen peroxide sensor made by using deposition of O_2-sensitive dye ($Ru(dpp)^3$). And chapter 9 talks about miscellaneous work on multichannel pH-sensor

design, wavelength dependence of quenching of $Ru(dpp)^3$ and the sensor design based on fluid reservoir and flow cell for analyte sensing in flowing medium.

References

[1] World Water Assesment Programme, "The United Nations World Water Development Report 3: Water in a Changing World," Paris, 2009.

[2] WHO, UN Children's Fund, "Progress on Drinking Water and Sanitation: Special Focus on Sanitation," UNICEF, New York, 2008.

[3] A. S. Bassi, D. Tang, E. Lee, J. X. Zhu and M. A. Bergougnou, "Biosensors in Environmental and Bioprocess Monitoring," *Food Technology and Biotechnology*, vol. 34, no. 1, pp. 9-22, 1996.

[4] G. L. Duveneck, M. Pawlak, D. Neuschafer, E. Bar, W. Budach, U. Pieles and M. Ehrat, *Sensors and Actuators*, vol. B38, no. 1-3, 1997.

[5] W. Budach, A. P. Abel, A. E. Bruno and D. Neuschafer, *Analytical Chemistry*, vol. 71, no. 16, 1999.

[6] S. H. Huang and F. G. Tseng, "Development of a monolithic total internal reflection-based biochip utilizing a microprism array for fluorescence sensing," *Jornal of Micromechanics and Microengineering*, vol. 15, pp. 2235-2242, 2005.

[7] N. Chronis and L. P. Lee, "Total internal reflection-based biochip utilizing a polymer-filled cavity with a micromirror sidewall," *Lab Chip*, vol. 4, pp. 125-130, 2004.

Chapter 2: Background

2.1 Introduction

This chapter provides background information on subjects related to this thesis. Section 2.2 is an introduction to photoluminescence and covers the differences between fluorescence and phosphorescence. Basic information regarding enzymes is covered in Section 2.3 to lay down a foundation for those unfamiliar with the subject. Section 2.4 provides introductory knowledge on the enzymatic biosensor indirect sensing scheme, which relies on two parts, indicators and corresponding biological components. Section 2.5 explains total internal reflection and evanescent field with respect to optical waveguides. Basic information on fiber optics is included in Section 2.6, to prepare the audience to better understand the fiber to waveguide coupling mechanism. Some of the information in this chapter is reproduced from the works of the previous masters degree students (Iris Yi and Sean Pieper) of our research group, who worked on fiber optics based enzymatic biosensors.

2.2 Photoluminescence

The information in this section is reproduced from Sean Pieper's work [1] : " The process, in which an electron is excited to a higher energy state by the absorption of a photon and upon relaxation of the electron back to the ground state another photon is emitted, is called photoluminescence [2]. Single photon absorption uses a single photon with sufficient energy to excite the electron itself with the resulting emitted photon being of a longer wavelength. Multi-photon absorption is where some number of photons at longer wavelengths are used to excite the electron. This technique requires these excitation photons to arrive simultaneously with the sum of their energies sufficient enough to raise an electron the higher excited state. This thesis focuses on single photon absorption with multi-photon absorption being beyond the scope of the discussion here.

There are two types of photoluminescence, which are fluorescence and phosphorescence. The mechanism by which the photons are emitted differentiates between these two types. Fluorescence is a singlet to singlet transition of electrons where the net spin (S) is zero and has a multiplicity of 1 (=2*S +1) for both the ground and excited states of the molecule. Fluorescence is characterized by a fast radiative recombination transition with decay lifetimes less than 10 ns and generally a small Stokes shift. One example of a fluorescent molecule commonly used in different applications is fluorescein. Figure 2.1 shows the absorption and emission spectra of fluorescein [3] which has a peak absorption wavelength of ~485 nm and a peak emission around wavelength of ~519 nm and has a decay lifetime of 3.7 ns [4].

Phosphorescence is where an electron is excited to a higher energy state, and then intersystem cooling alters its spin creating a triplet state resulting in a net spin of one and a multiplicity of 3. Since each state can only have one up and one down spin, an electron having the same spin as an electron at the ground state is forbidden to make this transition until presumably the excited electron changes its spin. This results in a long decay lifetime of more than 10 ns. The existence of a triplet state becomes more probable when the photoluminescent molecule is centered on a heavy metal [5] [6], which then allows for phosphorescent emission to occur via a triplet to singlet transition. Examples of such dyes are ruthenium based molecules and are discussed in more detail later. A general characteristic of phosphorescent molecules is their particular affinity to have their photoluminescent decay quenched by molecular oxygen.

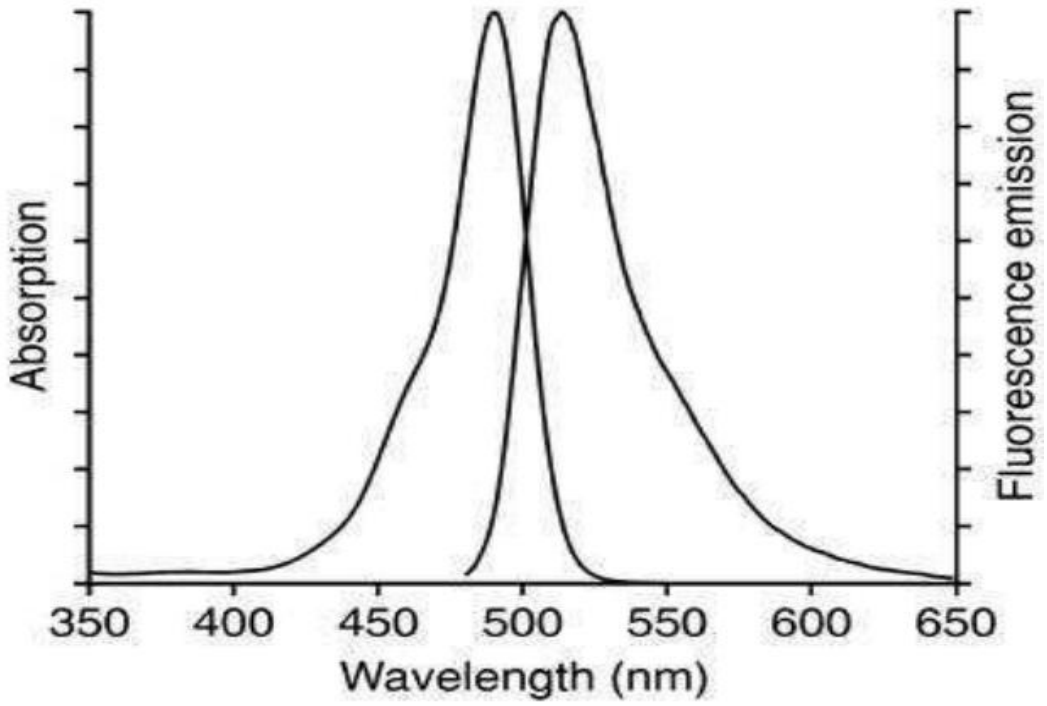

Figure 2.1, Absorption and emission spectrum of fluorescein at pH 9.0. Reproduced from Reference [3].

This is where instead of radiatively emitting from the triplet state the excited electron transfers to the oxygen molecule, non-radiatively transitions to a lower state, and then transfers back to the original molecule [5] [6]. This process follows the Stern-Volmer relationship expressed by the following equation [7],

$$I_0/I = \tau_0/\tau = 1 + K_{sv}[O_2] = 1 + k_q\tau_0[O_2] \ , \qquad (2.1)$$

where I_0 and τ_0 are the unquenched emission power (or often referred to as intensity) and decay lifetime respectively, I and τ are the quenched emission power and decay lifetime respectively, K_{SV} is the Stern-Volmer constant, k_q is the bimolecular quenching constant, and $[O_2]$ is the fractional gaseous O_2 concentration. Figure 2.2 illustrates the different paths a photoelectron can follow via a band diagram approach where a photoelectron is an electron that is excited from the

ground state to some higher energy level through the absorption of a photon with an appropriate amount of energy.

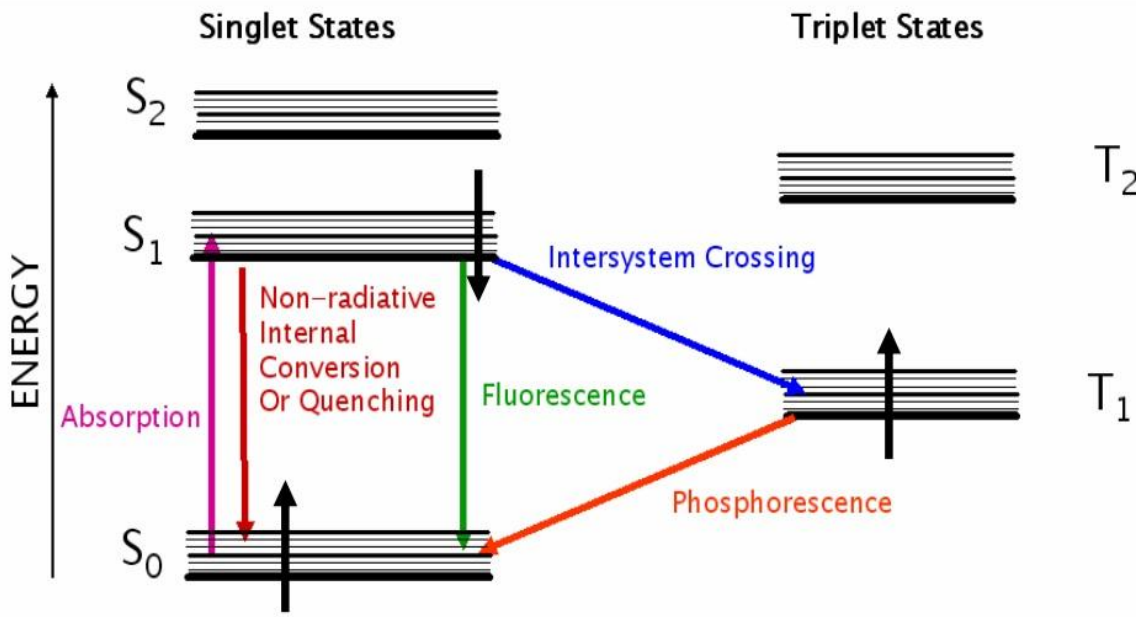

Figure 2.2, Representation of electron state transitions in a photoluminescent molecule. Shown are the different recombination paths for fluorescence and phosphorescence. Black arrows depict the spin of the electrons. Reproduced from [1]

Figure 2.3 illustrates excited electrons and an associated spin 4 where Fig. 2.3(a) represents the ground state, Figure 2.3(b) represents an excited condition with total spin of 0 and multiplicity of 1 which is favorable for singlet to singlet recombination called fluorescence shown in Figure 2.2, and Figure 2.3(c) represents an excited condition where the electron's spin is flipped due to intersystem crossing resulting in a total spin of 1and multiplicity of 3 and is referred to as a charge transfer to a triplet state. This process of an excited singlet state becoming a triplet state due to the excited electron's spin by intersystem crossing is also depicted in Figure 2.2. It is from this triplet state that phosphorescence occurs; the lower energy of phosphorescence photons in relation to fluorescence photons is due to the net spin causing the triplet state to be degenerate relative to the singlet state.

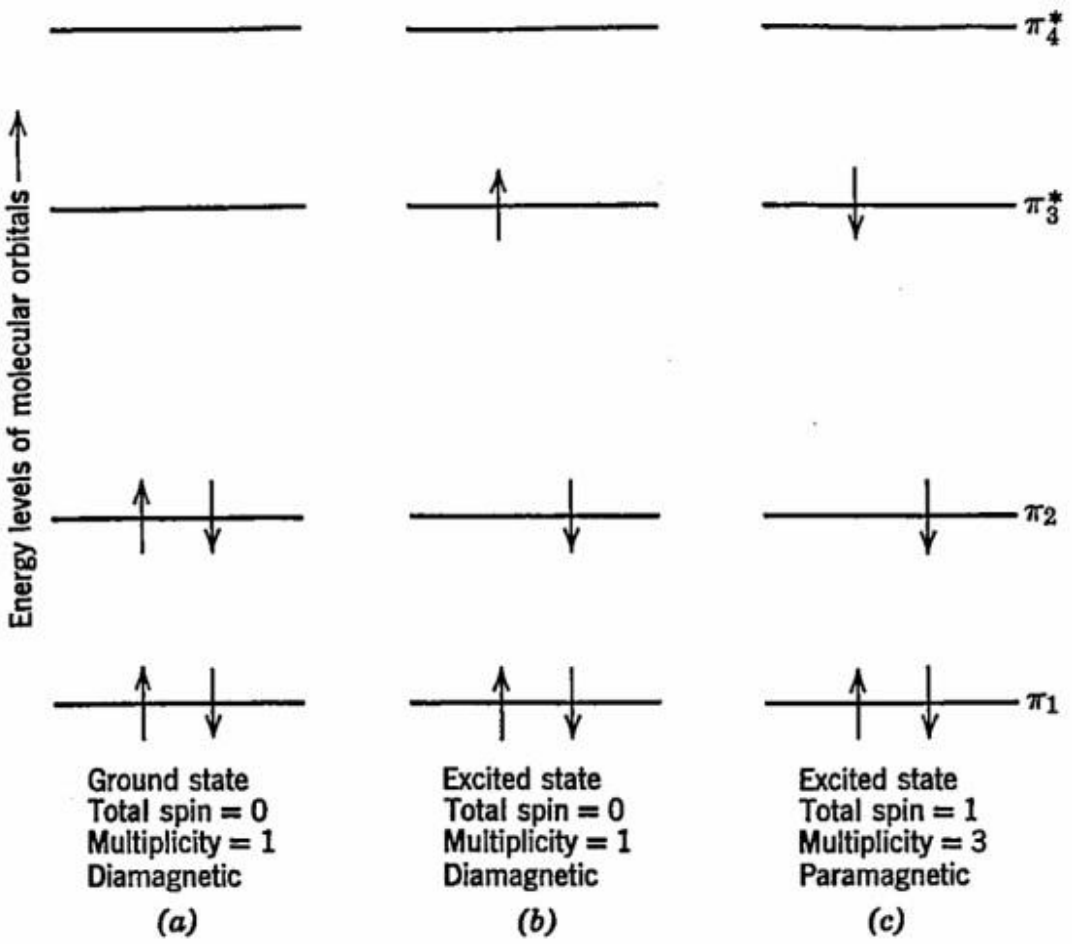

Figure 2.3, Simplified molecular band diagram including spin exhibiting (a) the molecules ground state and two possible excited states. (b) Shows a net spin of 0 and multiplicity of 1, a state that is favorable to fluorescence. (c) Shows a condition where the excited electron changed its spin resulting in the molecule to have a net spin of 1 and a multiplicity of 3. This state increases the probability of intersystem cooling to a triplet state and phosphorescent recombination occurring. Reproduced from Reference [4].

With the excited electron having the same spin as the ground state electron it is generally accepted that a transition of the excited electron down to the ground state is forbidden due to the Pauli Exclusion Principle where it is forbidden for two electrons to occupy the same energy state and have the same spin. Due to spin-orbit coupling [5] this transition can occur, presumably during this recombination the spin of the excited photoelectron flips so as not to violate the Pauli Exclusion Principle, resulting in the emission of a phosphorescent photon. It is of course possible for higher energy photons to be absorbed such that the excited electron will transition to a higher

state such as absorption by ultra-violet light for example and is beyond the scope of this discussion. Photoluminescence transitions occur with π electrons and not σ electrons within organic molecules. This is in part due to σ electrons forming the backbone bonds of a molecule and are typically very strong bonds [5]. Photons with sufficient energy to excite these electrons will break this bond in the molecule primarily resulting in photochemical degradation, or more plainly the molecule is broken and generally will no longer exhibit the same photoluminescent properties. This is sometimes referred to as photobleaching or photodegradation.

Molecules which will undergo photoluminescence are commonly referred to as a fluorophore or fluorochrome being defined as an organic molecule that is excited by one wavelength of light and emits a photon at a longer wavelength. This wavelength shift is referred to as the Stokes shift exhibited by the fluorophore. When dealing with phosphorescence is it very common to be have very low light levels as the radiative process is fairly inefficient. This can easily be seen when considering that ratio of the number of emitted photons to number of excitation photons absorbed to a singlet state, or quantum yield [5]. Looking at ruthenium complexes, quantum yields for tris(2,2'-bipyridyl) ruthenium(II) and tris(4,7-dipheny-l,10-phenanthroline) ruthenium (II) are 0.042 and 0.3 respectively [8]."

.2.3 Enzyme basics

This Section is an effort to provide information on the enzymatic portion of the associated research project that this thesis is part of. The intent is to give only a basic framework to the reader who is unfamiliar with enzymes and related biology. This section is reproduced from Sean Pieper's work: "An enzyme is a protein that catalyzes chemical reactions on some preferential molecule called a substrate [9] [10]. Here Escherichia coli (E. coli) bacteria are used for introducing the desired genetically engineered enzyme to the target environment. This is

accomplished by introducing an extra chromosomal circular deoxyribonucleic acid (DNA) called a plasmid placed inside the E. Coli cell and culturing a colony. A part of the plasmid is a election gene included to allow the bacteria to grow in the media of choice. This being useful when considering that the cell used may not be native to the environment it is being designed to exist in as part of the sensor system. Also included in this selection gene is coding for production of an antibiotic resisting substance. One other important component of the plasmid is coding that controls the timing of protein production for the introduced enzyme. Production control of the introduced enzyme is needed to ensure that other vital proteins needed for growth and sustainment of the E. Coli bacteria continue to be produced so that the cell remains alive as currently the desired reaction needs NADH which is provided by the E. Coli cell. Production of the extra proteins places the E. Coli cells that are desired at a growth disadvantage with respect to E. Coli cells that do not have the plasmid. This is where the antibiotic comes into play; introduction of gene coding that produces resistance to antibiotics during the culturing step can ensure that only E. Coli cells with the engineered plasmid exist in the cultured colony. Not taking steps to kill the E. Coli bacteria without the plasmid in the cell culture would result in the E. Coli bacteria with the plasmid being out competed resulting in a cell culture that would express very little of the desired traits introduced by the engineered enzyme contained with the plasmid. Identification of the different components of E. Coli cells are shown in Table 2.1 showing how the naming goes from general to more and more specific. Genes are noted as four italicized letter combinations with the first letter always being lower case. The protein this gene would encode is noted by the same four letter combination with the first letter being capitalized and not in italics, e.g. DhlA". Plasmid DNA sequence is noted by four letter combination with first letter always being lower case "p".

Table 2.1, Identification of the E. Coli bacteria cells with the engineered plasmid –gene for use as the biocomponent for monitoring of target pollutants in groundwater. Gene shown here is targeted for Toluene. Reproduced from [1]

Genus	**Species**	**Plasmid**	**Gene**
Escherichia	Coli	pAQN-	dhlA

The rate at which an enzyme catalyzes an analyte is described by the Michaelis-Menten kinetics equation shown here as,

$$r = k[E]\frac{[S]}{k_m + [S]} = V_{max}\frac{[S]}{k_m + [S]} \tag{2.2}$$

Where r is the reaction rate or reaction velocity, k is the reaction rate constant, K_m is the Michaelis-Menton rate constant, V_{max} is the maximum initial production rate of the product, [E] is the enzyme concentration, and [S] is the substrate concentration.

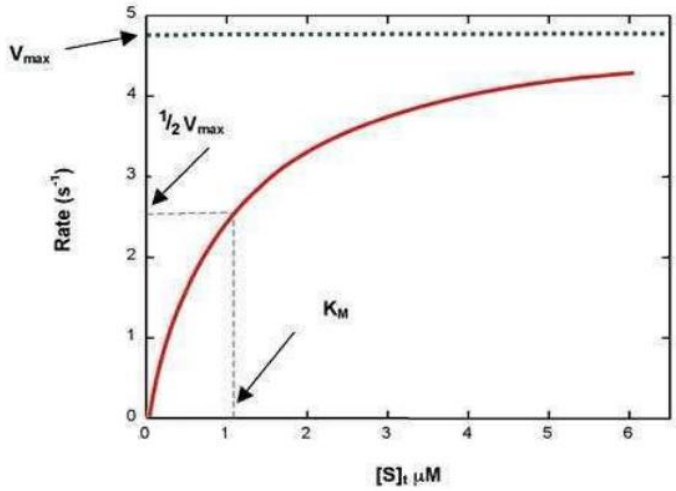

Figure 2.4, Simulated Michalis-Menton curve related the reaction rate between an enzyme and a target substrate. Reproduced from Reference [11].

Figure 2.4 illustrates an example of a simulated curve [11] of what this equation describes. Note that the point at which the equation equals $0.5V_{max}$ is the value of the Michailis-Menton rate constant K_m.

2.4 Optical sensing scheme

There are two optical sensing schemes in chemical sensors and biosensors, direct and indirect sensing. In the first, the intrinsic optical properties of the analyte are measured, while in the second the optical properties, such as color, absorption or luminescence of an immobilized indicator dye, label, or optically detectable bioprobe is monitored [12]. The direct sensing scheme is beyond the scope of discussion in this thesis, and the indirect sensing scheme is briefly introduced here. An indirect sensing scheme often relies on luminophores as the indicator, and a biocomponent as the sensor. Luminophore is briefly defined as the material that emits photoluminescence (PL).

The PL emission intensity of some useful luminophores is inhibited by the quencher concentration in the adjacent environment. A quantitative definition of the relationship between the PL emission intensity and the quencher concentration is known as the Stern-Volmer equation. An illustrative explanation of the luminophores-quencher pair working mechanism is shown in Figure 2.5. Quencher's presence in the luminophores' near-by environment alters the PL efficiency of the luminophores, and as a result, higher quencher concentration decreases the associated PL emission under the constant excitation power.

In the sensing process, a biological component is often used to recognize the analyte's information. Typical components include enzymes, antibodies, oligonucleotides, and whole cells [12], and among those, enzymes are widely used. Enzymes are proteins that catalyze chemical reactions. Like all catalysts, enzymes work by lowering the activation energy for a reaction, thus dramatically increasing the rate of the reaction to equilibrium.

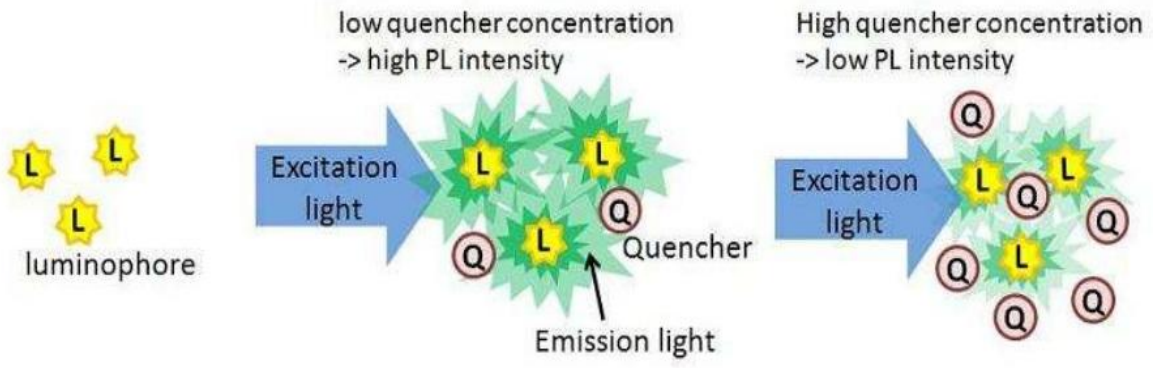

Figure 2.5, A simplified illustration of a luminophore-quencher pair working mechanism. The presence of the quencher in the adjacent environment of the luminophores alters the associated PL emission intensities under the same excitation intensity. Reproduced from [13]

As with all catalysts, enzymes are not consumed by the reactions they catalyze, nor do they alter the equilibrium of these reactions. However, enzymes do differ from most other catalysts by being much more specific [14]. With those properties, enzymes are an ideal candidate for analyte in-situ measurements. Genetically engineered enzymes can be designed to accelerate a reaction with the target analyte being one of the reactants, also known as substrates, and quencher as one of the products. With this mechanism, shown in Figure 2.6, a higher concentration of the analyte produces a higher concentration of quencher in the areas adjacent to the enzyme. An indirect analyte sensing scheme forms as the biocomponent, enzymes, works in conjunction with the luminophores. As shown in Figure 2.7, enzymatic reaction of the analytes produces quencher to inhibit PL efficiencyof the luminophores, and in this way the biosensor transduces the target analyte information into PL intensities. Therefore, by detecting the PL intensities from the luminophores we can tell how much analyte concentration there is in the area of interests.

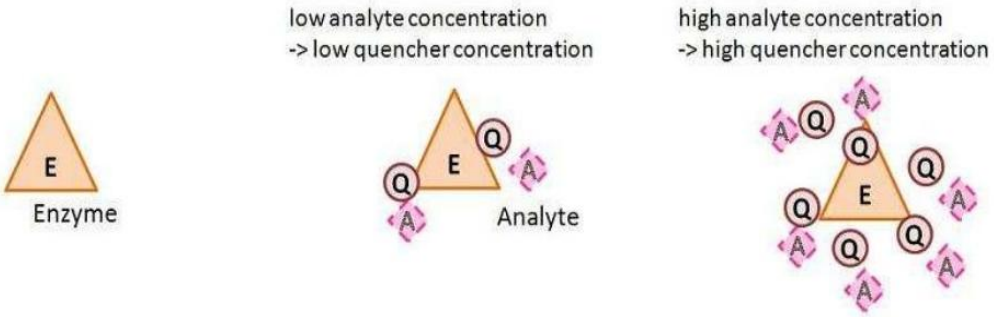

Figure 2.6, A simplified diagram of an enzymatic reaction with the target analyte being one of the substrates and quencher being one of the products. A higher analyte concentration in the enzyme adjacent areas results in a higher concentration of produced quencher. Reproduced from [13]

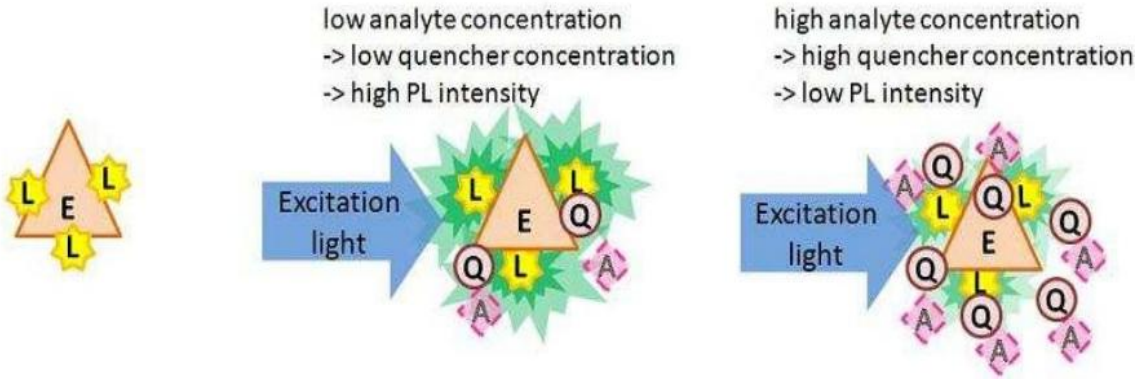

Figure 2.7, A simplified illustration of the indirect sensing scheme using the enzymatic biosensors working in conjunction with the luminophore-quencher pair. Reproduced from [13]

2.5 Total internal reflection and evanescent field

Axelrod et al [15] explained total internal reflection: "When a light beam propagating through a transparent medium 2 of high index of refraction (e.g., glass) encounters an interface with medium 1 of lower index of refraction (e.g., water), it undergoes total internal reflection for incidence angles (measured from the normal to the interface) greater than the "critical angle." The critical angle for TIR is given by

$$\theta_c = \sin^{-1} {}^{n_1}/_{n_2} = \sin^{-1} n \qquad (2.3)$$

Where n_1 and n_2 are the refractive indices of the medium 1 and the medium 2, respectively, and $n = n_1/n_2$ where $n < 1$ for TIR to occur. For incidence angle $\theta < \theta_c$ a portion of the light propagates through the interface with a refraction angle (also measured from the normal) given by Snell's law. (Some of the incident light internally reflects back into the solid.) For $\theta > \theta_c$, all of the light reflects back into the medium 2. However, even with TIR, some of the incident energy penetrates through the interface and propagates parallel to the surface in the plane of containing the incident and reflected rays. The field in the medium 1, called the "evanescent field" (or "wave"), is capable of exciting fluorescent molecules that might be present near the surface."

For an optical beam, the intensity of the evanescent wave (measured in units of energy per unit area per second) exponentially decays with perpendicular distance z from the interface [15]:

$$I(z) = I(0)e^{\frac{-z}{d}} \tag{2.4}$$

Where

$$d = \frac{\lambda}{4\pi\sqrt{{n_1}^2 \sin\theta^2 - {n_2}^2}} \tag{2.5}$$

with λ the wavelength of the incident light in vacuum. Depth d is independent of the polarization of the incident light and decreases with increasing θ. Except for $\theta \rightarrow \theta_c$ (where $d \rightarrow$ infinity), d is on the order of λ or smaller.

For a beam, the wave fronts of the beam can be represented as rays with arrows in the direction of propagation. Then the TIR phenomenon can be understood using ray optics. Figure 2.8 explains this schematically. Four rays are incident on the interface of the surrounding medium (n) and medium 2 (n_2) at different incident angles. All four rays get refracted at that interface according to the Snell's law, and are incident on the interface of medium 1 and medium

2. At this interface, Ray 1 and Ray 2 are incident at angles $\theta < \theta_c$, and therefore they are refracted at the interface. Ray 3 is incident at $\theta = \theta_c$, which travels parallel to the interface. Ray 4 is incident at $\theta > \theta c$, which reflects back in medium 2 due to total internal reflection.

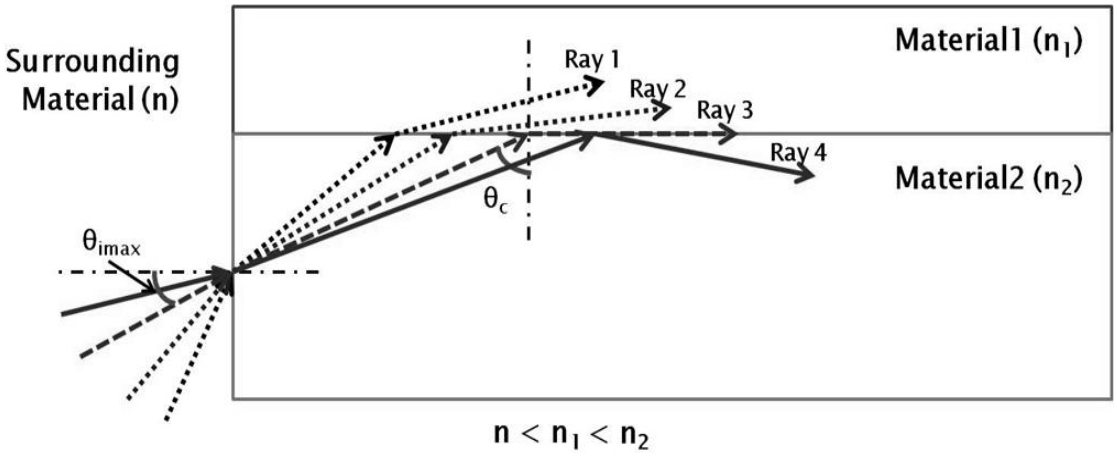

Figure 2.8, Schematic explanation of total internal reflection

"The intensity of the evanescent wave at the interface (I(0)), depends on the two indices of refraction, the incident angle of illumination θ and the polarization of the incident light. The p-polarized (parallel to the plane of incidence) and s-polarized (perpendicular to the plane of incidence) components of I(0) are given by [15]:

$$I_P(0) = |A_P|^2 \frac{(4cos^2\theta)(2sin^2\theta - n^2)}{n^4 cos^2\theta + sin^2\theta - n^2} \tag{2.6}$$

$$I_s(0) = |A_S|^2 \frac{4cos^2\theta}{1 - n^2} \tag{2.7}$$

where A_P and A_S are the corresponding p-polarized and s-polarized incident electric field amplitudes at the interface. Operation near the critical angle assures strong evanescent intensity, and a large decay length d. Proper selection of the angle θ is therefore a key feature when designing TIR optical configurations."

2.6 Optical fibers

Information in this section is reproduced from [13]: "In a PL-based sensor system, transmitting the excitation light to the luminophores and collecting emission light back from the luminophores are the primary jobs of the optics. Fibers are unequaled at this job in almost all practical applications due to their properties of long-distance transmission abilities, environmental robustness, ease of use, and low cost. An optical fiber typically consists of a higher refractive index core surrounded by a cladding material with a lower index of refraction. Light is kept in the core by total internal reflection to guide the electromagnetic waves along the fiber. Some of the fiber parameters are summarized in Table 1. Fibers that support many propagation paths or transverse modes are called a multi-mode fiber, which have a large V; while those that only support a single mode are called single-mode fibers [16]. Multimode fiber is much more suitable to the applications of PL-based sensor systems because it is significantly easier for the emission light modes to match some modes of the entire mode volume, M.

In other words, with larger NA, multimode fiber is much less sensitive to the emission light propagation direction. Moreover, between the choices of a step-index multimode fiber and a graded-index fiber, in the case of coupling non-spatial-coherent light, step-index multimode fiber is a better choice because it has a bigger M value than graded-index for a given value of V.

However, multimode fiber is inherently lossier than single mode. High-angle modes are weakly guided and so are vulnerable to scatter from irregularities in the fiber or to bending and pressure. It can be seen as a gradual decrease of the measured NA of the fiber as its length increases [17]."

Table 2.2, Fiber optics parameters

Core radius	a
Core index	n_1
Cladding index difference	n_2
Normalized index difference	$\Delta = \frac{{n_2}^2 - {n_1}^2}{2{n_1}^2}$
Numerical Aperture (NA)	$NA = \sqrt{{n_1}^2 - {n_2}^2} = n_1\sqrt{2\Delta}$
Normalized frequency (the V-number)	$V = \frac{2\pi a}{\lambda}\sqrt{{n_1}^2 - {n_2}^2} = \frac{2\pi a}{\lambda} NA$
Mode volume (M) for step index fiber	$M = \frac{4V^2}{\pi^2}$

References

[1] S. B. Pieper, *Thesis title : OPTICAL CHARACTERIZATION OF PHOTOLUMINESCENT DYES FOR BIOSENSOR TRANSDUCER APPLICATIONS,* Colorado State University, Fort Collins, Colorado, 2008.

[2] "Photonics," [Online]. Available: www.photonics.com/dictHome.aspx.

[3] "life technologies; invitrogen," [Online]. Available: http://www.invitrogen.com/site/us/en/home/support/Product-Technical-Resources/Product-Spectra.1300ph9.html.

[4] S. Santra, B. Liesenfeld, C. Bertolino, D. Dutta, Z. Cao, W. Tan, B. M. Moudgil and R. A. Mericle, "Fluorescence lifetime measurements to determine the core-shell nanostructure of FITC-doped silica nanoparticles: An optical approach to evaluate nanoparticle photostability," *Journal of Luminescence,* vol. 117, pp. 75-82, 2006.

[5] R. S. Becker, Theory and Interpretation of Fluorescence and Phosphorescence, New York: Wiley, 1969.

[6] F. P. Schafer, "Principles of Dye Laser Operation," in *Dye Lasers*, Berlin, Germany, Springer-Veriag, 1990.

[7] V. P. Chodavarapu, D. O. Shubin, R. M. Bukowski, A. H. Titus, A. N. Cartwright and F. V. Bright, "CMOS-based phase fluorometric oxygensensor system," *IEEE Transactions on Circuits and Systems I, Regular papers*, vol. 54, pp. 111-118, 2007.

[8] F. G. Gao, A. S. Jeevarajan and M. M. Anderson, "Long term continous monitoring of dissolved oxygen in cell culture medium for perfused bioreactors using optical sensors," *Biotechnology and Bioengineering*, vol. 86, pp. 425-433, 2004.

[9] "Enzyme," Merriam-Webster; an Encyclopedia Britanica Company, [Online]. Available: http://www.merriam-webster.com/concise/enzyme.

[10] "Enzyme," Wikipedia, the free encyclopedia, [Online]. Available: http://en.wikipedia.org/wiki/Enzyme.

[11] "Using Isothermal Titration Calorimetry," Genetic Engineering & Biotechnology NEWS, [Online]. Available: http://www.genengnews.com/gen-articles/using-isothermal-titration-calorimetry/1622/.

[12] O. S. Wolfeis, "Fiber-Optic Chemical Sensors and Biosensors," *Analytical Chemistry,* vol. 72, no. 12, 2000.

[13] Z. (. Yi, *Thesis title : Characterization of a Multi Characterization of a Multi-Channel Fiber Optic Photoluminescence Fiber Optic Photoluminescence-Based Sensor System*, Colorado State University, Fort Collins, Colorado, 2011.

[14] "Enzyme," Encyclopedia Britannica, [Online]. Available: http://www.britannica.com/EBchecked/topic/189245/enzyme.

[15] D. Axelrod, E. H. Hellen and R. M. Fullbright, "Topics in fluorescence spectroscopy," in *Biomedical Applications, vol.3*, New York, Plenum Press, 1992, p. 289.

[16] "Optical Fiber," Wikipedia, [Online]. Available: http://en.wikipedia.org/wiki/Optical_fiber.

[17] P. C. Hobbs, Building Electrio-optical Systems: Making It All Work, 1st Edition, New York, NY: Wiley & Sons, Inc., 2000.

Chapter 3: Review of photoluminescence based hand held sensor devices

3.1 Introduction

The goal of the study is to design a hand-held, low cost, low noise photoluminescence sensing device for enzymatic biosensor application. So, this chapter reviews five such photoluminescence sensing hand-held devices available in literature. In the five devices reviewed here, a couple consists of on-chip optical waveguides used to deliver excitation light to fluorescence source. These devices use different excitation sources and different methods to couple light into the waveguides. A couple of other devices use evanescent field of guided excitation light to excite fluorescent source. These devices employ different types of on chip optics to obtain total internal reflection of excitation light at the interface of waveguide and fluorescent source. The fifth device demonstrates a simple technique of sensing fluorescence. All these devices have their advantages and disadvantages considering the cost of engineering, design simplicity and noise. Design and functioning of all the devices are discussed in this chapter.

3.2 A handheld fluorometer

Nelson et al described the design, fabrication, and performance of a class of simple handheld fluorometers [1]. "The devices consist of a sensor along with an integrated optical filter packaged in a hand-held format. This fluorometer has been proven to be extremely portable and easy to use. It consists of four main components: 1) a sample volume to contain the fluorophore under investigation, 2) an excitation source to stimulate the fluorophore, 3) an emission filter to block the excitation wavelengths, and 4) a photosensor to detect the emitted light. Figure 1(a) shows how these components are configured in the handheld fluorometer. In addition, a data-acquisition system is used to display the sensor output. The integrated sensor (photodetector plus emission filter) is mounted onto a printed-circuit board (PCB) in a light proof case. The sensor

output is captured by a PC-based data-acquisition system (DAQ), and a custom LABVIEW program records the data and displays the sensor output. This PC-based data acquisition may be easily integrated onto the same board as the detector by replacing the laptop and DAQ card with a microcontroller and a liquid-crystal display (LCD) screen."

Initial experiments were performed with a setup as shown in Figure 1(b) where the sample is held in a standard methacrylate cuvette. Such cuvettes hold up to of 4 mL of sample. Most of the light collected by the detector originates from the portions of the volume near the detector; therefore, subsequent experiments were performed by replacing the cuvette with a well that sits directly above the chip. Such wells may be realized in a number of configurations and sizes; the one shown in Figure 1(c) holds 400 mL of sample. The hand-held fluorometer uses narrowband discrete light-emitting diodes (LEDs) as the excitation source. For the assays in this study, 375 nm (Nichia) and 525 nm (Lumex) LEDs were used.

It is well known that differential signal representations and architectures provide immunity to correlated noise. Therefore, a novel active pixel sensor (APS) was designed based on this concept [2] [3]. The sensor is a differential active pixel sensor with in-pixel correlated double sampling fabricated in a 0.5- μm 2-poly 3-metal complementary metal–oxide semiconductor process. In this study, the use of absorption filters to attenuate the excitation light is reported. These filters are fabricated by mixing chromophores into a polymer matrix which is then cast onto the chip. Thus, the rejection characteristics are determined primarily by chro-mophore concentration and film thickness, both of which can be well controlled.

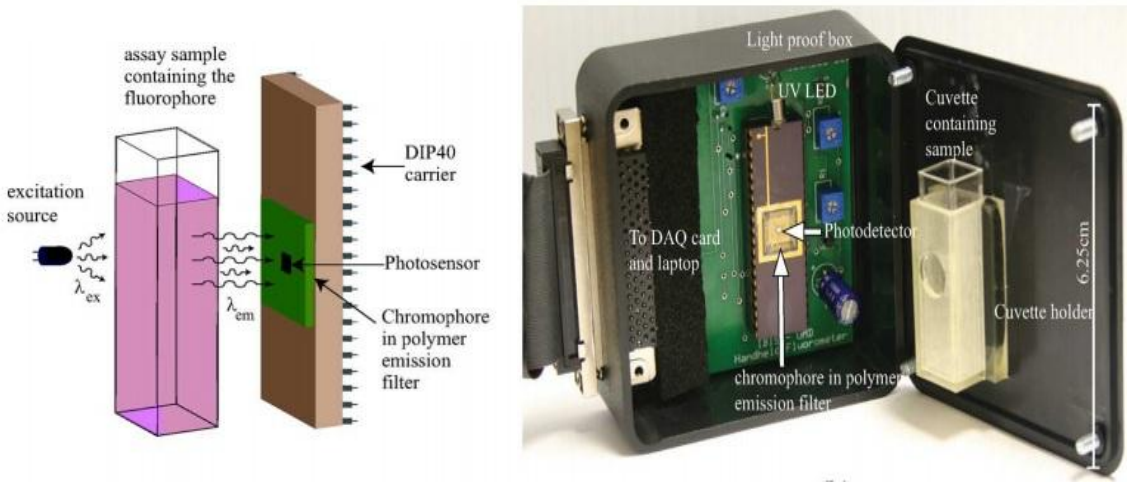

(a) (b)

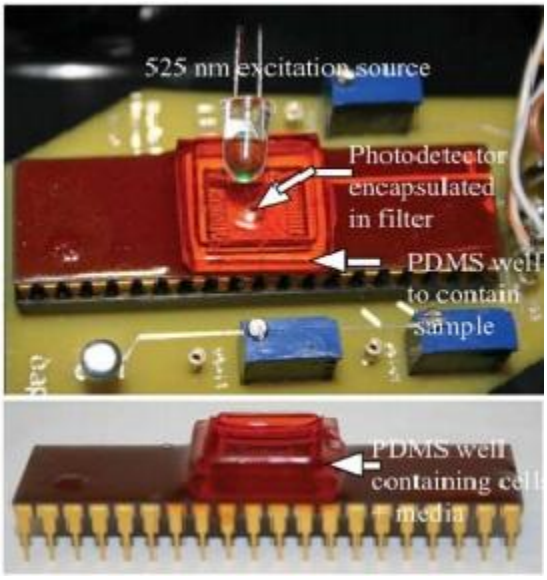

(c)

Figure 3.1, Reproduced from Nelson et al [1] (a) Handheld fluorometer components (b) Photograph of handheld fluorometer for use with a standard cuvette and 400-nm long-pass filter (c) Top and side view of the handheld fluorometer for use with the custom sample well and 540-nm long-pass filter

To achieve different filter cutoff wave-lengths, different chromophores are mixed into an optically transparent polymer. Such an integration methodology has the strong advantage of requiring only a single deposition step, with resulting performance characteristics that are relatively insensitive to fabrication tolerances. Alternative filter technologies, such as

interference filters, require much more complex fabrication and are very sensitive to fabrication tolerances [4] [5].

Two types of emission filters are utilized in the hand-held detectors reported. Both are fabricated by using chromophores obtained in powder form and dissolved into toluene, then stirred into poly-dimethyl-siloxane (PDMS) pre-cursor mixed with crosslinking agent and cast onto the surface of the packaged sensor. The filter is then cured at 70 C for 2 hours or at room temperature overnight. Varying degrees of optical rejection are obtained by varying either the amount of chromophore mixed into the polymer or the thickness of the filter film.

Figure 2(a) shows the transmission properties of 2-(2'-hydroxy 5'-methylphenyl) benzotriazole (BTA, Great Lakes Chemical, Inc.) dissolved in toluene. The filter has a long-pass characteristic with a cuton frequency at 400 nm and 60-dB rejection in toluene over a 1-cm path length. The filter is thus suitable for near UV excitation with visible light emission.

Figure 2(b) shows the transmission properties of lysochrome azo dye Sudan II. The filter has a long-pass characteristic with a cuton frequency at 540 nm and 45-dB rejection. This creates a filter that is suitable for flu-orophores that are excited by visible light in the blue and green regions and that emit light in the yellow, orange, and longer wavelength regions.

Nelson's fluorometer is demonstrated to be a very useful fluorescence sensing device for lab-on-a-chip application. The design can be used to measure the transduced fluorescent signal output from fluorescence-based enzymatic biosensor. As discussed in chapter 2, enzymatic biosensors incorporate enzymatic reaction of analyte with fluorescent source to obtain transduced fluorescent signal for sensing. Detection limit, signal to noise ratio and rejection of background excitation light for the transduced signal depend on the method employed to deliver excitation light to the fluorescent source and on how the fluorescent source is coupled with the

enzymatic reaction of analyte. Nelson's work focuses on design and demonstration of the CMOS-based differential active pixel sensor. But, it does not provide a platform to perform enzymatic reaction of analyte and couple that to the fluorescent source. Moreover, it delivers the excitation light by directly shining an LED on the fluorescent source, which illuminates the source non-uniformly and it entails in negligible rejection of excitation light from the transduced signal before filters. Therefore, the rejection of the excitation light depends totally on the filter employed, which limits the performance of the sensor employed.

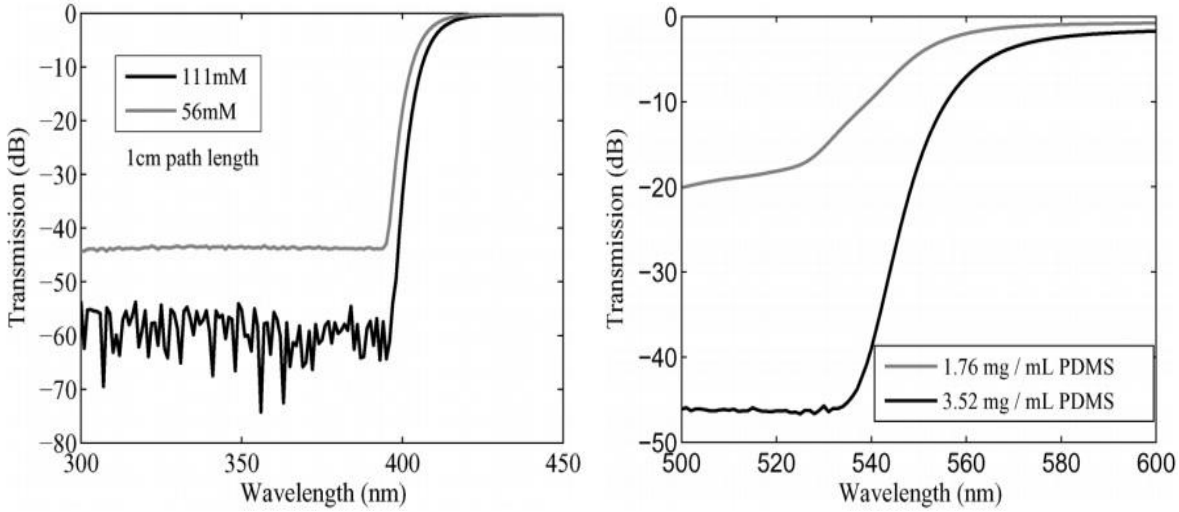

(a) (b)

Figure 3.2, Reproduced from Nelson et al [1] (a) Transmission characteristics of 2-(2'-hydroxy 5'-methylphenyl) benzotriazole in Toluene (b) Transmission characteristics of Sudan II embedded in PDMS on a glass slide

3.3 Use of optical waveguide to deliver excitation light to fluorescence source

Malins et al and Vannahme et al use an optical waveguide to deliver excitation light to the fluorescence source in their sensor designs. Malins et al demonstrated a dual-analyte optical chemical sensor platform based on the surface patterning of fluorescent dyes immobilized in sol–gel thin films as a proof of principle for a potential multi-analyte detection system with

implications for lab-on-a-chip technology [6]. A critical feature of Malins' work was the development of a suitable configuration to enable efficient and uniform excitation of the fluorescent dye-doped sol–gel layers. Sensor zones were deposited symmetrically in a radial pattern on the substrate, as shown in figure 3(a), thus enabling excitation by light injected into the sensing platform at the centre of symmetry. To this end, a conical hole of appropriate geometry was machined as shown in figure 3(b). To obtain efficient coupling into the waveguide, light has to be incident upon the substrate at an angle greater than the critical angle.

For the Perspex–air combination used here, the critical angle was of 42°. Consequently, light incident at an angle greater than this was totally reflected at the Perspex–air boundary surface, and was then guided by the sensor platform. The divergence angle of the LED (in this case 15°) was also taken into consideration and thus a 90° sink-drill was used for fabrication of the conical hole, which yielded an angle of incidence of 45° at the Perspex–air interface. This geometry was found to produce sensor platforms with efficient light-coupling characteristics, the guided LED light impacting evenly upon the dye-doped glass films and resulting in discrete fluorescent sensor zones on the platform.

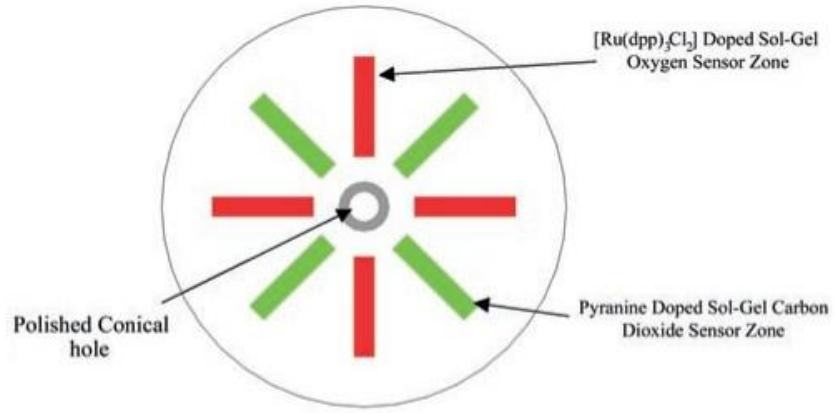

(a)

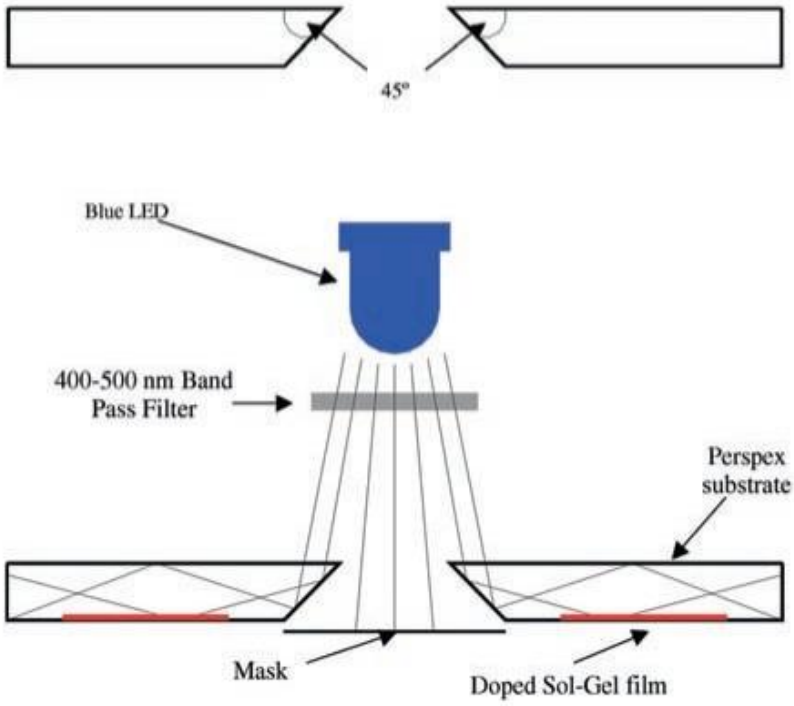

(b)

Figure 3.3, Sensor platform: (a) plan view—showing discrete sensor zones (b) side view—displaying geometry of the central conical hole and schematic representation of in-coupling of LED illumination (Reproduced from the Reference [6])

Imaging of fluorescence from the oxygen and carbon dioxide sensing areas was performed using a low-cost CCD camera and fluorescence quenching on analyte exposure was characterized. Figure 4 shows the apparatus setup used for that.

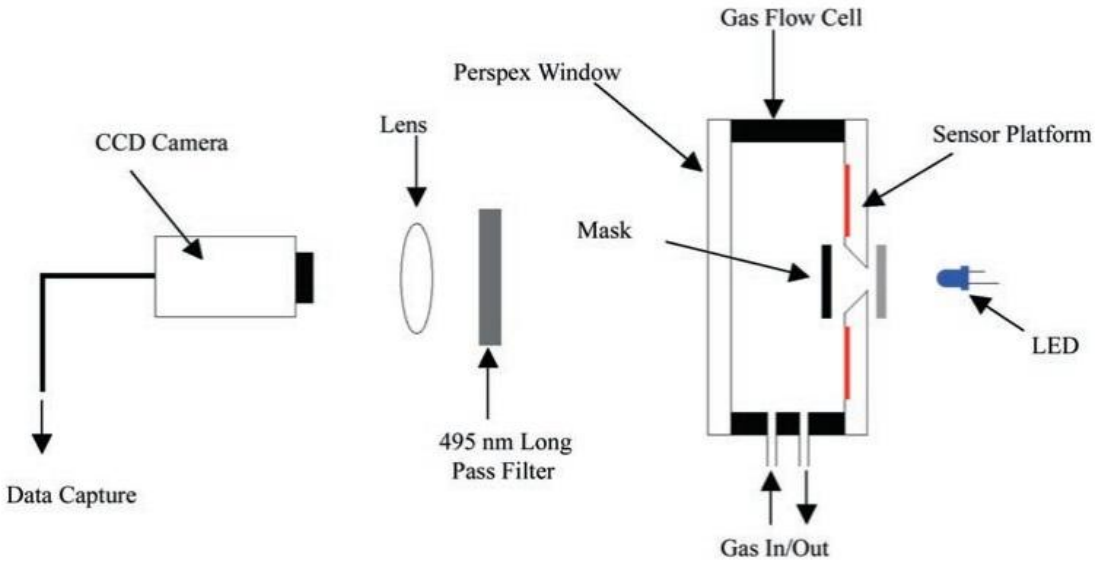

Figure 3.4, Experimental apparatus for characterization of the multi-analyte sensor platforms (Reproduced from the Reference [6])

It is evident that majority of the excitation light is guided and it travels in the direction normal to the direction in which the fluorescence is captured using CCD camera. Therefore, in this case a very good rejection of excitation light from the fluorescence signal is obtained before the 495 nm filter. This assures good performance of the sensor. Moreover, Malins et al use deposition of fluorescent dye on the substrate, which enables multiple uses of the sensor regions with different analyte concentrations. This design can be used as an enzymatic biosensor with a proper method of coupling the fluorescent dye regions with enzymatic reaction of analyte.

Similarly, Vannahme et al used deep ultraviolet induced optical waveguides to deliver the excitation light generated by the on chip distributed feedback lasers based on the organic semiconductor tris(8-hydroxyquinoline) aluminum (Alq3) doped with the laser dye 4-dicyanomethylene-2-methyl-6-(p-dimethylaminostyril)-4H-pyrane (DCM) [7]. Figure 5(a) shows

the design of the PMMA-made chip. And figure 5(b) shows the apparatus setup used to take measurements.

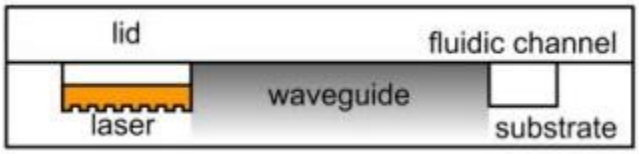

(a)

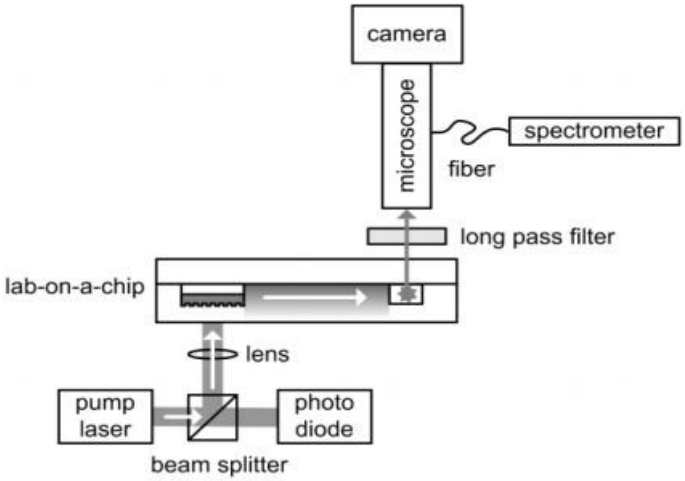

(b)

Figure 3.5, (a) sectional view of Vannahme's device (b) Schematic illustration of the optical setup to prove the functional capability of fluorescence excitation on LOC systems (Reproduced from Reference [7])

The excitation light travels in the horizontal direction and the fluorescence is collected in the vertical direction. This scheme again reduces the excitation light in significant amount from the fluorescence signal before the filter. Moreover, unlike Malins et al, Vannahme et al used PMMA material to make the waveguide and fluidics. PMMA has some advantageous properties over glass such as better shock resistance, ease of fabrication, low cost and more. Vannahme et al used these properties to their advantage.

3.4 Total internal reflection (TIR)-based lab-on-a-chip devices

Recently, total internal reflection (TIR) – based biosensors have attracted increasing attention due to the great reduction of background noise and suitability for studying biochemical kinetics on substrate surfaces. TIR-based biosensors are made using micro-fabrication techniques with polymer/elastomer based fluidics and semiconductor/polymer based optics in general. These devices utilize the evanescent field of the guided excitation light to excite the fluorescence source. This scheme reduces the background excitation light level in the fluorescence signal to null theoretically, however very small amount of excitation light remains present in the signal before any kind of filtering due to scattering of the excitation light at the interface.

Chronis et al designed, fabricated and demonstrated a (TIR)-based biochip utilizing a polymer-filled cavity with a micromirror sidewall [8]. The micromirror sidewall cavity facilitated precise alignment of the excitation light beam into the system. Figure 6 shows a schematic cross section of the chip and the path of the light beam as it passes through. The geometry of the micromirror makes it possible to vertically integrate a light source directly below the micromirror with no need of any external optics. More importantly, this design eliminates the need to align the light beam into the system at the desired angle. The angle of the tilted micromirror is accurately defined by the microfabrication process (54.7° for standard KOH etch of a {100} silicon wafer) and it can be changed by properly selecting polymers of different index of refraction (see section E). Dynamically changing the incident angle12 is not an advantageous feature for lab-on-a-chip applications, since it requires the use of a complex optical and mechanical configuration and the interaction of the end-user with the system.

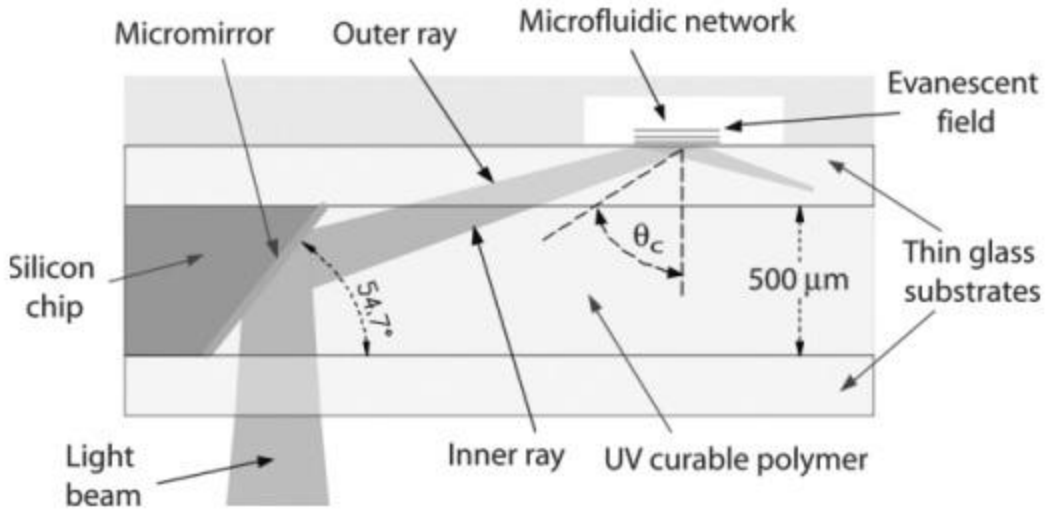

Figure 3.6, Schematic cross-section of the four-layer chip. The laser beam enters at the bottom of the chip and is redirected upon hitting the micromirror sidewall of the polymer-filled cavity (Reproduced from Reference [8])

The chip consists of four substrates stacked together. A silicon substrate that contains the micromirror, sits between two thin (~ 200 mm) glass (AF-45, index of refraction n1 = 1.526) wafers. The cavity that is formed between the two glass wafers and the micromirror surfaces is filled with a transparent UV curable polymer (Norland Optical Adhesive 65, index of refraction n_2 =1.524) that couples the exciting light into the system. The UV curable polymer is an essential component for efficient optical coupling, minimizing the reflectance losses to less than 5% (see section E). The top glass wafer serves as the functional substrate where TIR takes place, while the bottom one is used to planarize the UV curable polymer. The light beam is weakly focused on the interface where it is totally internally reflected, creating the evanescent field.

The device is made using standard bulk micro-machining techniques using photolithography and etching and thin film deposition. These techniques require high technology equipments. Moreover, the use of glass material and the mirror deposition is relatively costly for disposable biochip applications. Also, the brittleness of silicon and glass materials makes the chip fragile without a proper packaging using shock resistant material.

Huang et al fabricated and demonstrated a TIR-based biosensor with integrated microfluidic chamber, polymer- based optics and planar waveguides into a high-throughput platform [9]. The polymer-based optics, fabricated by SU-8 resist, includes cylindrical microlenses and a microprism array for effectively conducting the excitation light into the planar waveguide. It consists of two layers of structures (figure7); one layer includes the cylindrical microlens and the microprism array fabricated by SU-8 resist for effectively conducting the excitation light into the second layer of an integrated optical waveguide composed of SU-8 resist. TIR will occur at the interface between the waveguide and the aqueous solution to induce the evanescent wave for fluorescence excitation. To fabricate the microprism array, the glycerol-compensated oblique-exposure technique which can be used to fabricate inclined structures from 19° to 90° with 2° accuracy is employed [10, 11].

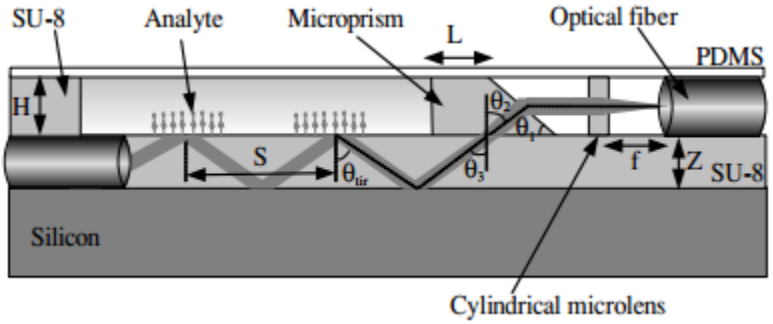

Figure 3.7, cross sectional view of the monolithic TIR-based biosensor (Reproduced from Reference [9])

Huang's novel design promises high coupling efficiency and minimizes reflectance loss on interfaces between waveguides and microprisms. But, use of SU-8 for making planar waveguides makes it difficult to deposit fluorescent indicator and/or enzyme on its surface due to highly hydrophobic nature of SU-8. Moreover, monolithic design requires very sophisticated apparatus setup and high technology costly equipments and masksets for fabrication.

Thus, the highest rejection of excitation light from signal and very efficient excitation of fluorescent source can be achieved using TIR-based devices. However, a strong need exists to fabricate TIR-based devices from low cost, easy to use materials using very simple fabrication techniques with simpler equipments and apparatus setup to create groundbreaking opportunities for highly portable, efficient and cost effective biosensing.

References

[1] N. Nelson, D. Sander, M. Dandin, S. B. Prakash, A. Sarje and P. Abshire, "Handheld Fluorometers for Lab-on-a-Chip Applications," *IEEE TRANSACTIONS ON BIOMEDICAL CIRCUITS AND SYSTEMS,* vol. 3, no. 2, pp. 97-107, April 2009.

[2] D. Sander, M. Dandin, H. Ji, N. Nelson and P. A. Abshire, "Low-noise CMOS fluorescence sensor," in *Proceedings of IEEE International Symposium of Circuits and Systems*, New Orleans, LA, May 2007.

[3] D. Sander, N. Nelson and P. Abshire, "Noise model, analysis and characyerization of a differential active pixel sensor," in *Proceedings of IEEE International Symposium of Circuits and Systems*, Seattle, WA, May 2008.

[4] M. A. Burns, B. N. Johnson, S. N. Brahmasandra, K. Handique, J. R. Webster, M. Krishnan, T. S. Sammarco, P. M. Man, D. Jones, D. Heldsinger, C. H. Mastrangelo and D. T. Burke, "An integrated nano-liter DNA analysis device," *Science,* vol. 282, pp. 484-487, 1998.

[5] M. Dandin, P. Abshire and E. Smela, "Optical filtering technologies for integrated fluorescence sensors," *Lan on a Chip,* vol. 7, pp. 955-977, 2007.

[6] C. Malins, M. Niggemann and B. D. MacCraith, "Multi-analyte optical chemical sensor employing a plastic substrate," *Measurement Science and Technology,* vol. 11, pp. 1105-1110, 2000.

[7] C. Vannahme, S. Klinkhammer, U. Lemmer and T. Meppes, "Plastic lab-on-a-chip for fluorescence excitation with integrated organic semiconductor lasers," *OPTICAL EXPRESS,* vol. 19, no. 9, April 2011.

[8] N. Chronis and L. P. Lee, "Total internal reflection-based biochip utilizing a polymer-filled cavity with a micromirror sidewall," *Lab on a Chip,* vol. 4, pp. 125-130, 2004.

[9] S.-H. Huang and F.-G. Tseng, "Development of a monolithic total internal reflection-based biochip utilizing a microprism array for fluorescence sensing," *JOURNAL OFMICROMECHANICS AND MICROENGINEERING,* vol. 15, pp. 2235-2242, 2005.

[10] K. Y. Huanh, H. T. Hu and F. G. Tseng, "Application of 3D glycerol-compensated inclined-exposure technology to an integrated optical pick-up head," *JOURNAL OFMICROMECHANICS ANDMICROENGINEERING,* vol. 14, pp. 975-983, 2004.

[11] K. Y. Huang, H. T. Hu and F. G. Tseng, "A novel fabrication technology for smooth 3D inclined polymer microstructures with adjustable angles," in *12th International Conference on Solid state Sensors, Actuators and Microsystems*, 2003.

Chapter 4: Total internal reflection-based biosensor device concept and material selection

4.1 Introduction

While implementing the total internal reflection (TIR)-based enzymatic biosensor device, the idea is to excite photoluminescent source (dye) using evanescent field of guided excitation light. TIR-based implementation includes integration of optical waveguide and fluidic channel on a single device. It effectuates good when the materials used for it possess appropriate optical and chemical properties. Chemical properties of materials are important to consider determining the limitations of the end point biosensor device. For that, appropriate optical and chemical properties of the materials were decided upon. Then, a quest for materials possessing such properties was held. The entire pursuit of properties and materials is presented in this chapter.

In section 4.1, the essentials of TIR concept and its biosensor implementation are explained. Based on that, a set of sought-after material properties were decided upon. In section 4.2, the most important optical properties like optical transmittance and refractive index are explained. Basic sought-after optical and chemical properties of some glass materials are discussed in section 4.3. In section 4.4, chemical resistance, chemical permeability, autofluorescence and refractive index properties of several thermoplastic materials are discussed. In section 4.5, the selection of materials with appropriate properties and cost is argued.

4.2 TIR-based biosensor device concept and desired properties of materials

The operating principle of photoluminescence based sensors, fluorescence based or phosphorescence based, is to excite photoluminescent dye molecules using excitation light at a particular wavelength and use the resultant photoluminescence of the dye, emitted at some different wavelength, as a signal for sensing. The sensing mechanism of photoluminescence-based enzymatic biosensors is contingent upon quenching of photoluminescence of dye molecules. It uses enzymes as bio-components that catalyze quenchers of photoluminescence in

concentrations proportional to the analyte concentrations. This quenched photoluminescence signal is used as a transduced signal for sensing. The total internal reflection-basedmechanism uses the evanescent field tail of guided excitation light to excite photoluminescent dye sitting on the surface of a planar waveguide core.

Figure 4.1 shows schematic cross section of TIR-based enzymatic biosensor device. A planar optical waveguide consists of two optical materials with different refractive indices. A planar slab of the material with higher value of refractive index (n_2) is core of the waveguide, which is buffered between two planar slabs of the other material; the cladding; with relatively lower value of refractive index (n_1). Optical waves are guided into the waveguide core due to the total internal reflection of optical waves at the core-cladding interface, when the waves are launched at proper launching angle. Macroscopically, the waves are internally reflected at the core-cladding interface, but microscopically, an evanescent tail of field penetrates the cladding material. The penetration depth of the evanescent field tail depends on the wavelength and the incidence angle of the guided waves. It is given by the following equation [1],

$$d = \frac{\lambda}{4\pi\sqrt{{n_1}^2 \sin\alpha^2 - {n_2}^2}} \tag{4.1}$$

Where, d = penetration depth, n_1 = refractive index of core material, n_2 = refractive index of the cladding material, λ = wavelength of optical wave, α = incidence angle. At incidence angle (α) equal to the critical angle (α_c), $\sin\alpha_c = \frac{n_2}{n_1}$, and hence, the penetration depth is theoretically infinite. With appropriate value of penetration depth at excitation wavelength, the photoluminescent dye can be excited.

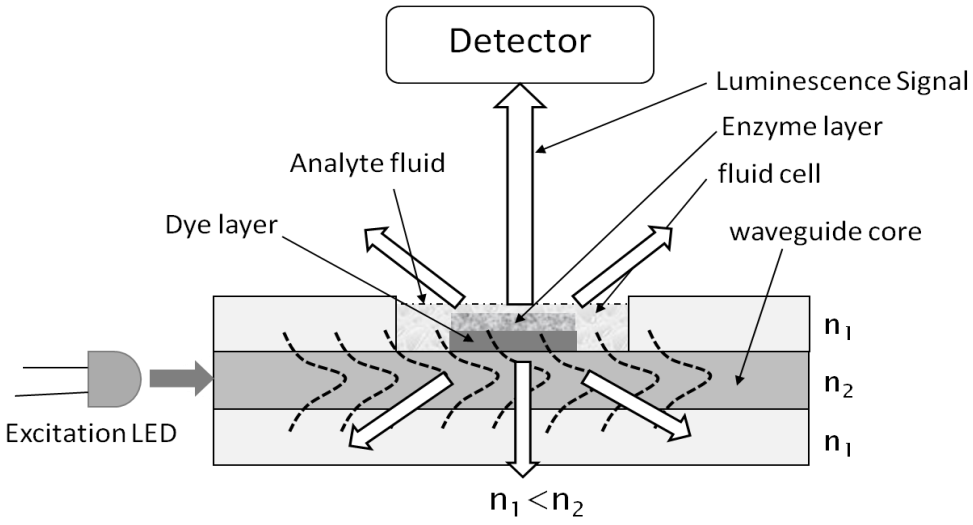

Figure 4.1, schematic cross section of TIR-based enzymatic biosensor conceptual device

It is essential to incorporate a fluid cell into the device design to implement a biocomponent-transducer reaction chamber for bio-sensing. The fluid cell is fabricated in the upper-cladding slab. The photoluminescent dye is deposited on the surface of the waveguide core in the fluid cell. A layer of bio-component; i.e., enzyme; is deposited on the dye layer. Both the layers are surrounded by the analyte fluid in the cell. The enzyme layer catalyzes quencher molecules in the concentration proportional to the concentration of the analyte molecules. When the excitation light is coupled into the waveguide, the evanescent field of the guided light penetrates into the cladding. The guided field is shown in the figure by the blue bell-shaped curves all across the core and the evanescent field is shown as rapidly dying exponential tails of the curves. This evanescent field tails are used to excite the dye layer. The excited dye layer emits photoluminescence at a wavelength different and larger than that of the excitation light. The quencher molecules catalyzed by the enzyme diffuse through the enzyme layer and reach the dye layer quenching its photoluminescence. The quenched photoluminescence can be detected by the detector as a transduced signal, and when then detector is calibrated properly the signal

can be used for sensing different levels of concentrations of analyte molecules. Thus, in the entire scheme, the dye layer acts as a transducer and the enzyme layer as a bio-component for sensing. Thus, the schematic represents how the total internal reflection concept can be implemented for bio-sensing applications. But, which materials should be used and what kind of mechanism for launching the excitation light and collecting fluorescence should be used, are to be explored.

It is wise to enlist the requirements of the properties of the materials to be used. It is tacit from the discussion that two optical materials with different refractive indices are required to implement optical waveguide. Moreover, the lower refractive index material in the two; the cladding material; should possess properties to facilitate channel fabrication. For that, the cladding material should be easily processed or molded. In addition, both, the core and the cladding materials should be optically clear, polish-able and capable of being bound to each other. Also, these materials should be low cost as to be used for disposable biochip design. These required properties for both the materials are summarized and enlisted in table 4.1. In addition to these, some properties like chemical resistance, chemical permeability and chemical diffusion are important to know to decide upon the limitations of the end point bio-chip design.

Commercially available thermoplastics like poly(methyl methacrylate), poly carbonate, Cyclic olefin copolymer, polyethylene terepthalate glycol and optical glasses from Schott like BK7, F2, SF11, LaSFN9, BaK1, all of these materials are optically clear and are available with optically smooth surfaces. Also, two materials with different refractive index values can be selected from these materials as their refractive index values are different from one another. Optical clarity and smoothness are required but not sufficient properties for TIRF implementation. All of the thermoplastic materials possess background fluorescence called auto-

fluorescence, which is a limiting property. Moreover, these plastic as well as the glass materials possess some chemical properties like chemical resistance and chemical permeability, which are sometimes useful and sometimes limiting. So, it is important to know about these properties quantitatively and qualitatively before two appropriate materials are chosen from the aforementioned materials.

Table 4.1, list of required material properties for

Material 1 **Refractive index n1**	**Material 2** **Refractive index n2**
Optically clear	Optically clear
Optically smooth surfaces and edges →polish-able	Optically smooth surfaces and edges →polish-able
Easy processing/molding/fabrication	
Low cost	Low cost
n1 less than n2	n1 less than n2

4.2 Optical and chemical properties of glass materials

Glass manufacturers provide hundreds of different glass types with differing optical and chemical properties. A wide variety of glass materials are available with their refractive indexes in the range from 1.42 to 1.82. Along with the refractive index and transmittance of glass materials, some chemical properties like stain resistance, acid resistance and alkali resistance are also important to consider, because these properties can affect how easy it is to fabricate the material into shape.

4.2.1 Optical properties

Refractive index

Two different materials with different refractive indexes are required to effectuate optical waveguide. For that, it is necessary to have refractive index values of glass material. The change

in refractive index with wavelength (dispersion) is not big of a concern for TIR-based device concept under study, as it employs monochromatic waveguide.

Optical transmission

The material used for waveguide core should transmit very well at the wavelength of interest. Transmission versus wavelength graph for a given material helps to find out the transmittance of the material at the wavelength of interest.

Optical properties like dispersion (abbe number) and birefringence are important to consider for multichromatic optical applications and applications where optical polarization is critical. But, these properties are not that critical for TIR-based device application under study as it includes a monochromatic waveguide.

4.2.2 Chemical properties

Optical glasses acquire their properties through their chemical composition, melting process and finishing methods. In order to obtain specific optical properties, chemical compositions must often be chosen that lead to products with less than optimum chemical resistance. For this reason there is a relatively large range of resistance of the different optical glasses with reference to environmental influences and chemical demands. Chemical properties of optical glass materials along with their dependence on material composition are explained in TIE-30, technical information document from advanced optics (schott glasses) [2]. Some of the information from the TIE-30 document is briefly presented here.

"In large quantities of neutral or acidic media, chemical processes occur in which cations from the glass (preferably alkali ions) are exchanged with the hydrogen ions from the solution. Leached layers that are also called "silicate gel layers" because of their composition are formed over the course of time, their thickness depending on the resistance of the glass. Acid resistance test SR internationally standardized according to ISO 8424: 1996 [3]. On the other hand,

hydroxide ions from alkaline solutions destroy bonds between the silicon and oxygen ions that give the glass its structure. The glass is dissolved. These processes can play a role in polishing and washing operations. Alkali resistance test AR and phosphate resistance test PR are also internationally standardized according to according to ISO 10629: 1996 [4] and ISO 9689: 1990 [5] respectively. A change in humidity and temperature on glass surfaces can lead to localized corrosion, which is characterized by the test for climatic resistance (ISO/DIS 13384) [6]."

Climatic resistance (ISO/DIS 13384)[2]

"Climatic resistance describes the behavior of optical glasses at high relative humidity and elevated temperatures. The influence of water vapor in the air, especially under higher humidity and temperatures, can cause a change in the glass surface in the form of a cloudy film that generally cannot be wiped off. The chemical process is a reaction with water in deficiency. Under normal atmospheric conditions such changes take place slowly even in sensitive glasses.

An accelerated procedure is used to test the climatic resistance of glasses. Polished, uncoated glass plates are exposed to a water vapor saturated atmosphere, the temperature of which is alternated between 40°C and 50°C on an hourly basis. Since the temperature increase in the glass plates follows that of the atmosphere, water condenses on the glasses during the warming phase. In the cooling phase the temperature of the atmosphere initially falls faster than that of the glass plates causing a drying of the glass surface. This is augmented by a heating source.

After an exposure time of 30 hours the glass plates are removed from the climatic chamber. The degree of weathering of the glass surface is determined by measuring the difference in haze between the weathered and the virgin specimen. The measurements are

conducted using a sphere transmission haze meter. The classification is done based on the haze difference value ΔH obtained after the 30 hour test period. Table 4.2 lists the climatic resistance classes."

Table 4.2, Classification of optical glasses into climatic resistance classes CR 1 – 4 based on transmission haze increase after being subjected to a 30 hour climatic change test in the temperature range from 40°C to 50°C. Reproduced from [2].

Climatic resistance class CR	**1**	**2**	**3**	**4**
Haze difference ΔH	< 0.3%	≥ 0.3% < 1.0%	≥ 1.0% < 2.0%	≥ 2.0%

Acid Resistance (ISO 8424:1996)[2]

"Acid resistance classifies the behavior of optical glasses that come in contact with larger quantities of acidic solutions (for example, laminating substances, carbonated water, etc.). If an acidic aqueous medium reacts with a glass surface, stains can form (see stain resistance), or the glass can decompose, or both reactions can occur simultaneously. The acid resistance test provides particularly valuable information concerning dissolution of the glass. For the test, glass specimen polished on all six surfaces, are immersed in a large quantity of acidic solution. The time t required to dissolve a layer with a thickness of 0.1 μm at 25°C serves as a measure of the resistance to acids. The layer thickness is calculated from the weight loss per surface area and the density of the glass.

Two aggressive solutions are used in determining the resistance of the glasses to acids. A strong acid (nitric acid, c = 0.5 mol/l, pH 0.3) is used for the more resistant glass types, whereas glasses with less acid resistance are exposed to a weak acidic solution with a pH value of 4.6 (sodium acetate buffer).

This method, using two different solutions, is adopted to allow for the fact that some glasses cannot contain enough of the sparingly soluble substances to be able to achieve greater chemical resistance without negatively influencing the optical specification. Such glasses are therefore susceptible to damage during processing, since even weak acids with pH values of 4 - 6 (for example, carbonic acid, cements, perspiration, etc.) can cause noticeable deterioration.

Class SR 5 represents the transition point between the more acid resistant glasses SR 1 – 4 and the more acid sensitive glasses in SR 51 – 53. Class SR 5 includes glasses for which the time for removal of a layer thickness of 0.1 μm at a pH value of 0.3 is less than 0.1 h and at a pH value of 4.6 is greater than 10 hours. An overview of the classes is listed in Table 4.3."

Alkali resistance (ISO 10629: 1996)[2]

"The alkali resistance indicates the sensitivity of optical glasses in contact with warm, alkali liquids, such as cooling liquids in grinding and polishing processes. The test takes into account the fact, that through processing which occurs mostly in water based media the solution usually becomes increasingly alkaline through the chemical reactions of water with the abraded glass particles. This particularly applies when such solutions are recycled. Also taken into consideration is the fact that higher temperatures can occur as a result of the abrasion. Finally, consideration has also been paid to the fact that warm alkaline solutions are widely used in washing processes for the cleaning of polished surfaces."

Table 4.3, Classification of optical glasses in acid resistance classes SR 1 – 53 based on the time in which a layer thickness of 0.1 μm is removed in an acidic or weak acidic solution of a given pH value at a temperature of 25°C. Reproduced from [2]

Acid resistance Class SR	1	2	3	4	5		51	52	53
pH	0.3	0.3	0.3	0.3	0.3	4.6	4.6	4.6	4.6
Time [h]	> 100	10 – 100	1-10	0.1-1	<0.1	>10	1-10	0.1 - 1	< 0.1

"The alkali resistance class AR is based on the time required to remove a layer thickness of glass of 0.1 μm in an alkaline solution (sodium hydroxide, c = 0.01 mol/l, pH = 12) at a temperature of 50°C. The layer thickness is calculated from the weight loss per surface area and the density of the glass. Table 4.4 lists the alkali resistance classes."

Table 4.4, Classification of the optical glasses in alkali resistance classes AR 1 – 4 based on the time required to remove a layer thickness of 0.1 μm at a temperature of 50 °C in a caustic sodium solution with a pH value of 12. Reproduced from [2]

Alkali resistance classes AR	1	2	3	4
Time [h]	> 4	1 – 4	0.25 – 1	< 0.25

Phosphate Resistance (ISO 9689: 1990)[2]

"The phosphate resistance describes the behavior of optical glasses during cleaning with washing solutions. The method takes into account the fact that the washing solutions (detergents) used for cleaning usually are not pure hydroxide solutions, rather they contain polyphosphates among other things. The phosphate resistance classes allow statements to be made regarding the resistance of optical glasses to such detergents.

The phosphate resistance class PR is based on the time required to remove a layer thickness of glass of 0.1 μm in an alkaline phosphate containing solution (pentasodiumtriphosphate $Na_5P_3O_{10}$, c = 0.01 mol/l, pH = 10) at a temperature of 50°C. The layer thickness is calculated from the weight loss per surface area and the density of the glass. Table 4.5 lists the phosphate resistance classes.

Schott enterprise provides a variety of glass materials comprehending all the classes of acid, alkali, climate and phosphate resistance. The materials which belong to the classes representing more than moderate resistance are not suitable for the application under study, as

high resistance to acid, alkali and phosphate limits how easily the material is fabricated to shape [7]."

Table 4.5, Classification of the optical glasses in phosphate resistance classes PR 1 – 4 based on the time required to remove a layer thickness of 0.1 μm at a temperature of 50 °C in a pentasodiumtriphosphate solution with a pH value of 10 (PR). Reproduced from [2].

Phosphate resistance classes PR	1	2	3	4
Time [h]	> 4	1 – 4	0.25 – 1	< 0.25

"It also limits the ability to fabricate or mold fluidic channels in the glass substrate. So, optical glass materials from schott with moderate chemical resistance like BK7, F2, SF11, LaSFN9, BaK1 were explored. These materials are presented here with their transmittance, refractive index and chemical resistance values. These materials possess very high optical transmittance of 99% over the spectral range of 400nm to 1500nm. This data is available in the datasheets of these materials. Table 4.6 gives refractive index values for five wavelengths over visible spectrum. Chemical resistance class values for all the materials are given in Table 4.7. "

Table 4.6, refractive index values for optical glasses from Schott (Reproduced from material datasheets)

Materials	**Optical wavelengths**				
	365.0 nm	**486.1 nm**	**587.6 nm**	**656.3 nm**	**852.1 nm**
BK7	1.5363	1.5224	1.5168	1.5143	1.5098
F2	1.6662	1.6321	1.6200	1.6150	1.6067
SF11	1.8570	1.8065	1.7847	1.7760	1.7618
LaSFN9	1.9021	1.8690	1.8503	1.8426	1.8300
BaK1	1.5972	1.5794	1.5725	1.5695	1.5642

4.3 Optical and chemical properties of plastics

The most desirable materials for TIRF concept should be low cost, light weight, easy to fabricate, mass producible and they should also meet the refractive index, optical transmittance and chemical resistance requirements. Plastic is another category of materials that can meet

these requirements. Plastics are further subcategorized as thermosoftening plastics (thermoplastics) and thermoset plastics. Thermoset plastics are very highly resistant to thermal energy and chemicals and they cannot be molded after curing. On the other hand, thermoplastics become pliable and moldable above a specific temperature, and returns to a solid state upon cooling. Therefore, for TIRF application thermoplastics are better materials than thermoset plastics. Thermoplastics are further subcategorized in many ways based on their monomer molecules; poly(methyl methacrylate)-PMMA, poly(carbonate)-PC, poly(styrene), poly(ester), Poly(styrene)-PS, poly(siloxanes), fluorine containing polymers and cyclic olefin polymers and copolymers are several examples of thermoplastic categories. Some basic optical and chemical properties of thermoplastics should be explored to compare different thermoplastics on their basis in search for the best suitable material.

Table 4.7, chemical resistance classes for optical glasses from Schott (Reproduced from material datasheets)

Materials	**Climatic Resistance**	**Acid Resistance**	**Alkali Resistance**	**Phosphate Resistance**
BK7	2	1.0	2.0	2.3
F2	1	1.0	2.3	1.3
SF11	1	1.0	1.2	1.0
LaSFN9	2	2.0	1.0	1.0
BaK1	2	3.3	1.2	2.0

4.3.1 Basic optical properties of thermoplastics

As discussed earlier, refractive index and optical transmittance are primary optical properties of interest. Values of these properties for some commonly used thermoplastics for optical applications like styrene acrylonitrile (SAN), PMMA, PC, PS, cyclic olefin copolymer (COC) from topas and cyclic olefin polymer (COP)-Zeonex are given in Table 4.8, along with

very widely used elastomer; poly (dimethylsiloxane) – PDMS. This plastics/elastomer provides about 92% transmittance over a range of refractive index values. Although their optical transmittance is a little less than that of optical glasses, these materials have been used in various optical applications replacing optical glasses due to their properties like low cost, ease of fabrication, shock resistance and light weight.

Table 4.8, refractive index and optical transmittance (T) values for thermoplastics

	Refractive index Vs wavelength					**T**
	435.8 nm	**486.1 nm**	**587.6 nm**	**656.3 nm**	**780 nm**	**t = 2mm**
PMMA [8]	1.5025	1.4973	1.4914	1.4880	1.4846	92%
COC [10]	1.5451	1.5399	1.5332	1.5304	1.5270	91.2%
PC [8]	1.6117	1.5994	1.5849	1.5782	1.5712	88%
SAN [8]	1.588	1.578	1.567	1.5616	1.5556	-
PS [8]	1.6171	1.6056	1.5917	1.5853	1.5785	90%
COP [11]	1.5369	1.5317	1.5251	1.5224	-	-
PETG [12]	≈ 1.57 to 1.54 (over visible spectrum)					-
PDMS [9]	≈ 1.46 to 1.43 (over visible spectrum)					-

4.3.2 Chemical resistance of thermoplastics

Chemical resistance of thermoplastic materials to organic and inorganic chemicals is classified in three classes. In Table 4.9, chemical resistance classes of some thermoplastics (at room temperature) along with that of PDMS to some chosen organic and inorganic chemicals are given. The materials are resistant, limited resistant or not resistant to the solvents. If some material is resistant to some chemicals then the chemicals do not have any detrimental effect on the material, and if the material is partially resistant then the chemicals stain the material surface and exhibit detrimental effects like swelling and/or cracking. If the material is not resistant then the chemicals are the perfect solvents of it with different solubility values. Unlike glass materials, chemical resistance levels of thermoplastics don't control how easily they are

fabricated into shape. Thermoplastic materials possess inherent property to be easily molded at high enough temperature and to be cured on cooling down to room temperature. But, these chemical resistance properties of thermoplastics are important to know to determine the limitations of end point bio-sensor.

Table 4.9, chemical resistance information of thermoplastics
(√ - resistant, o – limited resistant, X – poor resistant)

	PMMA	**PC**	**SAN**	**PS**	**COC**	**COP**	**PETG**	**PDMS**
	[13, 15]	**[13, 16]**	**[17]**	**[13, 17]**	**[13]**	**[11]**	**[14]**	**[18]**
Acids (50%)	√	√	O	√	√	√	√	√
Alkalis	√	X	√	√	√	√	√	√
Alcohols	√	O	√	O	√	√	√	√
Ketones	X	X	X	X	√	O	X	√
Esters	X	X	X	X	√	X	X	√
Chlorinated	X	X	O	X	X	X	X	O
Aromatic	X	X	X	X	X	X	X	X
Gasoline	O	O	O	X	X	X	O	√
Oils	√	O	O	X	X	X	O	√

4.3.3 Poly(dimethyl siloxane) – PDMS

PDMS is very widely used silicone based elastomer. It has been used in fluidics (valves, pumps, fluidic circuits), optical systems (adaptive lenses, tilting mirrors), and sensors (acceleration sensors, tactile sensors, chemical sensors, medical sensors) [19-21]. Fluidic channels of any size and shape can be fabricated in PDMS, as it is easy to do that using appropriate mold [22]. PDMS material possesses some physical and chemical properties that make it very appropriate material for designing devices with different functionalities. McDonald et al. have tabulated the physical and chemical properties of PDMS with their consequences [19]. That information is reproduced here in table 4.10.

Table 4.10, physical and chemical properties of PDMS. Reproduced from Reference [19].

Properties	**Characteristic**	**Consequence**
Optical	transparent; UV cutoff, 240 nm	optical detection from 240 to 1100 nm
Electrical	insulating; breakdown voltage, $2x10^7$ V/m	allows embedded circuits; intentional breakdown to open connections
Mechanical	elastomeric; tunable Young's modulus, typical value of ≈750 kPa	conforms to surfaces; allows actuation by reversible deformation; facilitates release from molds
Thermal	insulating; thermal conductivity, 0.2 W/(m.K); coefficient of thermal expansion, 310 μm/(m.°C)	can be used to insulate heated solutions; does not allow dissipation of resistive heating from electrophoretic separation
Interfacial	low surface free energy ≈ 20 erg/ cm^2	replicas release easily from molds; can be reversibly sealed to materials
permeability	impermeable to liquid water; permeable to gases and nonpolar organic solvents	contains aqueous solutions in channels; allows gas transport through the bulk material; incompatible with many organic solvents
Reactivity	inert; can be oxidized by exposure to a plasma; $Bu_4N^+F^-$((TBA)F)	unreactive toward most reagents; surface can be etched; can be modified to be hydrophilic and also reactive toward silanes; etching with (TBA)F can alter topography of surfaces
toxicity	Nontoxic	can be implanted in vivo; supports mammalian cell growth

4.3.4 Auto-fluorescence of plastic materials

There is one more limiting property of thermoplastic substrates; background fluorescence or auto-fluorescence. Auto-fluorescence can interfere with on-chip optical measurements for TIRF chips and such interference often leads to suboptimal limit of detection [23]. It is important

to know the spectral contribution of auto-fluorescence in limiting device performance while considering fluorescence based optical sensing applications. Only a few reports have been reported on auto-fluorescence of plastic materials. Piruska et al. [23] studied the auto-fluorescence magnitude and dynamics of Borofloat glass, several plastic materials and the associated plastic chips at four different laser excitation wavelengths; 403nm, 488nm, 532nm and 633nm [24]. They found the autofluorescence magnitude of the Borofloat glass material from Schott to be the least, while the auto-fluorescence of the plastic materials was found higher than the Borofloat. The highest fluorescence was found at 403nm the shortest wavelength studied. For longer wavelengths the auto-fluorescence magnitude was found to reduce. PDMS and PMMA exhibited the lowest auto-fluorescence magnitudes. In all cases chips yielded significantly higher auto-fluorescence. However, Piruska et al. did not study the fluorescence spectra of the materials.

The fluorescence spectra of plastic materials like PMMA, COC, PDMS, PC, and PETG were studied for excitation wavelength of 470nm. A fiber coupled blue LED with center wavelength at 470nm (Industrial fiber optics, IF92B) was used as the excitation source. The auto-fluorescence spectra of these materials were collected using a fiber in lateral direction and measured using a fluorescence spectrometer (Ocean optics; USB4000 FL). A schematic of experimental setup is given in figure 4.3. Plastic optical fibers (SH4001-1.3, 980μm core diameter, Industrial Fiber Optics) were used for excitation and collection fibers.

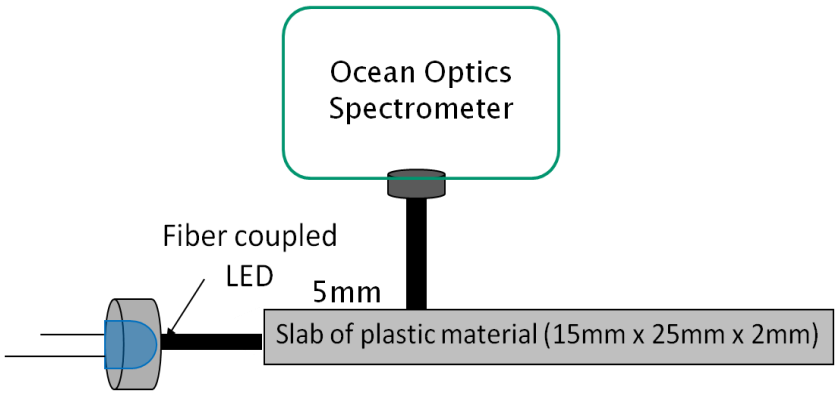

Figure 4.3, experiment setup for plastic auto-fluorescence measurement

The resultant spectra are shown in figure 4.4. In figure 4.4(a), spectra of COC, PMMA and PDMS are given, which were taken at spectrometer integration time of 100ms. In figure 4.4(b), spectra of PETG and PC are given, which had the spectrometer integration time to be 1s. The reason behind taking different integration time was to keep the intensity readings at comparable levels for the transmittance values of PETG and PC being very small compared to that of other materials. In all the spectra, the 470 nm peak is excitation wavelength and the long falling tail is due to fluorescence.

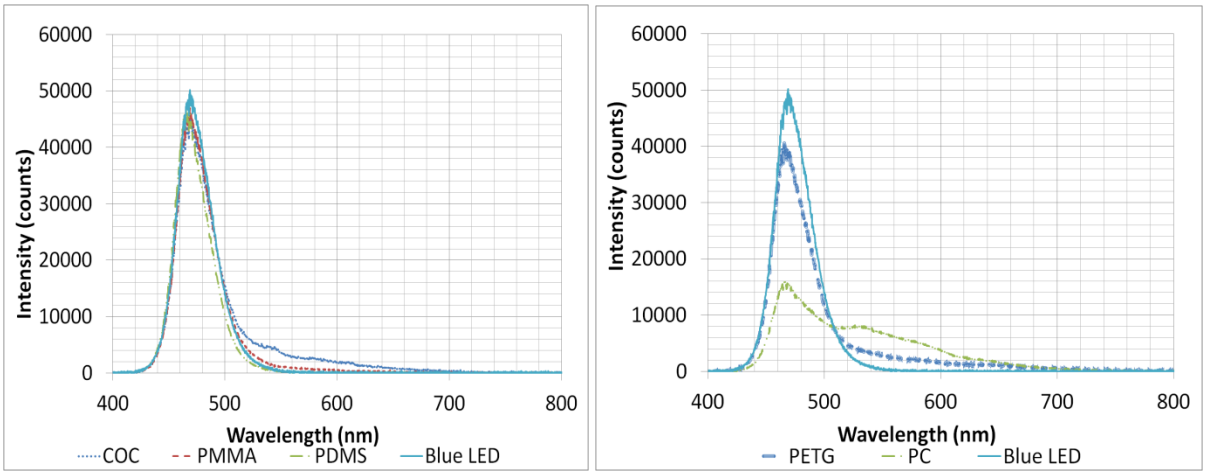

(a) (b)

Figure 4.4, (a) fluorescence spectra of COC, PMMA, PDMS (100ms integration time) (b) fluorescence spectra of PETG and PC (1s integration time)

It can be observed that the peaks and the shapes of the tails are different for different materials. The difference in peak values is due to the difference in transmittance and the difference in the shapes of the tails is due to the difference in fluorescence for different materials. The auto-fluorescence characteristic of the materials were measured and compared using a characteristic index (F'), which was reckoned as the fluorescence intensity (F) normalized by the intensity of the entire spectrum. The fluorescence intensity (F) was computed by integrating the spectrum over the range from 510nm to 720nm and then it was normalized by the factor obtained on integrating the entire spectrum over the range from 400nm to 720nm to give the characteristic index (F').

The characteristic index values of PMMA. PDMS, COC, PETG and PC are given in table 4.11. PDMS has the smallest value of characteristic index and PC has the largest. Smaller value of characteristic index means lower auto-fluorescence and/or higher transmittance. The desired material for TIRF application should possess lower auto-fluorescence and higher transmittance, hence a smaller value of characteristic index.

4.4 Selection of appropriate materials

Materials which are low cost, optically transparent with high transmittance over visible spectrum, optically polish-able, and also exhibit ease of fabrication, low auto-fluorescence with proper chemical resistance are appropriate materials for TIRF application. Materials exhibiting excellent ease of fabrication, low enough auto-fluorescence and proper chemical resistance with good enough (about 90%) optical transmittance are more appropriate than the materials exhibiting poor ease of fabrication with excellent optical transmittance. As discussed in previous sections of this chapter, Optical glass materials exhibit very good transmittance and good chemical resistance, but these materials are costly and difficult to fabricate into shape. On the other hand, plastic materials exhibit excellent ease of fabrication with proper chemical resistance

and good optical transmittance. Moreover, they are low cost, light weight and mass producible. So, plastic materials have an edge over glass materials to be used for TIRF application.

Table 4.11, characteristic index values for plastic materials; PDMS, PMMA, COC, PETG, PC

Material	Characteristic index (F')
PDMS	0.06
PMMA	0.11
COC	0.22
PETG	0.24
PC	0.54

In contrast to their classy properties, the plastics also exhibit a limiting property like auto-fluorescence. Among all the plastics studied in previous sections, plastics like PDMS and PMMA exhibit lowest levels of auto-fluorescence. In addition, they also possess good chemical resistance and best optical transmittance among all. Also, the refractive index of PDMS is lower than that of PMMA, which makes PDMS suitable as cladding material. Moreover, PDMS possess best mechanical and chemical properties which make it the most appropriate cladding material in all as these properties make it very easy to mold PDMS into any shape and size. Hence, PDMS and PMMA are the most appropriate materials among all for TIRF application with PDMS as a cladding material and PMMA as a core material. However, COC also exhibit comparable levels of auto-fluorescence and optical transmittance with better chemical resistance than PMMA. Hence, COC also can be used for TIRF application when resistance levels of the end-point application to certain chemicals are more critical.

References

[1] N. Chronis and L. P. Lee, "Total internal reflection-based biochip utilizing a polymer-filled cavity with a micromirror sidewall," *Lab on a Chip,* vol. 4, pp. 125-130, 2004.

[2] "TIE-30: Chemical properties of optical glass," March 2008. [Online]. Available: http://fp.optics.arizona.edu/optomech/references/glass/Schott/tie-30_chemical_properties_of_optical_glass_us.pdf.

[3] *ISO 8424: Raw optical glass - Resistance to attack by aqueous acidic solutions at 25°C - Test method and classification,* June 1996.

[4] *ISO 10629: Raw optical glass - Resistance to attack by aqueous alkaline solution at 50°C - Test method and classification; July 1996,* July 1996.

[5] *ISO 9689: Raw optical glass-Resistance to attack by aqueous alkaline phosphate - containing detergent solutions at 50°C-Testing and classification,* December 1990.

[6] *ISO/CD 13384: Raw optical glass - Testing of the climate resistance CR (resistance to humidity) at temperatures changing between 40°C and 50°C and classification,* January 1999.

[7] H. Bach and N. Neuroth, Eds."The properties of optical glass," 1998.

[8] M. Polyanskiy, "Refractiveindex.INFO," [Online]. Available: http://refractiveindex.info/?group=PLASTICS&material=PC.

[9] F. Schneider, J. Draheim, R. Kamberger and U. Wallrabe, "Process and material properties of polydimethylsiloxane (PDMS) for optical MEMS," *Sensors and Actuators,* vol. A 151, pp. 95-99, 2009.

[10] Topas Advanced Polymers, [Online]. Available: http://www.topas.com/sites/default/files/files/optical_en_080603.pdf.

[11] Zeonex: Cycloolefin Polymer (COP), [Online]. Available: http://www.zeonex.com/lib/pdf/zeonex_e_200809b.pdf.

[12] Filmetrics, [Online]. Available: http://www.filmetrics.com/refractive-index-database/PET/Estar-Melinex-Mylar.

[13] Topas Advanced Polymers, [Online]. Available: http://www.polyplastics.com/Gidb/GradeListDownloadAction.do;jsessionid=ea83fa0ea468

e088b8bf8625498c?brandSelected=6.1.

[14] Plastics Europe : Association of plastics manufacturers, [Online]. Available: http://www.plasticseurope.org/Documents/Document/20100301162055-050303GeneralChemicalResistanceofPET-20050303-003-EN-v1.pdf.

[15] ERIKS solutions in plastics, [Online]. Available: http://solutions-in-plastics.info/nl-be/datasheets/Transparante%20Kunststoffen/ERIKS%20-%20PMMA%20resistance%20to%20chemical.pdf.

[16] Palram, [Online]. Available: http://www.perspex.co.uk/documents/technical/chemical-resistance/Polycarbonate.pdf.

[17] BASF Plastics, [Online]. Available: http://www.styrolution.net/wa/steu~fr_FR/function/conversions:/publish/common/upload/general_purpose_styrenics/Chemical_Resistance_Styrene_Copolymers.pdf.

[18] J. N. Lee, C. Park and G. M. Whitesides, "Solvent Compatibility of Poly(dimethylsiloxane)-Based Microfluidic Devices," *Analytical Chemistry,* vol. 75, pp. 6544-6554, 2003.

[19] J. C. McDonald and G. M. Whitesides, "Poly(dimethylsiloxane) as a Material for Fabricating Microfluidic Devices," *Accounts of Chemical Research,* vol. 35, no. 7, pp. 491-499, 2002.

[20] J. R. Anderson, D. T. Chiu, R. J. Jackman, O. Cherniavskaya, J. C. McDonald, H. Wu, S. H. Whitesides and G. M. Whitesides, "Fabrication of Topologically Complex Three-Dimensional Microfluidic Systems in PDMS by Rapid Prototyping," *Analytical Chemistry,* vol. 72, pp. 3158-3164, 2000.

[21] D. C. Duffy, J. C. McDonald, O. J. Schueller and G. M. Whitesides, "Rapid Prototyping of Microfluidic Systems in Poly(dimethylsiloxane)," *Analytical Chemistry,* vol. 70, pp. 4974-4984, 1998.

[22] S. K. Sia and G. M. Whitesides, "Microfluidic devices fabricated in poly(dimethylsiloxane) for biological studies," *Electrophoresis,* vol. 24, pp. 3563-3576, 2003.

[23] A. Piruska, I. Nikcevic, S. H. Lee, A. Chong, W. R. Heineman, P. A. Limbach and C. J. Seliskar, "The autofluorescence of plastic materials and chips measured under laser irradiation," *Lab on a Chip,* vol. 5, pp. 1348-1354, 2005.

Chapter 5: Development and optimization of methods of depositing photoluminescent indicators on core surface

5.1 Introduction

After deciding upon the best suitable core and cladding materials, an optimized method for photoluminescent dye deposition on the waveguide core surface has to be developed for efficient TIR-based application. For that, the deposited dye layer should have optically smooth surface and it is desired to endure long in the presence of moderately as well as highly corrosive chemicals. Also, the thickness and surface roughness of the layer should be adequate to have more amount of excited dye giving more fluorescence strength for unit strength of scattered excitation light. For that, an adequate method of immobilizing the dye layer firmly on the core surface should be developed.

A variety of methods for attaching fluorescent dye to fiber tips have been reported in the literature including coupling dye to a polymer powder that is confined within some area by a membrane [1-3], attaching porous glass as a substrate for covalent indicator immobilization [4], confining a thin layer of dissolved indicator behind a hydrophobic, gas-permeable membrane [5]. All of these methods have their advantages and disadvantages, but none of them provide firm and smooth immobilization of dye on planar surface. So, none of them can be used for adequate TIR-based implementation. Some other methods of covalently bonding polymer-bound dye molecules directly to a glass substrate are also demonstrated [6, 7]. But, there is no information available about the usefulness of these methods for depositing dye on planar core surfaces for TIR-based application. Since, the core materials to be used in the final TIR-based design are thermoplastics, reliability of methods of bonding dye molecules to thermoplastics have to be tested.

As discussed earlier, a photoluminescent dye could be fluorescent or phosphorescent depending on the excitation-emission mechanism and lifetime. The excitation-emission mechanism depends on the chemical and quantum configuration of the dye molecules. Moreover, the ability and the method of depositing dye as well as the characteristics of deposited dye layers depend on their chemical configurations. For that reason, adequate dye deposition methods for different dye molecules may not be the same. In this study, deposition methods for two different photoluminescent dyes are developed and optimized for adequate implementation of TIR-based concept. One of them being fluorescenamine; a pH sensitive fluorescent dye; and the other being dichlorotris(triphenylphosphine)rutheniumII (Ru(dpp)); an O_2 sensitive phosphorescent dye.

In section 5.2, sample preparation and test criteria used to compare different methods of deposition are discussed. In section 5.3, the pursuit of an adequate deposition method for a pH sensitive dye; fluorescenamine; is presented. In section 5.4, the entire pursuit of an adequate deposition method for a O_2 sensitive dye; $Ru(dpp)^3$; is presented.

5.2 Standardization of sample preparation, test protocol and test criteria

As discussed earlier, an adequate method of dye deposition should be developed for efficient implementation of TIR-based concept. For that, different methods should be tried and compared to check for adequacy using a standardized test protocol based on some standardized criteria. Dye is to be deposited on the surface of core material. It becomes easier to define a general standardized protocol for testing different deposition methods for adequacy when the characteristics of material samples used to try different methods on are identical for method by method. For that, the characteristics of material samples like size, shape and roughness should be standardized as well.

5.2.1 Sample preparation

As concluded in chapter 4, PMMA and COC are the most suitable materials for waveguide core. So, the size and the shape of samples made of these materials have to be standardized. One way to do this is to keep the dimensions of the samples the same as that of the core in the final TIR-based design. But, the size and shape of the core of the final TIR-based device depend mainly on the shape and size (dimensions) of fluidic channel, optical fiber and deposited dye layer. Also, the dimensions of the fluidic channel are functions of dimensions of deposited dye layer and optical fibers. Also, the diameter of fiber should support multi-mode light propagation for more coupling of light power than single mode fiber by the same fluorescence source. Hence, knowing the dimensions of the deposited layer is the key to know the required exact dimensions of the core in the final TIR-based design. For that, knowledge of the method of deposition is important. And hence, the dimensions and shape of the samples cannot be standardized based on the exact core dimensions before knowing anything about the deposition method. However, it can be standardized based on approximated core dimensions, which can be estimated by approximating the deposition surface area, fiber diameter and channel dimensions.

Methods of covalently bonding polymer-bound dye molecules [6, 7] use aqueous solution of polymer-bound dye and cross linking agent to be put on the surface before the water is evaporated and dye is firmly immobilized. The water content in these aqueous solutions usually exceeds 80%. So, major portion of the aqueous solution is water. Therefore, the surface area of dye layer deposited on the core surface can be approximated by measuring the surface area covered by the same amount of water deposited on the core surface. Moreover, multi-mode light coupling requirements can be satisfied by using 980μm diameter plastic optical fiber as a collecting fiber. The normalized frequency of 980μm diameter POF is ≈ 2842, which supports

enormous number of modes. As the cross sectional area of the POF fiber is about 1 mm^2, a number of different values of water volume were tried to have water deposition surface area of ≈2mm^2 to keep the deposition area larger than fiber cross section area to account for tolerances in alignments. After several trials, deposition surface area of 2mm^2 was obtained for 5µl of DI water volume. Based on the deposition layer and fiber dimensions, the width of the fluidic channel incorporating the deposition layer is approximated to be about 4mm allowing for tolerances. Also, the channel length is approximated to be 10mm to incorporate fluid reaction area with 1mm diameter inlet and outlet holes and a 1mm hole for collecting fiber. So, based on the dimensions of fluidic channel, the required core width and length are approximated to be 10mm and 20mm respectively. And the required thickness of the core is assumed to be 2mm, which is larger than the POF diameter (≈1mm). So, 10mm x 20mm sized slabs were cut for use as samples from 0.090'' (≈2.2mm) PMMA sheet using CO_2 laser-cut machine by commercial plastic vendors.

So, preparing 10mm x 20mm x 2.2mm sized PMMA samples using CO_2 laser-cut machine is a standardized protocol of preparing samples for testing different methods of dye deposition.

5.2.2 Test protocol and test criteria

A number of methods were tried seeking for the most adequate method of deposition. Every method was tested according to some standard criteria following a standard protocol for testing. The protocol was to measure a spectrum of deposited layer and then look for peak of auto-fluorescence, of chemical substrate used for deposition and calculate a scattered excitation light strength to fluorescence strength ratio. Surface roughness of the deposited layers and refractive index were also measured when needed. The criterion was to compare different

methods based on presence and strength of auto-fluorescence and the scattered excitation light strength to fluorescence strength ratio. Deposition methods that gave auto-fluorescence peaks of deposition substrate or/and give the scattered excitation light strength to fluorescence strength ratio greater than 1:1 were not considered adequate for TIR-based application. Methods with no auto-fluorescence and good ratio were tested for the refractive index and surface roughness of deposited layers, and ones that gave refractive index value smaller than that of the core material and gave small enough value of surface roughness were considered adequate for TIR-based application. Methods considered adequate based on these protocol were again tested to check if the deposited layer lifts off with 1hour's exposure to DI water OR if the dye molecules leach off the deposited layer.

While trying different methods of deposition, it was taken care of that the deposited layer be measured at the geometric center of the sample surface and at least 2mm-5mm off the sample edges to avoid the excitation light scattered off the edges from being caught by the collection fiber. The spectra of deposited dye layers were measured following a standardized procedure and using a standardized setup. The setup is illustrated in figure 5.2. As shown in figure 5.2(a), the SMA connected end of the excitation fiber, coupled with an LED, was aligned normal to the 10mm side of the samples so that the fiber was touching the 10mm side at the center. The excitation LED was driven by 30mA current through a current supply. As shown in figure 5.2(b), the fluorescence spectrum was measured using a fluorescence spectrometer (USB4000 FL, OceanOptics) with the collecting fiber collecting fluorescence in the normal direction to the sample surface with the fiber touching the deposition layer surface and 5mm off the excited edge.

Different methods of depositing the pH sensitive fluorescenamine dye and O_2 sensitive $Ru(dpp)^3$ dye were tried and tested for adequacy following the same standardized protocol based on the same standardized criteria. The excitation LED used for testing was fiber coupled 470nm LED, as the excitation wavelength for fluorescenamine and $Ru(dpp)^3$ is 470nm. Different methods of deposition included mixing the dye with +ve photoresist and then spin casting a thin layer of the dye-resist conjugate, incorporating the dye molecules into the core surface by targeting the surface using dye's solution in the solvent of core material, gluing the dye molecules to the core surface using Si adhesive gel, covalently bonding polymer-bound dye molecules. All these methods and their test results are discussed in the following sections.

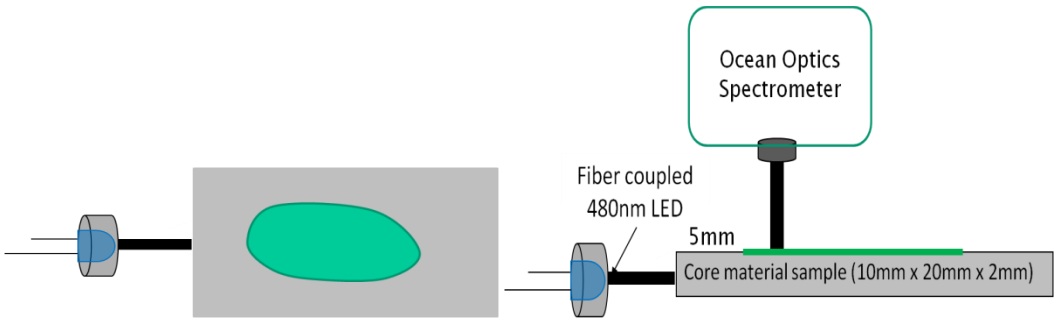

Figure 5.2, (a) schematic top-view of test apparatus setup (b) side-view of test apparatus setup

5.3 Methods for depositing fluorescenamine

5.3.1 Incorporating dye into the core surface using its solution in acetone

Fluorescenamine is miscible in polar solvents like ethanol, iso-propanol, acetone etc. Among these solvents acetone is a very good solvent for PMMA too. So, in this method of deposition, a solution of fluorescenamine isomer I (201626 ALDRICH) in acetone (320110 SIGMA-ALDRICH) with 1.38 % w/w concentration was made. Type X solution (1.38% w/w)

contained 5mg of fluorescenamine isomer dissolved in 500mL of acetone. The solution X in 20µL quantity was put on PMMA core sample and tested by spectrum inspection. Picture of this sample is given in figure 5.3(a). The fluorescence spectrum of this deposited layer was measured using the standardized protocol. The spectrum is shown here in figure 5.3(b).

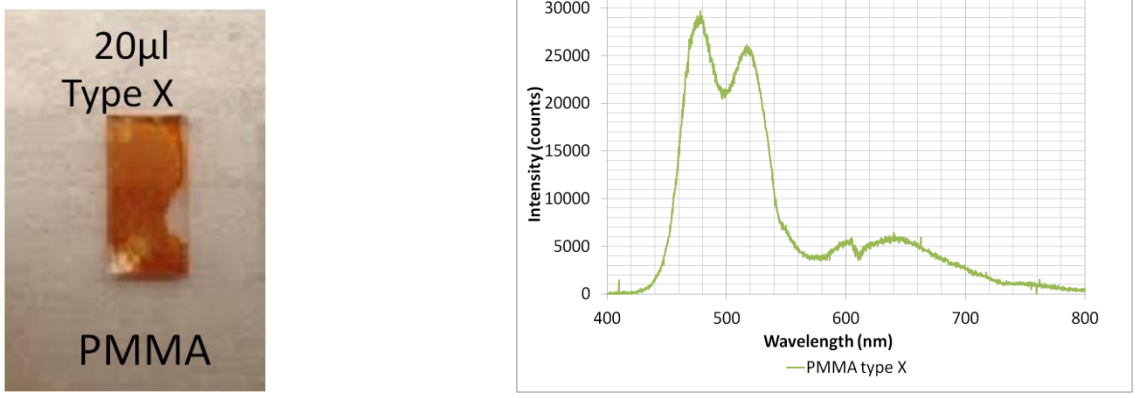

(a) (b)

Figure 5.3, (a) pictures of deposited solution X and solution Y (b)

As seen from the figure 5.3(b), this deposition method gives unwanted fluorescence peak at 650nm. The fluorescence peak at 520nm is fluorescence of fluorescenamine, which is of more interest. The fluorescence peak at 650nm is not seen in PMMA auto-fluorescence spectrum given in chapter 4. So, this deposition method happens to be not "good" for TIR-based application. Moreover, after this spectrum was taken for type X, the sample was kept in DI water for an hour and then blow dried with N_2. Fluorescenamine powder was observed to be leaching off the surface while the treatment. And after the treatment the sample did not show 520nm peak or 650nm peak in the spectrum. The picture of the sample and its spectrum after the treatment are given in figure 5.4. This result confirmed that this method of deposition is not "good", as dye could not be firmly immobilized as well.

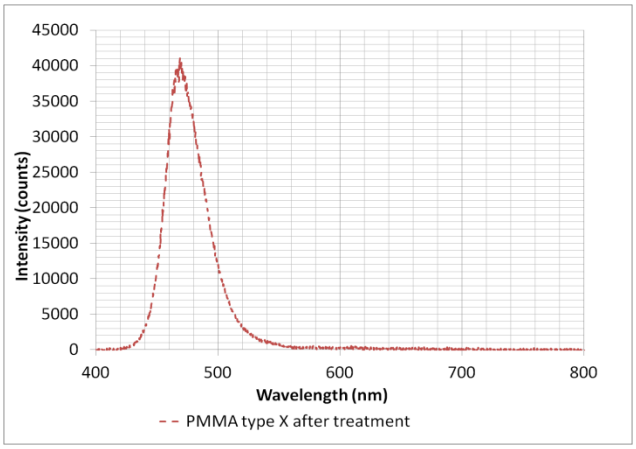

(a) (b)

Figure 5.4, (a) type X PMMA sample after water treatment (b) spectrum of type X PMMA sample after water treatment

5.3.2 Spin coating the mixture of dye-acetone solution and AZ1518 positive photoresist

The attempt to immobilize dye firmly on the sample surface using acetone was not successful. So, the attempt to immobilize dye should be made using some substrate that sticks to the surface firmly. Photoresists are such substrates that can be put on the PMMA surface to be stuck there robustly. So, the type X solution of fluorescenamine in acetone was mixed with AZ1512 positive photoresist in 1:1 proportion, and the mixture thus made was named type I solution. Then, the type I solution was spun on the PMMA surface. Different volumes of type I solution were tried to be put on the surface in order to cover the whole surface. The whole surface of the 10mm x 20mm PMMA sample was successfully covered by 50µl of the type I solution. Then, different rotation speeds of the spinner were tried to obtain a thin layer of deposition. After trying each different rotation speed the thickness of the layer was visually observed. The thinnest layer before losing significantly high amount of the type I solution from the surface was obtained for 4000 rotations per minute for 2 minutes. A photograph of the sample prepared like this is shown in figure 5.5(a). Upon exciting the sample, amber-colored

auto-fluorescence of the resist substrate was visible. This is shown in figure 5.5(b). The spectrum was taken based on the standard protocol, which is shown in figure 5.5(c). It is evident that the

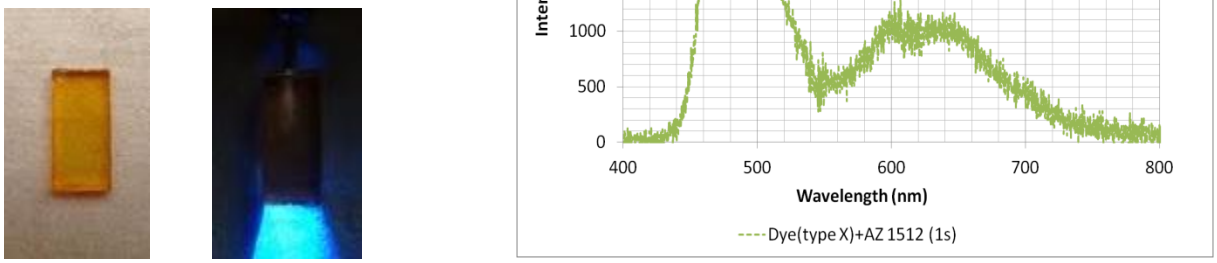

(a) (b) (c)

Figure 5.5, (a) type I coated PMMA sample (b) auto-fluorescence picture of type I coated sample (c) spectrum of type I coated sample

spectrum has 650nm peak. This 650nm peak could be due to the same reason we had this peak in the spectrum of deposited layer discussed in last section. To confirm that, the type I coated sample of this method was water treated for 1 hour and then the spectrum was taken again. During the water treatment, there was not any dye leaching off the layer. And the spectrum of the water treated sample had the same 520nm and 650nm peaks. So, this method was successful in immobilizing dye firmly on the surface. But, the cause of 650nm peak was unknown. It could be because of the unwanted auto-fluorescence of AZ1512. Therefore, a PMMA sample was prepared by spin coating just the AZ1512 photoresist with 4000 RPM for 2 minutes to confirm the cause. The picture of this sample is given in figure 5.6(a).

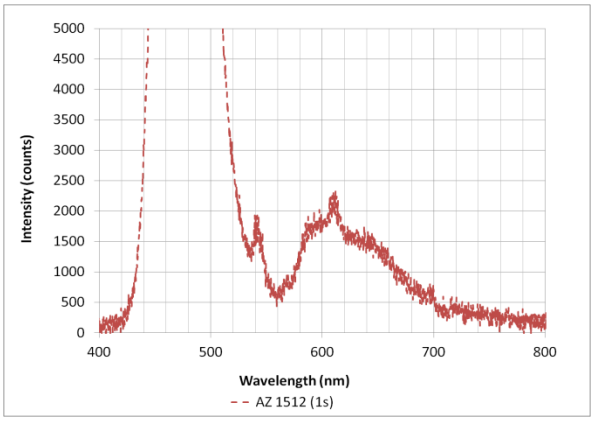

(a) (b)

Figure 5.6, (a) picture of AZ1512 coated PMMA sample (b) spectrum of AZ1512 coated sample

The spectrum was taken based on the standard protocol, which is shown in figure 5.6(b). The amber-colored auto-fluorescence of AZ1512 is visible in the picture. These results confirm the cause of 650nm peak in the type I sample to the presence of AZ1512. In addition to the 650nm auto-fluorescence peak, this method gives 520nm scattered excitation light strength to fluorescence strength ratio of about 2:1. But, it is logical to believe that the ratio can be decreased by simply increasing the thickness of the deposited layer. If it can be done then apart from the 650nm fluorescence peak, this method satisfies all other test criteria. It is because by spin coating the type I solution pretty smooth (optically smooth) deposition surface can be obtained. Therefore, this method of dye deposition was considered contingently adequate and the quest for the most adequate deposition method was kept on.

5.3.3 Using poly(vinyl alcohol) as a substrate for depositing fluorescenamine dye

This method was first demonstrated by Zhujun Zhang in 1989. He used this method for immobilization of dye on fiber tips. In this study, the method was tried for dye immobilization on PMMA plane surface. Zhujun studied the effect of dye amount and layer thickness on the fluorescence. In this study, the effect of dye amount and layer thickness on the scattered

excitation light strength to fluorescence strength ratio is studied in order to determine the adequate amount and/or thickness of the dye based on the standardized criteria. Zhujun's method of deposition uses cyanuric chloride to couple fluorescenamine with poly(vinyl alcohol) which is then cross-linked by glutaraldehyde in the presence of hydrochloric acid. The method has two important features. First, dye is covalently bonded to PVOH prior to the cross-linking step. The second is that the rate of the crosslinking reaction can be controlled by varying the amount of acid catalyst (HCL). Under the conditions normally employed, the rate of cross-linking is sufficiently slow to allow the glutaraldehye/ PVOH solution to be manipulated as a liquid before it solidifies. The chemistry of how this method works is shown in figure 5.7.

In this study, a protocol for the amount and/or concentration of HCL is developed to optimize the solidification time and amount of crosslinking (swelling index). It is developed based on the information presented by Zhujun et al. The information on the dependence of solidification time and swelling index on the amount and/or concentration of HCL is given in figure 5.8, which is reproduced from Zhujun et al. Swelling index depends on the amount of PVOH and gluteraldehyde as well. Therefore, swelling index was not optimized while the effect of different amount of dye on the fluorescence was studied. While optimizing solidification time, different amount of HCL acid were tried with 5µl of 10% (w/w) PVOH and 1 µl of 2.5% gluteraldehyde to obtain solidification time of 4-5 minutes.

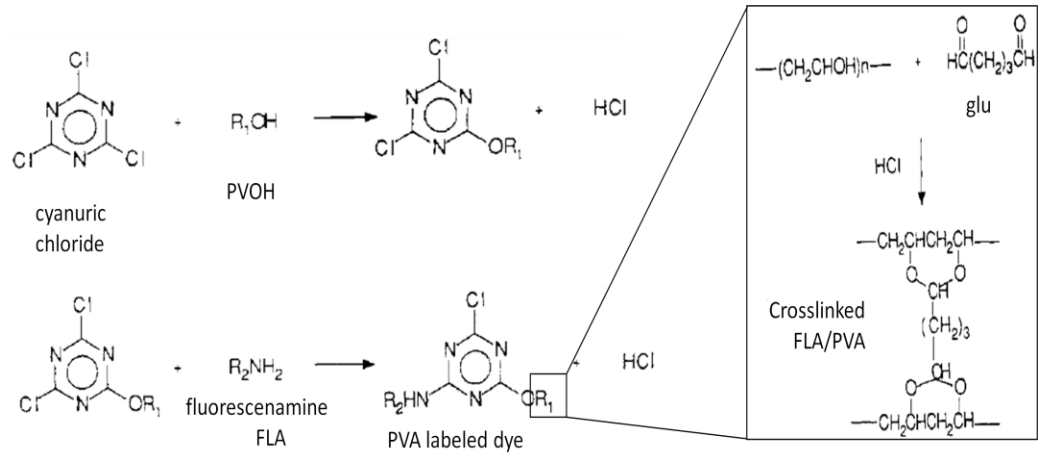

Figure 5.7, Use of poly(vinyl alcohol) as a substrate for dye immobilization, reproduced from [7]

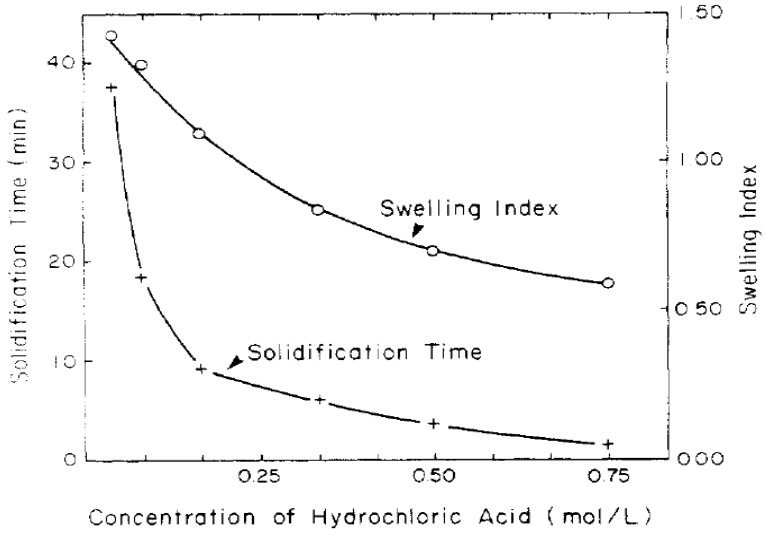

Figure 5.8, swelling index and time required for solidification as a function of HCL concentration

Solidification time of 4-5minutes is required to give good enough time to put the PVOH/fluorescanamine/gluteraldehyde liquid on the PMMA surface before the substrate solidifies. The result of a number of trials confirmed 1.5M concentration of HCl to give 4-5 minutes of solidification time for given PVOH and gluteraldehyde amount and concentration. So, 1.5 M HCl concentration was standardized and used in all the experiments done to determine the effect of amount of dye and thickness of layer on the fluorescence strength.

For the experiments to investigate the effect of amount of dye, the amount of PVOH labeled fluorescenamine was changed by changing the % (w/w) concentration for the known constant volume (5ul) of it. Three PMMA-based samples were prepared by using a mixture of 5µl of x % (w/w) PVOH-fluorescenamine, 1ul of 2.5% gluteraldehyde and 1ul of 1.5M HCl and by changing the value of x to be 1, 10 and 20 respectively. The spectra of these samples were measured using the standard protocol after the layers were solidified and the results were compared based on the standard criteria. The spectra of the samples are given in figure 5.9. In the figure PVA-FLA is acronym used for PVOH labeled fluorescenamine.

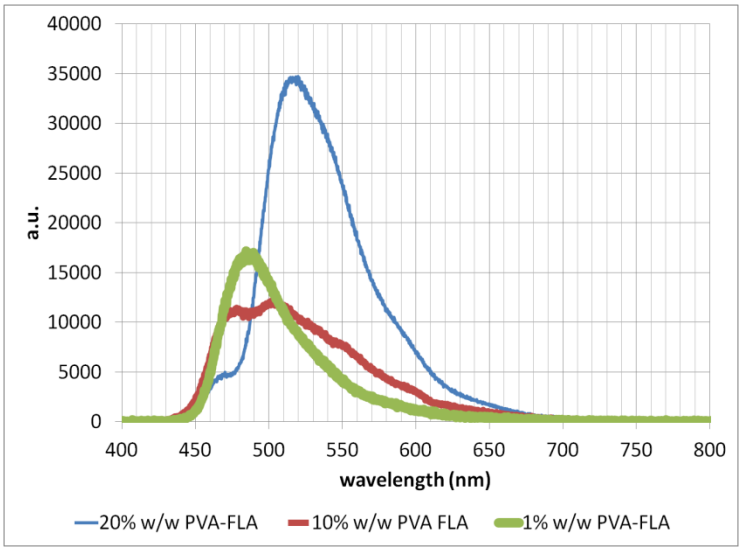

Figure 5.9, effect of amount of dye on fluorescence peak for PVA labeled dye

It is evident from the figure that as the amount of dye increases the fluorescence peak (520nm) also increases and scattered excitation light peak (470nm) decreases. The increase in fluorescence peak is intelligible as an increase in the amount of dye (amount of PVA-FLA) means more amount of excited dye per unit strength of absorbed excitation light per unit area and that in turn means more fluorescence intensity. The decrease in scattered excitation light peak is also understandable as an increase in amount of PVA-FLA for constant amount of diluter (water)

means smaller degree of dilution and larger swelling index [8] that means relatively less porous substrate that in turn means more optically smooth interface between the deposited layer and PMMA surface, means smaller amount of scattering at the interface.

Now for the experiments to investigate the effect of thickness of deposited layer, the number of deposited layers was changed to change the thickness of the effective deposited layer. Three PMMA samples were prepared by making the number of deposited layers to be 1, 3 and 5 respectively. Each such layer was deposited by transferring a mixture of 5ul of 10 % (w/w) PVOH-fluorescenamine, 1ul of 2.5% gluteraldehyde and 1ul of 1.5M HCl to the sample surface. The spectra of these samples were measured using the standard protocol after the layers were solidified and the results were compared based on the standard criteria. The spectra of the samples are given in figure 5.10(b). A picture of the PMMA sample with 3 layers of deposition is shown in figure 5.10(a). In the figure 5.10 (b) PVA-FLA is acronym used for PVOH labeled fluorescenamine.

It is evident from the results that fluorescence intensity can be increased by increasing the number of layers. More number of layers means more amount of excited dye per unit strength of absorbed excitation light per unit area and that in turn means more fluorescence intensity. Also, it is observed that the peaks of the scattered light for different samples in this case are not changed significantly. It is intelligible as addition of more layers does not change the porosity of the deposition at the interface and therefore the effective optical roughness at the interface is not changed for different samples.

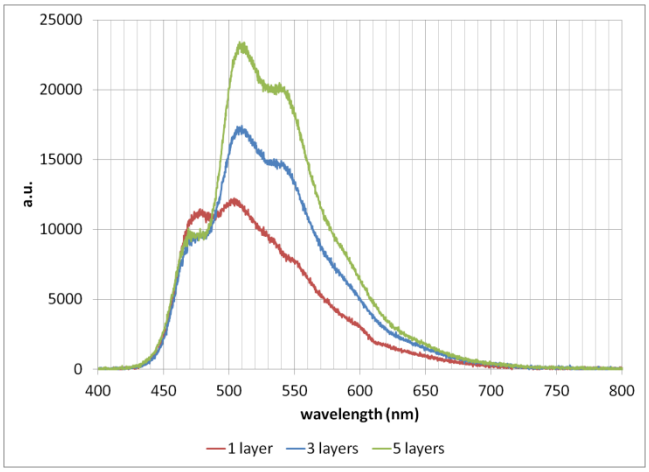

(a) (b)

Figure 5.10, (a) picture of PMMA sample with 3 layers of deposition (b) spectra of PMMA samples for 1, 3 and 5 deposition layers

Thus, the scattered excitation light strength to fluorescence strength ratio can be decreased either by increasing the amount of dye or by increasing the thickness (increasing the number of layers). So, based on the criterion related to the ratio, this method of deposition is adequate for proper amount of dye and proper thickness. Also, there is not any other auto-fluorescence peak available in the spectrum. Hence, this method is the most adequate method among all discussed in this chapter.

It is wise to confirm the adequacy for the surface roughness and refractive index requirements. For that, the surface roughness was measured for the PMMA sample with 3 layers using ZeScope optical profilometer. The result of the measurement is shown in figure 5.11. The RMS and average roughness of the deposition layer were measured to be 11.9nm and 6.50nm respectively, which are very small values compared to the wavelength of interest (520nm). Very small values of roughness confirmed the adequacy based on the roughness requirements. Thickness of the deposition was also measured to be 40μm, the result is shown in figure 5.12. Based on this thickness information ellipsometric measurements were taken for the same sample

to determine the refractive index of the deposited layer. Simple calculations of refractive index were carried out in thin film calculation software (TFcalc) using the values of delta and psi obtained from the ellipsometric measurements. The procedure followed for the ellipsometric measurements and for the TFcalc calculations is explained in appendix D. The results gave the refractive index of the deposited layer to be 1.47 at 632.8 nm, which is smaller than the refractive index value of PMMA material (1.49).

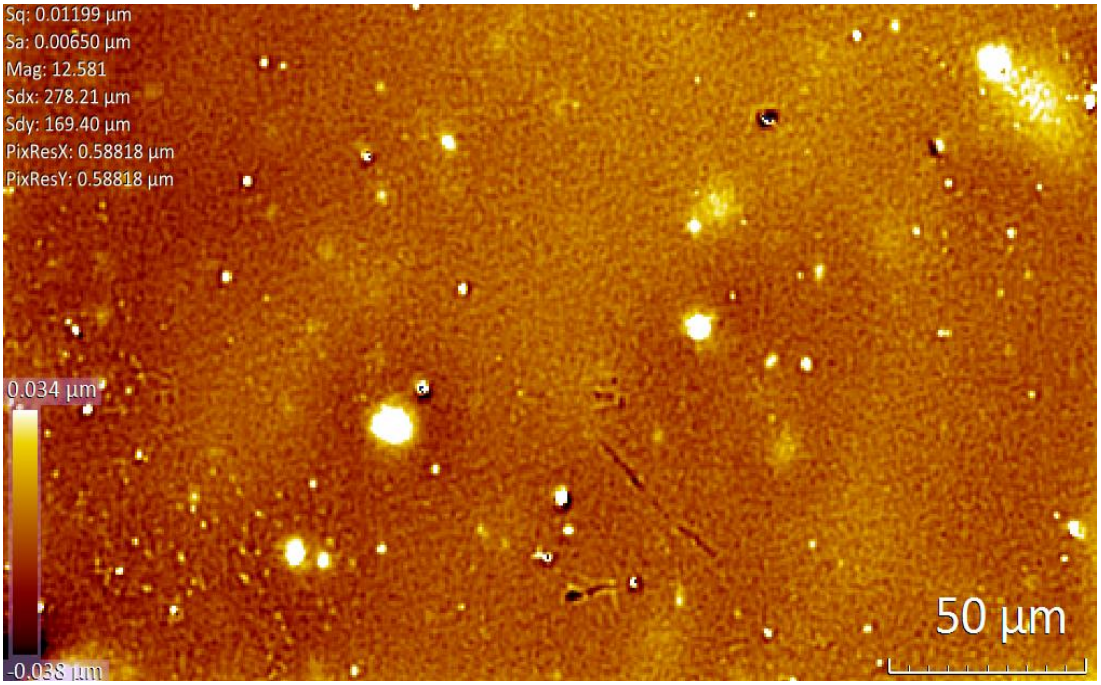

Figure 5.11, surface roughness profile for the PMMA sample with 3 layers of deposition, produced by the ZeScope profiler software

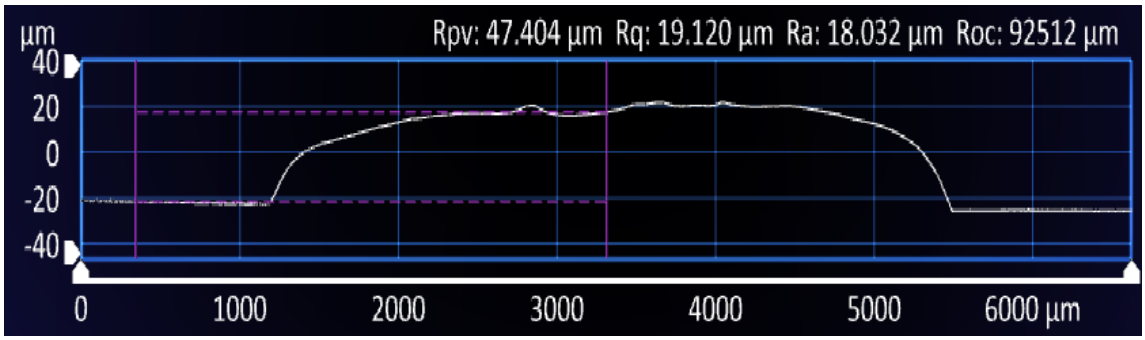

Figure 5.12, thickness profile of PMMA sample with 3 layers of deposition

Hence, this deposition method is the most adequate method of all discussed in this chapter based on mostly all of the standardized criteria. Finally, the firmness of the immobilization obtained by this deposition method was tested. For that, 8 samples of PMMA were prepared with 1 layer of deposition using a mixture of 5ul of 10 % (w/w) PVOH-fluorescenamine, 1ul of 2.5% gluteraldehyde and 1ul of 1.5M HCl. And all the samples were kept in DI water for 1 hour. Then, the samples were removed from water. On observation of the samples after letting all the water evaporate, it was observed that the deposited layers for 3 of the samples were completely peeled off and for another 3 of the samples they were partially peeled off and for the rest of the samples they were completely intact and firmly immobilized. So, this method had been successful in keeping the deposited layer firmly immobilized on the surface for just above 50% times. Though, this was so far the most adequate method of all.

However, for implementing the final pH-sensing TIR-based device, it might not be a successful method because of the low success ratio and poor repeatability. Therefore, some other methods of deposition based on Si adhesives and polymer substrate were also tried for better adhesion of dye molecules on the PMMA surface. These methods are discussed along with the implementation and characterization of pH-sensing TIR-based device in chapter 7 of this thesis work.

5.4 Deposition method for Dichlorotris(triphenylphosphine)rutheniumII – Ru(dpp) dye

5.4.1 Use of Si-based clear adhesive gel for deposition of Ru(dpp)

Si-based clear adhesive gel is generally made of Siloxane compounds and the main ingredient of it is poly(dimethylsiloxane). The refractive index of poly(dimethylsiloxane) is 1.44, which is smaller than that of PMMA. So, if this adhesive gel can immobilize dye firmly on the PMMA surface, then it may be used as an adequate method of deposition for ruthenium based phosphorescent dye $Ru(dpp)^3$. For that, a method of mixing the $Ru(dpp)^3$ dye with Si gel should

be developed. Si-based clear adhesive form is miscible with any polar or non-polar solvent when it is in its uncured form. On the other hand, $Ru(dpp)^3$ is available in powder form which is miscible in organic non-polar solvents like chloroform and more [9]. So, chloroform was used to mix the dye with Si clear adhesive gel.

Several solutions of dye and Si gel in chloroform were made with different % (w/v) concentrations. PMMA samples were prepared by putting 5µl of these solutions and then the samples were visually inspected to observe the viscosity of the solutions. Viscosity of the solution is important property to consider as it governs the thickness of the deposited layer. Moderately viscous solution is desired to have moderately thick deposition layer. Based on visual inspections of several samples, samples prepared using the mixture of 200mg Si gel, 1mg $Ru(dpp)^3$ and 0.5ml chloroform were observed to have more thick deposition layers. And samples prepared using 200mg Si gel, 1mg $Ru(dpp)^3$ and 1.5ml chloroform were observed to have moderately thick deposition layers. Therefore, the solution made by mixing 200mg Si gel, 1mg $Ru(dpp)^3$ and 1.5ml chloroform was defined as the standard solution for this deposition method. Several PMMA samples were prepared using 5µl drops of the standard solution. And these samples were tested for adequacy by measuring their spectra following the standardized protocol and then by comparing the spectra based on the standard criteria. The results of spectrum measurement are given figure 5.13. Figure 5.13(a) shows a picture of one such sample and figure 5.13(b) shows the measured spectrum for that sample. The 470nm peak in the spectrum is of scattered excitation light and the 610nm peak is of $Ru(dpp)^3$ phosphorescence. Ru(dpp)3 exhibits stoke's shift of about 130nm.

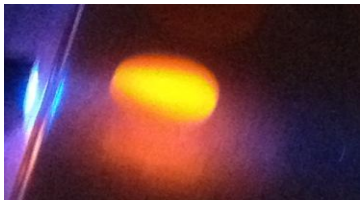

(a)

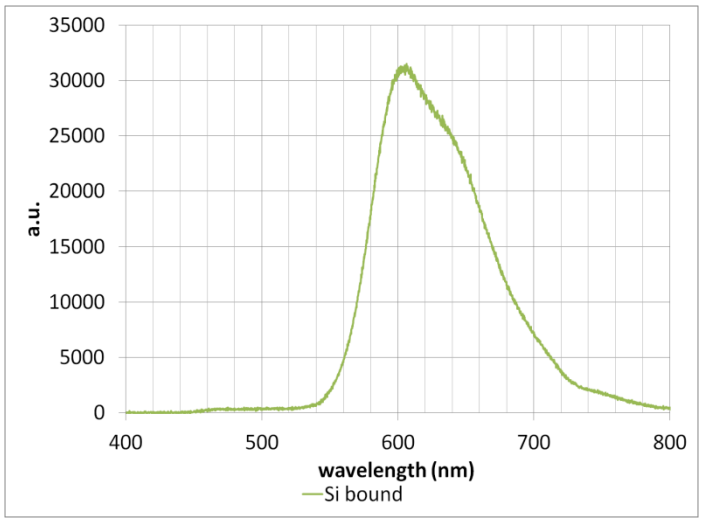

(b)

Figure 5.13, (a) a picture of PMMA sample prepared using Si-gel based $Ru(dpp)^3$ deposition (b) spectrum measurement result for the $Ru(dpp)^3$ deposited PMMA sample

The 470nm peak in the spectrum is very small compared to the 610nm peak of fluorescence. It gives the fluorescence peak to scattered excitation light peak to be about 30:1, which is excellent for TIR-based application. Also, there is not any unwanted auto-fluorescence peak present in the spectrum. Therefore, based on these primary criteria this method is excellently suitable for TIR-based configuration. Moreover, the samples were treated with DI water by keeping them in water for an hour, and during and after the water treatment there was not any leaching out of $Ru(dpp)^3$ was observed. The deposited layer was found to be firmly bound to the sample surface after the water treatment. Also, the surface roughness, layer thickness and refractive index of deposition were measured to test the adequacy based on the standard criteria. The results of the layer thickness measurements are given figure 5.14.

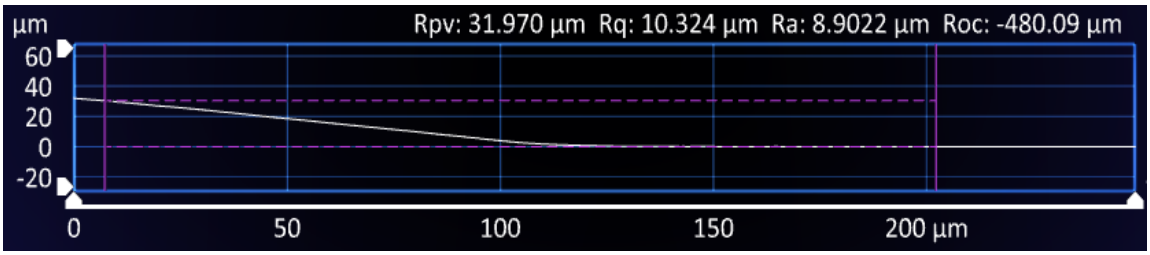

Figure 5.14, thickness profile of Ru(dpp)3 deposited layer

The thickness is measured to be 30µm. Based on this thickness information ellipsometric measurements were taken for the same sample to determine the refractive index of the deposited layer. Simple calculations of refractive index were carried out in thin film calculation software (TFcalc) using the values of delta and psi obtained from the ellipsometric measurements. The procedure followed for the ellipsometric measurements and for the TFcalc calculations is explained in appendix D. The results gave the refractive index of the deposited layer to be 1.45 at 632.8 nm, which is smaller than the refractive index value of PMMA material (1.49).

Considering all the standardized criteria, use of Si-based clear adhesive gel gives an excellent method for depositing $Ru(dpp)^3$ on sample surface. So, the same method was used to implement O_2 based biosensors for sensing H_2O_2 and lactose. O_2 based bio-sensing implementations of TIR-based device are discussed in more detail in chapter 8 of this thesis work.

References

[1] Peterson, J. I.; GoMstein, S. R.; Fkzgerald. R. V.; BuckhoM, D. K. "Fiber Optic pH Probe for Physiological Use" Anal. Chem. 1980, 52, 864-869.

[2] Peterson, J. I.; F kzgerald, R. V.; BuckhoM, D. K. "Fiber-optic Probe for in Vivo Measurement of Oxygen Partial Pressure" Anal. Chem. 1984. 56 62-67.

[3] Klrkbright, G. F.; Narayanaswamy, R.; Weltl, N. A. "Studies with immobilized chemical reagents using a flow-cell for the development of chemically sensitive fibre-optic devices" Analyst 1984, 709, 1025-1 028.

[4] Fuh, M. S.; Burgess, L. W.; Christain, G. D. "Single Fiber-optic Fluorescence Enzyme-based Sensor" Anal. Chem. 1988, 60, 433-435.

[5] Vurek, G. G.; Feustel, P. J.; Severlnghaus, J. W. "A fiber optic pco2 sensor" Ann. Biomed. Eng. 1983, 11, 499-510.

[6] Munkhoim, C.; Wait, D. R.; Mllanovlch, F. P.; Klainer, S. M. "Polymer Modification of Fiber Optic Chemical Sensors as a Method of Enhancing Fluorescence Signal for pH Measurement" Anal. Chem. 1988, 56, 1427-1430.

[7] Zhujun, Z.; Zhang, Y.; Wangbai, M.; Russell, R.; Shakhsher, Z.M.; Grant, C.L.; Rudolf Seitz, W. "Poly(viny1 alcohol) as a Substrate for Indicator Immobilization for Fiber-optic Chemical Sensors" Anal. Chem. 1989, 67, 202-205.

[8] Okay, O. "Macroporous copolymer networks" Prog. Polym. Sci. 25 711–779 2000

[9] Sabo-Etienne, S.; Gellier, M., "Ruthenium: Inorganic and Coordination Chemistry", Encyclopedia of Inorganic Chemistry, 2006, John Wiley & Sons. doi:10.1002/0470862106.ia208

Chapter 6: Fabrication of plastic total internal reflection (TIR) based device

6.1 Introduction

Development and optimization of dye deposition methods for efficient implementation of TIR-based concept are discussed in last chapter. The problem of fabricating such a TIR-based device using plastic materials is addressed in this chapter. As discussed earlier, TIR-based concept incorporates fluidic channel, deposited layers, optical waveguide and excitation and collection optics, all in a single device. So, the problem really is to develop a fabrication technique to incorporate all these elements into a single device.

Pursuing the solution, the first step would be to decide upon the dimensions of core and fluidic channel based on the information we have about the dye deposition method and excitation-collection optics. The development of device dimensions and geometry are discussed in section 6.2. Furthermore, as concluded in chapter 4, PMMA suits for waveguide core and PDMS suits for the cladding and for making fluidic channel into it due to its excellent molding properties. So, the preparation of PMMA core slabs and PDMS fluidic channels based on the decided device geometry are discussed in section 6.2. In section 6.3, development of a technique for bonding PDMS-cladding and PMMA-core integrating fluidic channel and excitation-collection optics into a single device is discussed. In section 6.4, the method used to test the fabricated devices and the results of the test are discussed, along with the improvements made in the device design and fabrication technique.

6.2 Device geometry

The goal of this section is to discuss the development of device geometry using the information about the deposition methods, dimensions of deposited layers and dimensions of excitation-collecting fibers. The required dimensions of the fibers for efficient and abundant

collection of fluorescence were discussed in chapter 5. It was concluded to have multi-mode fibers with fiber diameter to be ≈ 1mm. Therefore, plastic optical fibers (SH4001-1.3 980μm core diameter custom order, Industrial Fiber Optics) were used for excitation and collection optics. Moreover, as discussed in chapter 5, the channel dimensions depend on the dimensions of the deposited dye layers and fibers. The deposition layer surface area was estimated to be ≈2mm^2, due to the lack of information on deposition method. Since we now have the information on deposition method, the exact value of deposited layer's surface area can be calculated. For that, the deposition method for fluorescenamine using polyvinyl alcohol as a substrate was considered a standard. And the deposition method using Si-based adhesive gel was considered a standard for Ru(dpp)^3. The pictures of samples prepared using these two deposition methods are given in figure 6.1.

(a) (b) (c)

Figure 6.1, (a) layer of deposited Ru(dpp)3 (b) layer of deposited FLA-PVA (c) reference scale

Figure 6.1(c) shows a reference scale with 1mm mark. Figure 6.1(b) shows a picture of deposited layer of Ru(dpp)^3 using Si-gel. And it can be reckoned that the deposited layer's surface area for it is ≈2mm^2. Figure 6.1(c), shows a picture of deposited layer of FLA-PVA using PVA substrate. And it is evident that the surface area for this is ≈1.5mm^2. This information confirms that the estimated value of 2mm^2 for deposition surface area is actually a factual value

of deposited surface area. Thus, all the approximated dimensions of the fluidic channel, fluid inlet-outlet holes and excitation-collection fibers and core slab hold true. Therefore, the dimensions of the fluidic channel were finalized to be 3mm x 10mm x 1mm. It was decided considering possible misalignments in the fabrication. Based on that, the dimensions of the core were finalized to be 10mm x 20mm x 3mm. Thus, the primary geometry of the final device was decided, which is shown in figure 6.2. This geometry drawing was developed using autoCAD development tool. Figure 6.2(a) is home view of the final device and figure 6.2(b) is up-side-down front view of the device. The dimensions are in the scale: 1 unit = 20mm.

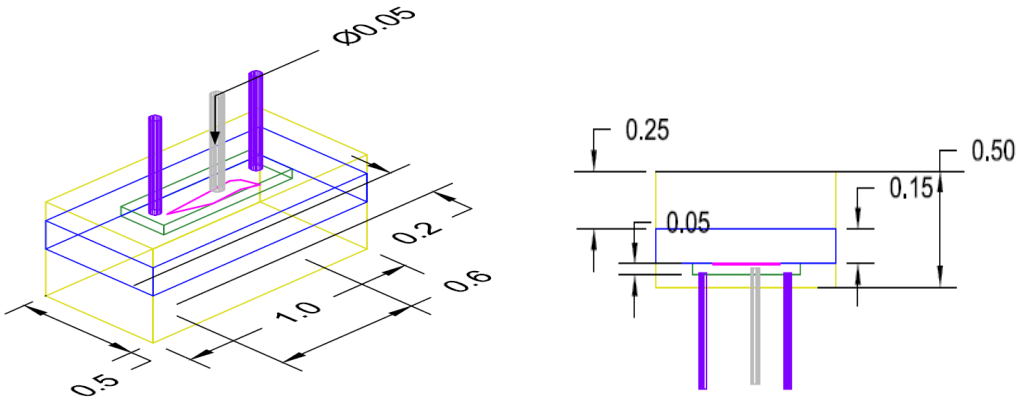

(a) (b)

Figure 6.2, (a) home view of 3D drawing of primary device geometry (b) upside-down front view of 3D drawing of primary device geometry

Slabs drawn with yellow outline are PDMS material slabs. PMMA core is drawn with blue outline. The channel is shown in green outline. And the magenta colored outline depicts deposited dye layer. The purple colored cylinders penetrating through the upper PDMS slab's top surface depict inlet and outlet tubes through inlet and outlet holes. The white colored cylinder depicts collection fiber. The diameter of these inlet, outlet and collecting fiber holes is 1mm.

6.3 Preparation of PMMA core slabs and fabrication of PDMS upper and lower cladding

In this section, development of fabrication technique for making PDMS upper and lower cladding slabs is discussed. PMMA core slabs and PDMS cladding slabs should be prepared based on the primary device geometry discussed in last section. PMMA core slabs were cut in 10mm x 20mm sizes from a 3mm thick PMMA sheet using CO_2-based laser cutting machine. As discussed in chapter 5, the laser cut edges of PMMA material exhibit RMS edge roughness and average edge roughness of ≈230nm and ≈110nm respectively. These values of roughness are considered good for low amount of excitation light scattering. Therefore, PMMA core slabs were prepared by cutting them to size using CO_2 laser.

Commercially available PDMS material comes with curing agent. It is available under a number of brand names. For this study, PDMS material from Dow Corning (Sylgard 184) was used. The material base and curing agent were used in 10:1 ratio to fabricate PDMS upper and lower cladding. It is understood from the primary geometry of the device that the PDMS upper cladding incorporates a fluidic channel in it. As the molding properties of the PDMS material is very good, a fluidic channel was fabricated in PDMS by curing the material against a mold with appropriate dimensions.

6.3.1 Fabrication of novel type of acrylic molds for PDMS upper and lower cladding

PDMS has been used for making micro fluidic channels for years [1][2]. Conventionally, the molds for fabricating fluidic channels in PDMS are made by photolithography technique [3-5]. Photolithography technique is more efficient and easy to use for making micrometer sized channels. But, the fluidic channel required for TIR-based application in this study is larger in size by a factor of 300-400 times in width and height. For this big of a channel, it becomes difficult and unwieldy to use photolithography technique. Therefore, a new method of making molds using cut to size acrylic slabs was developed. Some PMMA slabs of the size of channel,

i.e. 4mm x 10mm, were laser-cut from the 0.060” thick PMMA sheet. Some other slabs of the size of core were also used. To design a mold for PDMS upper cladding with fluidic channel, a slab with dimensions 3mm x 10mm x 0.060’’ was permanently bonded with and in the center of the surface of a slab of dimensions 10mm x 20mm x 0.090”. The schematic of these slabs is shown in figure 6.3. Figure 6.3(a) shows top view of the channel sized PMMA slab. Figure 6.3(b) shows top view of the core sized PMMA slab. And figure 6.3(c) shows the top view of the mold made by bonding the two slabs together. And figure 6.3(d) shows side view of the mold shown in figure 6.3(c).

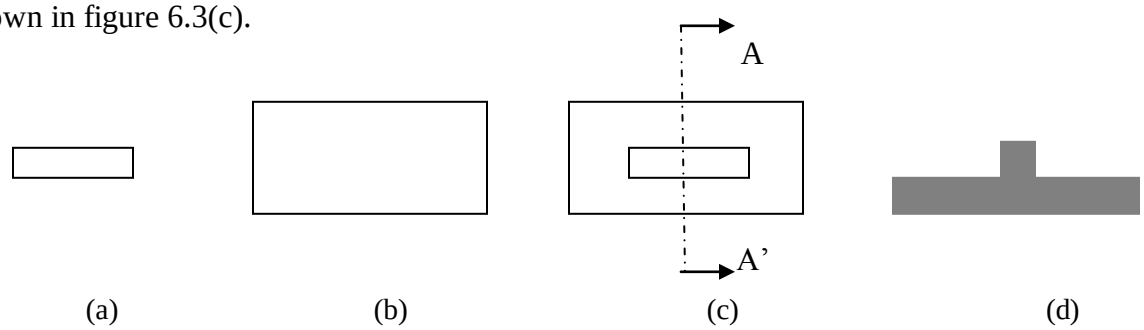

Figure 6.3, (a) top view of the channel sized PMMA slab (b) top view of the core sized PMMA slab (c) top view of the mold made by bonding the two slabs (d) side view of the mold

Two PMMA slabs were bonded together using a solvent bonding technique. A mixture of dichloromethene, dichloroethene with methyl methacrylate monomer (MMA monomer) is demonstrated to be a cement for acrylics [6][7]. Weldon is brands name of commercially available such acrylic cement. Weldon was used in proper amount to bond the slabs together to make a mold. For that, 5µl drop of Weldon cement was applied to the surface of one slab (core sized slab) and then the second slab was put on. Then both the slabs were firmly pressed for 5 minutes and then were left to cure for a day. After a day, both the slabs were firmly bonded together making a mold for PDMS upper cladding with fluidic channel.

PDMS material was molded against this mold to make PDMS upper cladding. It was done following a procedure, which is depicted in figure 6.4. First of all, the mold was placed in a

small petri dish. Figure 6.4(a) shows a cross section of the mold. It was taken along the AA' line in figure 6.3(c). Then the PDMS base was mixed with the curing agent in 10:1 ratio and air bubbles were removed from the mixture using vacuum. Then the mixture was poured on the mold as shown in the figure 6.4(b). It was kept for curing overnight and then the cured PDMS was carefully peeled off the mold, as shown in figure 6.4(c), to give the PDMS upper cladding with fluidic channel printed in it.

(a) (b) (c)

Figure 6.4, (a) cross section of the mold for PDMS upper cladding (b) molding PDMS against the mold (c) cross section of molded PDMS upper cladding with a channel printed in it
(NOTE: PMMA and PDMS)

At this point, it is important to elaborate how the light is coupled in the waveguide. As discussed in chapter 4, a fiber is used to directly couple light into the waveguide. That can be efficiently done for the light rays, which are launched off the fiber at an angle less than or equal to the acceptance angle of the waveguide. In other words, the coupling happens only for the rays for which the launching angle is less than or equal to the acceptance angle of the waveguide. All other rays are escaped off the waveguide. It is known that a fiber coupled blue LED (IF E92B 470nm, Industrial Fiber Optics) is used for excitation light source. The numerical aperture of the fiber coupled with the LED is 0.48, which is equivalent to a launching angle of 28.69°. On the other hand, the numerical aperture of the PMMA (1.49) – PDMS (1.44) waveguide is 0.38, which is equivalent to 22.5°. So, the rays launched at angles more than 22.5° are escaped and the remaining rays are coupled into the waveguide. Launching angle of equal to 22.5° gives critical

angle of 75.11°, so that the rays launched at angles less than or equal to 22.5° are incident on the core-cladding interface with angles greater than or equal to 75.11° and they are guided down the waveguide.

This is a basic explanation of light coupling in the waveguide. But, the scenario is a little different and more complicated for propagation of guided light. It is noteworthy that the portion of the waveguide, where the fluidic channel is made, PDMS is not the cladding material. Instead the fluid, which is mostly water, would be the cladding. And again for the area, where dye is deposited, the cladding would be the dye layer. So, the upper cladding material changes along the length of the waveguide core and therefore, the refractive index of the upper cladding changes discretely along the length of the core. For that reason, the critical angle is also discrete for different regions along the waveguide. To understand this with more clarity, consider the cross section of the primary device geometry along the length of the core. It is shown in figure 6.5. In the figure the core is divided in three regions numbered as 1, 2 and 3. For number 1 region of the core, the upper cladding is PDMS (1.44). For number 2 region of the core, the upper cladding is fluid (water – 1.30) and for number 3 region of the core, the upper cladding is deposited layer of dye (1.48 for FLA and 1.45 for $Ru(dpp)^3$). It is noteworthy that for all three regions the lower cladding is always PDMS. Due to the change in upper cladding refractive index along the waveguide core, the critical angle (minimum angle of incidence required to keep the light guided) for region 1 is 75.11°, for region 2 is 60.75° and for region 3 is 76.69° for $Ru(dpp)^3$ and it is 80.60° for FLA.

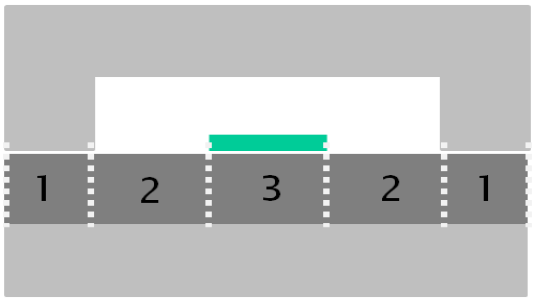

Figure 6.5, schematic of cross section of primary geometry of TIR-based device (NOTE: PMMA and PDMS)

Based on the information on critical angles, it is understood that light coupled in the region 1 remains guided in region 2. In region 3 for FLA, guided modes of light corresponding to the incidence angles ≥ 80.60° remain guided and modes corresponding to the incidence angles ≥ 75.11° and < 80.60° are scattered out of the core. In region 3 for $Ru(dpp)^3$, guided modes of light corresponding to the incidence angles ≥ 76.69° remain guided and modes corresponding to the incidence angles ≥ 75.11° and < 76.69° are scattered off the core. As the waveguide supports multimode propagation, there are still thousands of modes supported in the waveguide corresponding to incidence angles between 80.60° and 90°. And losing on some modes in region 3 of the waveguide is not a problem for exciting the dye layer. It is to be noted that it is just a 2D analysis of the waveguide.

Thus, light is coupled in the waveguide using a multimode plastic optical fiber. But, for that the fiber needs to be steady in its position while device operation. For that, a groove was made in the PDMS lower cladding to hold the fiber firmly. A socket for the waveguide core was also made in the PDMS lower cladding. The length of the channel and size of the mold for upper cladding was also modified a little to account for the socket and groove of the lower cladding, keeping the total surface area of both the molds the same. A 3D drawing of newly designed molds are shown in figure 6.6. Figure 6.6(a) shows mold design for PDMS lower cladding.

Figure 6.6(b), shows revised mold design for PDMS upper cladding. The scale used for figure 6.6 is 1 unit equals to 20mm.

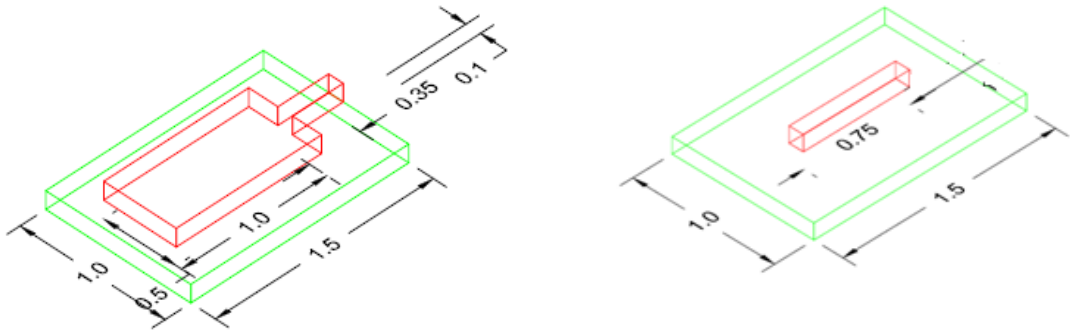

(a) (b)

Figure 6.6, (a) mold for PDMS lower cladding (b) revised mold for PDMS upper cladding

The mold for PDMS lower cladding was made by joining 3 blocks of PMMA together. The dimensions of these 3 blocks were 20mm x 30mm, 10mm x 20mm and 5mm x 2mm all cut from a 0.090" PMMA sheet. The process of making the mold is shown in figure 6.7. Figure 6.7(a) shows side view of 20mm x 30mm block. Figure 6.7(b) and figure 6.7(c) show side views of 10mm x 20mm block and 5mm x 2 mm block respectively. The blocks (b) and (c) were placed on block (a) as shown in the 3D diagram in figure 6.6(a). Then, 20µl of Weldon cement was applied to one of the edges of the interface using pipette. The cement covered the whole interface due to capillary action. After 1 day of curing time, the mold was ready to use. A side view of prepared mold is shown in figure 6.7(d).

(a) (b) (c) (d)

Figure 6.7, (a) 20mm x 30mm x 0.09” PMMA block (b) 10mm x 20mm x 0.09” PMMA block (c) 5mm x 2mm x 0.09” PMMA block (d) mold made for PDMS lower cladding

The lower cladding was made by casting PDMS against this mold. For that, the mold was put in a petri dish. Then, PDMS base and curing agent was mixed in 10:1 proportion in one beaker. Air bubbles were removed from the mixture using vacuum pump. Then, 20ml of this mixture was poured on the mold in the petri dish and the dish was kept overnight for curing at room temperature. Then the PDMS was peeled off the mold and lower cladding was cut in size of mold using razor blade. The fabrication process is explained in figure 6.8. Figure 6.8(b) shows molding of PDMS against the mold shown in figure 6.8(b). Figure 6.8(c) shows bottom view of molded PDMS lower cladding. The dashed-lines in (b) and (c) are edges of fiber groove and socket in their respective views.

Thus, the lower PDMS cladding included a grove for fiber and a socket for waveguide core. They can be seen in figure 6.8(c). It is seen that the fiber groove was in such a manner that the excitation fiber can be fit into the groove with its alignment to be normal and in the center to the 10mm edge (edge of smaller side) of the core slab.

(a) (b) (c)

Figure 6.8, (a) mold designed for PDMS lower cladding (b) molding process (c) bottom view of molded PDMS lower cladding

Thus, with the upper and lower cladding made out of PDMS, three main problems in chip fabrication are solved; designing fluidic channel in PDMS upper cladding, providing core slab cut to size, and providing fiber groove and core socket in PDMS lower cladding.

6.4 Development of technique for PDMS-PDMS and PMMA-PDMS bonding

After fabricating PDMS lower cladding, PDMS upper cladding and PMMA core, the problem was how to bond them together to make a single device. It is important to develop a technique to bond PMMA core with PDMS lower and upper claddings and it's also important to bond PDMS upper cladding to the PDMS lower cladding. This is evident in figure 6.9. Figure 6.9(a) shows bottom view of PDMS lower cladding with the groove and socket. Figure 6.9(b) is bottom view of PDMS upper cladding. Figure 6.9(c) shows top view of the final device when the both the cladding's were flipped over and upper cladding was put on the lower cladding. It is essential to bond the rest of the surface area of the PDMS upper cladding to the corresponding part of the lower cladding, where the core slab is not bonded.

As shown in figure 6.9(c), the area which is not enclosed by the small-dashed line is the area where PDMS-PDMS bonding is essential, and the area which is enclosed by the small-dashed line is the area where PMMA-PDMS bonding is essential. For that, two different types of bonding techniques were tried; wet bonding (chemical assisted bonding) and dry bonding (adhesiveless bonding).

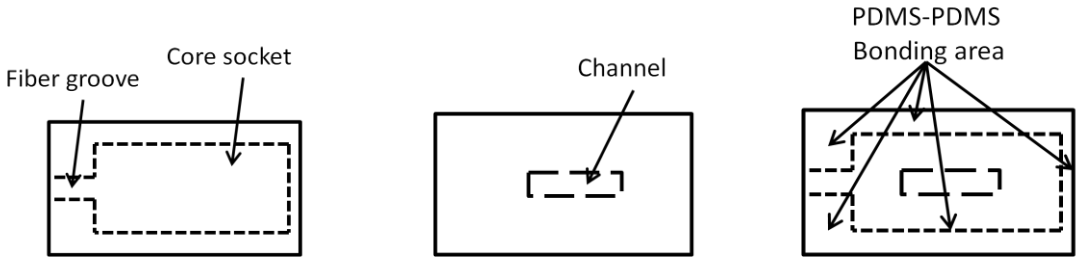

(a) (b) (c)

Figure 6.9, (a) bottom view of PDMS lower cladding (b) bottom view of PDMS upper cladding (c) top view of combined PDMS cladding

6.4.1 Wet bonding (chemical assisted bonding)

Eddings et al [8] demonstrated wet bonding technique for PDMS-PDMS bonding. They used PDMS curing agent as a bonding substance between two semi-cured PDMS slabs. The same method was tried to bond two PDMS slabs with one slab having the fluidic channel. For that, two semi-cured PDMS slabs were provided with one of them having a fluidic channel. Then, 200µl of PDMS curing agent was applied to the surface of one of the slabs and then both the slabs were put together. It was very difficult to apply the curing agent uniformly with smaller thickness on the slab surface. It was due to the super hydrophobic nature of PDMS material. After applying the curing agent, both the slabs were pressed firmly against each other and were cured for 24 hours. The two slabs were bonded firmly together with each other. But the channel was found clogged by the curing agent. So, five different pairs of slabs were tried to confirm the adequacy of the technique. For all the five pairs, the channels were clogged less or more. It was due to the same reason of super hydrophobic nature of PDMS material. It was very difficult to handle the curing agent with PDMS. Hence, the wet bonding method was proved to be unwieldy for this study due to the threat of channel clogging. Therefore, some other techniques of bonding PDMS-PDMS and PMMA-PDMS were explored for dry (adhesive less) bonding.

6.4.2 Dry (adhesive less) bonding

Dry bonding technique depends on surface modification of materials. Surface chemistry of the materials involved is modified to make them reactive enough to make covalent bonds with each other. Several bonding techniques employing surface modification are reported for PDMS-PDMS bonding as well as PDMS-PMMA bonding [9-13]. Kim et al demonstrated the use of self-assembled layer on PMMA surface for optimum bonding of PMMA with PDMS [13]. Eddings et al demonstrated surface modification of PDMS by O_2 plasma and corona discharge for optimized PDMS-PDMS bonding [8]. Kim et al used corona discharge for bonding surface

modified PMMA with PDMS. Corona discharge is nothing but air plasma discharge produced due to high potential gradient around a conductor. In this study, a high density linear extended air plasma system was used for producing corona discharge. For that, a plasmaline 415 plasma chamber was used. Unlike the electrode for corona discharge, this plasma chamber employs coaxial waveguide structures for creating linear extended air plasma; high potential gradient corona discharge.

The technique used here for PDMS-PDMS bonding is explained in figure 6.10. As shown in the figure 6.10(a), two PDMS blocks were treated by corona discharge simultaneously using 60W RF power and 0.9 Torr air pressure in the plasmaline chamber. Immediately after that, treated surface of the slabs were brought together and pressed firmly for 30s to obtain irreversible PDMS-PDMS bonding. It is shown in figure 6.10(b).

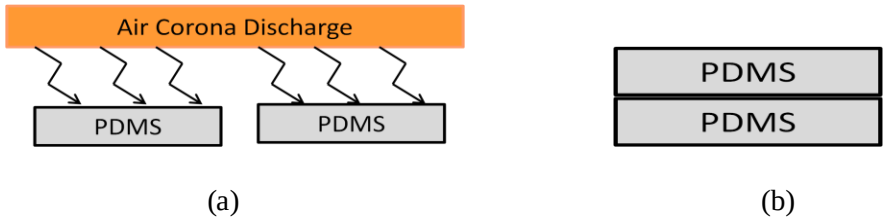

Figure 6.10, (a) corona discharge treatment of PDMS (b) irreversible PDMS-PDMS bonding

The technique used for PMMA-PDMS bonding is given in figure 6.11. As shown in figure 6.11(a), PMMA core slab was treated with O_2 plasma using micro RIE plasma chamber at 200W RF power, 50sccm O_2 flow rate and 50mTorr pressure for 60 seconds. Immediately after that, the slab was dip in activated 5% 3-APTES (3-aminopropyl triethoxysilane) solution for 1 minute (the solution was heated at 85° C for 5 minutes to activate) to create a self-assembled

layer on PMMA surface. Then, the slab was kept at 65° C for 10 minutes in order to stabilize the self-assembled layer. This process step is shown in figure 6.11(b). After that, the PMMA slab and PDMS slab, both were treated by air corona discharge using the plasmaline chamber at 60W RF power and 0.9Torr air pressure for 15 seconds. This process step is shown in figure 6.11(c). Immediately after the corona discharge, the treated surfaces of the PMMA and PDMS slabs were brought together in contact firmly under pressure for 30 seconds to obtain irreversible bonding between them. Thus, the PMMA-PDMS bonding was obtained using corona discharge technique.

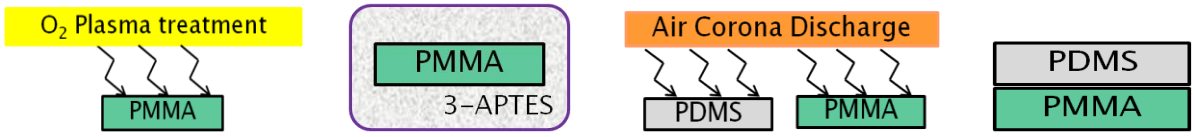

(a) (b) (c) (d)

Figure 6.11, (a) O2 plasma treatment of PMMA core slab (b) 3-APTES treatment of PMMA to create a self-assembled layer (c) corona discharge treatment of PDMS and PMMA (d) PMMA-PDMS bonding

Thus, the problem of bonding PDMS to PDMS and PMMA to PDMS was solved. These bonding techniques were implemented in TIR-based device fabrication as shown in figure 6.12 and figure 6.13. The PMMA and PDMS slabs shown in these figures are cross sectional views of their original counterparts taken along the length. Figure 6.12(a) depicts four steps by which PDMS upper cladding is fabricated with fluidic channel in it. In the first step, two PMMA slabs cut to sizes of 20mm x 30mm and 4mm x 15mm respectively are provided. In the second step, they are bonded together to make the mold for fluidic channel in PDMS upper cladding. In the third step, PDMS is cast against the mold and cured. In the final step, the cured PDMS is peeled off the mold and cut to the size of the mold using a blade. Figure 6.12(b) gives four steps by which PDMS lower cladding is fabricated with fiber groove and core socket in it. Figure 6.12(c) shows how PMMA core slab is bonded to PDMS upper cladding after dye deposition. In the first step, PMMA core slab is processed by O2 plasma. In step two, immediately after the O2 plasma

treatment the slab is treated with 3-APTES to form the self-assembled layer. In step three, a layer of dye is deposited on the surface of PMMA core using one of the standardized methods of deposition. And three holes of 1mm diameter are punched along the channel using a hollow metal pipe; one hole in the center for collecting fiber and one hole on either side for inlet and outlet of fluid. In step four, the PMMA slab and PDMS upper cladding prepared in step three are treated by corona discharge. In the final step, the treated surfaces are brought in contact and pressed firmly for 30s to obtain irreversible bond.

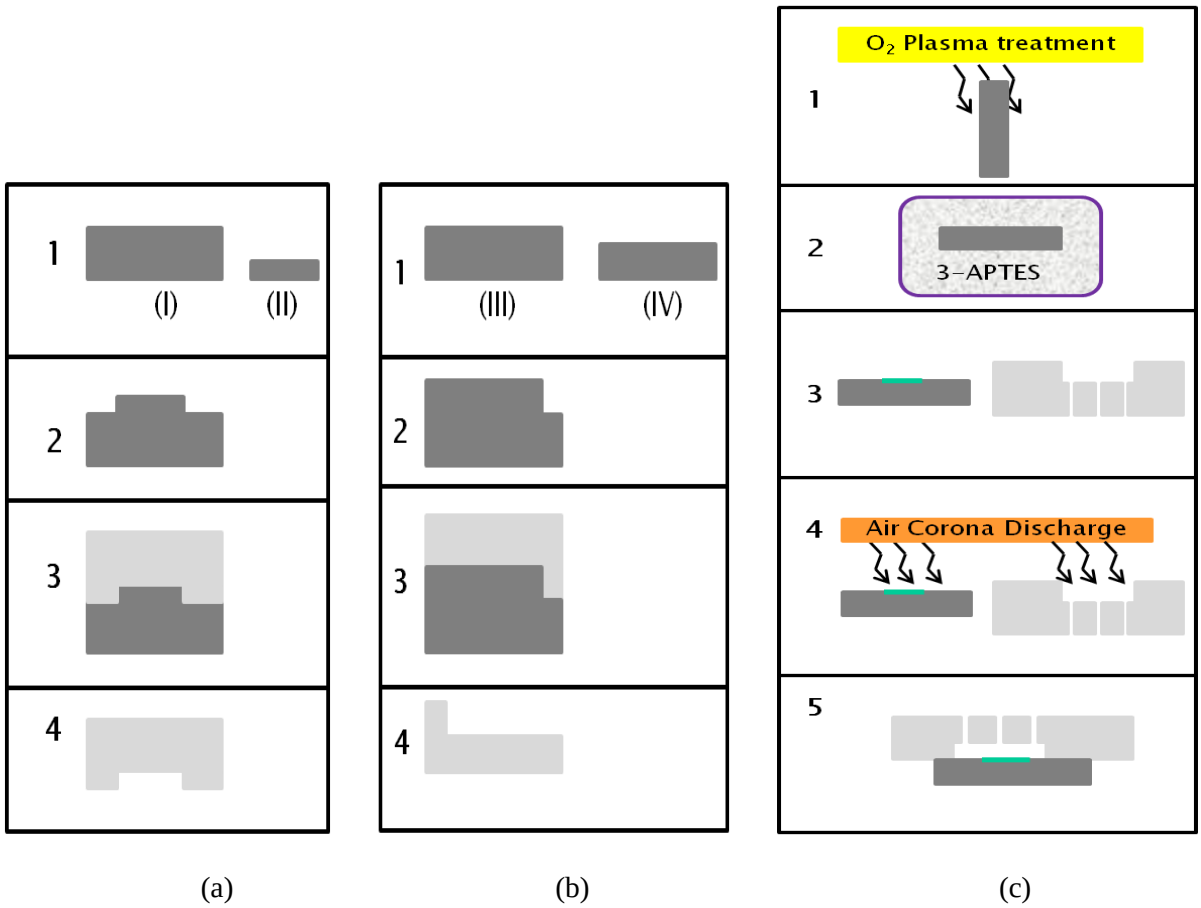

Figure 6.12, (a) process steps for PDMS upper cladding fabrication (b) process steps for PDMS lower cladding fabrication (c) process steps for bonding PMMA core to PDMS upper cladding

As shown in figure 6.13(a), the PDMS lower cladding is bonded with the PMMA core and the PDMS upper cladding using corona discharge treatment. The final device looks like as shown in figure 6.13(b). This figure is a cross sectional view taken along the length of the device through channel. The core sealed in the socket, excitation fiber groove, collecting fiber hole and inlet-outlet valves are seen in the picture of the original device in figure 6.14.

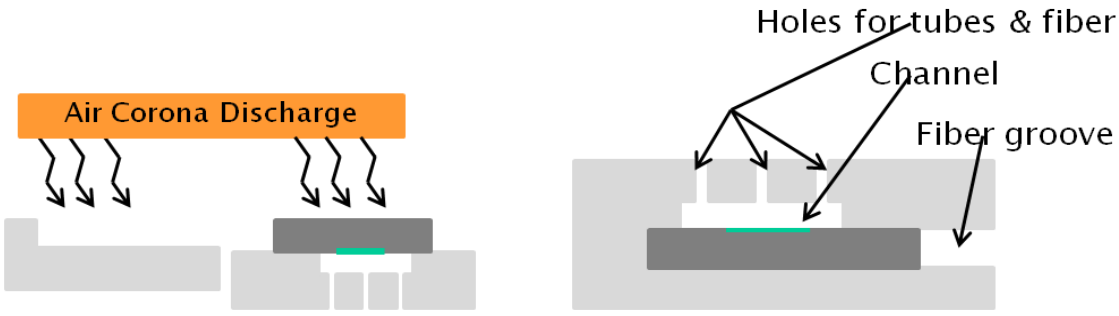

(a) (b)

Figure 6.13, (a) final process step in the device fabrication (b) cross section of the TIR-based device

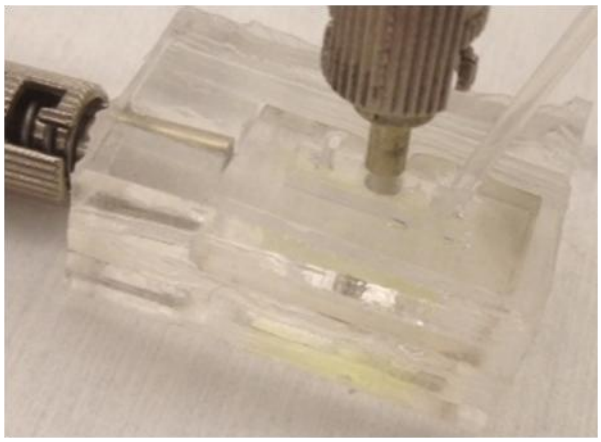

Figure 6.14, a picture of fabricated TIR-based device

6.5 Improvements made in the device design and fabrication technique

The technique employed for TIR-based device fabrication necessitates the dye layer to be deposited on the 3-APTES treated PMMA surface and it also necessitates the deposited dye layer to be exposed to corona discharge. So, it is necessary to check if the exposure to corona discharge changes the fluorescence characteristics of the deposited dye. For that, two PMMA samples were prepared based on the protocol mentioned in chapter 5. These samples were treated by 3-APTES following the procedure mentioned earlier. After that, PVA-FLA layer was deposited on one of the samples and $Ru(dpp)^3$ was deposited on the other using the optimized standard method of deposition discussed in chapter 5. Spectra were measured following the standard protocol. Then, both the samples were exposed to corona discharge and the spectra were measured again. Spectra taken before corona discharge and after corona discharge were compared and the results are shown in figure 6.15. Figure 6.15(a) shows the results of comparison for FLA-PVA deposition. And figure 6.15(b) shows the results of comparison for $Ru(dpp)^3$ deposition.

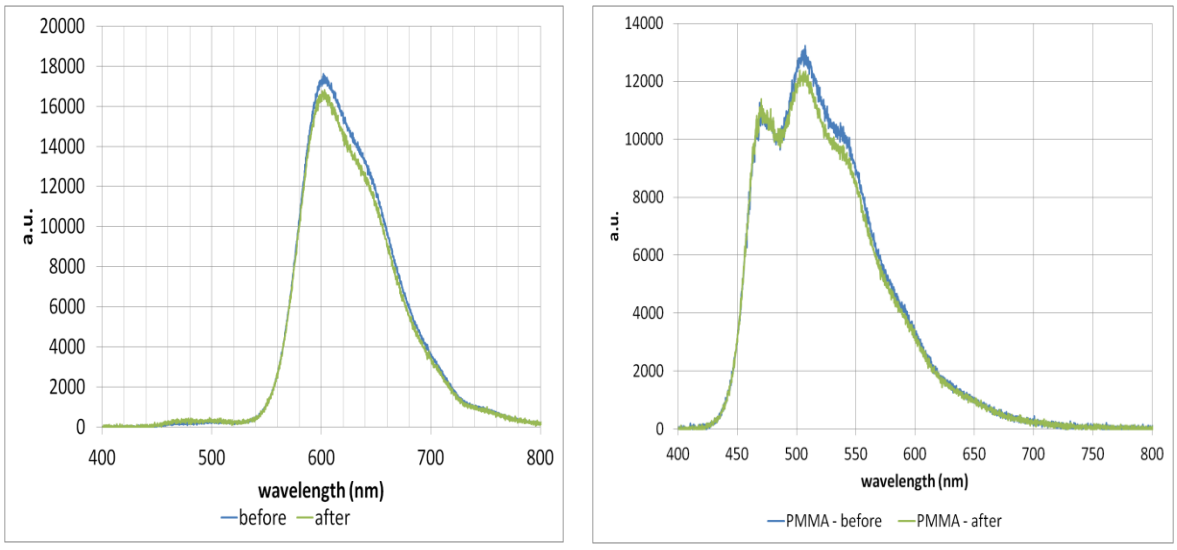

(a) (b)

Figure 6.15, (a) comparison of Ru(dpp)3 spectrum before and after corona discharge (b) comparison of FLA-PVA spectrum before and after corona discharge

The results tell that there is not any difference in the spectrum after corona discharge. Therefore, corona discharge treatment does not affect the spectral characteristics of the fluorescence of deposited dye layers.

The channels incorporated in the final device should not leak after the bonding between PDMS upper cladding and PMMA core. The adequacy of the employed fabrication technique should be tested to check the repeatability of consistently producing non-leaky channels. For that, ten different devices were made and tested. The channels of all ten devices were filled by phosphate buffered saline (pH 7.4) and then the devices were kept at room temperature at atmospheric pressure for six hours. It was observed if the channels leaked during the six hours time period. Three out of the ten channels were found leaky after six hours. This was attributed to the poor quality of PDMS-PDMS bonding and/or PDMS-PMMA bonding. This kind of poor PDMS-PDMS bonding is reported by Eddings et al [8]. It is also shown that the quality of the bonding depends on the surface area of the interface. The larger the interface area better is the bonding quality. Therefore, the dimensions of the device were increased in order to have more PDMS-PDMS and PMMA-PDMS interface area.

The change of dimensions in the new design is evident in figure 6.16. Figure 6.16(a) shows the old design. Figure 6.16(b) shows the new design called revised design-I. It is evident from the figure that increase in the overall dimension of the device increased the PDMS-PDMS and PMMA-PDMS interface area. The new design increased the total device area from 600mm^2 to 875mm^2. The new design increased the total PDMS lower cladding to PDMS upper cladding interface area from 372mm^2 to 494mm^2 and it increased the total PDMS upper cladding to PMMA core interface area from 155mm^2 to 300mm^2. Thus, the new design provided more interface area for stronger bond. The adequacy of the employed fabrication technique was tested

again to check the repeatability of consistently producing non-leaky channels using ten devices of the new design. All the ten devices were found to have non-leaky channels after eight hours. The results of the adequacy test confirmed an improvement of the new design over the old design.

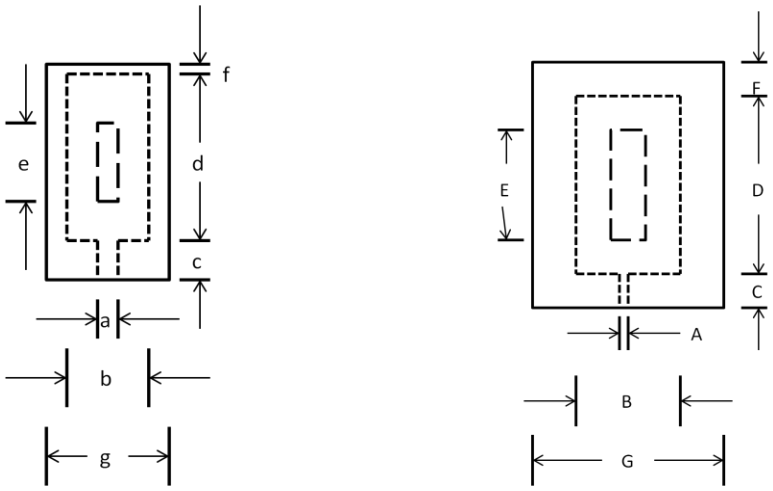

(a) (b)

Figure 6.16, (a) top view of old TIR-based design with smaller interface area (b) top view of new TIR-based design (revised design-I) with larger interface area
(NOTE : a = 3mm, b = 10mm, c = 6mm, d = 20mm, e = 15mm, f = 4mm, g = 20mm, A = 1mm, B = 15mm, C = 6mm, D = 25mm, E = 15mm, F = 4mm, G = 25mm)

The molds for the new design were made of PMMA slabs with different dimensions. The mold for PDMS upper cladding was made by bonding two PMMA slabs of dimensions 25mm x 35mm x 2.2mm and 5mm x 15mm x 2.2mm together. The mold for PDMS lower cladding was made by bonding three PMMA slabs of dimensions 25mm x 35mm x 2.2mm, 15mm x 25mm x 2.2mm and 1mm x 6mm x 2.2mm together. The slabs were bonded together using the Weldon cement as mentioned earlier.

It can be understood that the interface area of the PDMS upper cladding to PMMA core is redundant in this design. It has little influence on the adequacy of the design with respect to channel leakage. If we get rid of the redundant area of PDMS lower cladding to PDMS upper

cladding interface then TIR-based chips can be produced with the same 300mm^2 PMMA-PDMS interface area with smaller over all device area. The top view of a revised design-II is shown in figure 6.17(a).

As shown in the figure, the revised design-II has got rid of the redundant PDMS-PDMS interface area. The total device area has decreased from 875mm^2 to 465mm^2 with a decrease in PDMS-PDMS interface area from 494mm^2 to 84mm^2. And the interface area of PMMA to PDMS upper cladding is the same as 300mm^2. The molds for the revised design-II were made of PMMA slabs with different dimensions. The mold for PDMS upper cladding was made by bonding two PMMA slabs of dimensions 15mm x 31mm x 2.2mm and 5mm x 15mm x 2.2mm together. The mold for PDMS lower cladding was made by bonding three PMMA slabs of dimensions 15mm x 31mm x 2.2mm, 15mm x 25mm x 2.2mm and 1mm x 6mm x 2.2mm together. The slabs were bonded together using the Weldon cement as mentioned earlier.

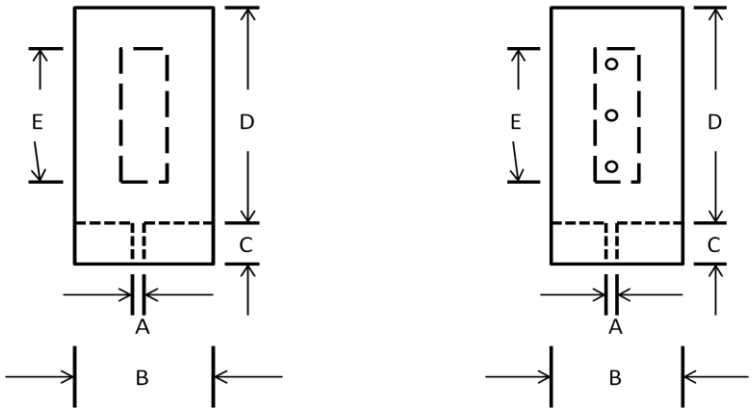

(a) (b)

Figure 6.17, (a) revised design-II with smaller over all device area (b) revised design-II with inlet, outlet and collecting fiber holes (NOTE: A=1mm, B=15mm, C=6mm, D=25mm, E=15mm)

Now, consider the figure 6.17(b). Three holes in this figure are the inlet, outlet and collecting fiber holes. As mentioned earlier, these are 1mm diameter holes. This 1mm diameter

inlet is too small for the 5mm wide and 0.09" (2.2mm) high channel. And with such a small inlet, replenishing of the channel with new fluid leaves certain dead zones in the channel volume. These dead zones are detrimental for the device performance. For that, the dimensions of the channel at the inlet should be less than or equal to the inlet-hole dimensions to get rid of these dead zones while replenishing the channel. For that, a revised design-III with tapered channel instead of rectangular channel was made. The design-III is shown in figure 6.18(a). The channel is made by combining two triangular PMMA blocks laser-cut to size from a 0.09" (2.2mm) thick PMMA sheet. The dimensions of one such block is shown in figure 6.18(b). So, the mold for PDMS upper cladding for this design was made by bonding two such triangles to a 15mm x 31mm x 2.2mm sized PMMA block. And the mold for PDMS lower cladding of this design was made by bonding three PMMA blocks of dimensions 15mm x 25mm x 2.2mm, 15mm x 31mm x 2.2mm and 1mm x 6mm x 2.2mm together.

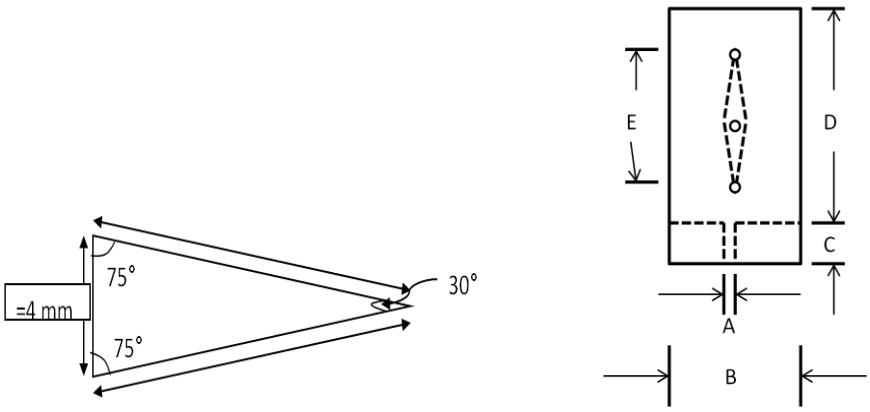

(a) (b)

Figure 6.18, (a) dimensions of a triangle used as a building block of the mold for a tapered channel in PDMS upper cladding (cut to size by CO_2 laser) (b) top view of the revised design-III with tapered channel

The tapered channel design gave 340mm^2 PMMA-PDMS interface area, which is larger than the area provided by the revised design-II for the same total device area of 875mm2. The

new chip designs with larger interface areas (revised design-I and revised design-II) and the tapered channel design of the TIR-based chip were implemented quite later during the progress of this thesis work. The tapered channel design was used to characterize device performance parameters of the pH-sensor, the H_2O_2 sensor and the lactose sensor implemented using the enzymatic biosensor concept. Before that, primary implementation of pH-sensor concept using fluorescenamine dye was demonstrated using the old design shown in figure 6.16(a). The primary implementation of pH-sensor, improvements in its design and implementation and characterization of its performance parameters are discussed in chapter 7 of this thesis work. Similarly, primary implementations of H_2O_2-sensor and lactose sensor using $Ru(dpp)^3$ were demonstrated using the revised design-I and revised design-II. The primary implementation of the H_2O_2 sensor and the lactose sensor, improvements in their designs and implementations and characterization of their performance parameters are discussed in chapter 8 of this thesis work.

References

[1] Mcdonald J.C.; Whitesides G.M. “Poly(dimethylsiloxane) as a Material for Fabricating Microfluidic Devices”. ACCOUNTS OF CHEMICAL RESEARCH /VOL. 35, NO. 7, 2002

[2] Duffy, D.C.; McDonald J.C.; Schueller O.J.A.; Whitesides, G.M. “Rapid Prototyping of Microfluidic Systems in Poly(dimethylsiloxane)”. Anal. Chem. 1998, 70, 4974-4984

[3] Anderson, J. R.; Chiu, D. T.; Jackman, R. J.; Chemiavskaya, O.; McDonald, J. C.; Wu, H.; Whitesides, S. H.; Whitesides, G. M. “Fabrication of Topologically Complex Three-Dimensional Microfluidic Systems in PDMS by Rapid Prototyping.” Anal. Chem. **2000**, 72, 3158-3164.

[4] Jo, B.-H.; Van Lerberghe, L. M.; Motsegood, K. M.; Beebe, D. J. “Three- Dimensional Micro-Channel Fabrication in Polydimethylsiloxane (PDMS) elastomer.” J.microelectromech. Syst. **2000**, 9, 76-81.

[5] Qin, D.; Xia, Y.; Whitesides, G. M. “Rapid Prototyping of Complex Structures with Feature Sizes Larger Than 20 pm” Adv. Mater. 1996, 8, 917.

[6] US7592385 patent

[7] US20060252865

[8] Eddings, M. A.; Johnson, M. A.; Gale B. K. “Determining the optimal PDMS–PDMS bonding technique for microfluidic devices”. J. Micromech. Microeng. 18 (2008) 067001

[9] Unger, M.A.; Chou, H.P.; Thorsen, T.; Scherer A.; Quake S.R. “Monolithic Microfabricated Valves and Pumps by Multilayer Soft Lithography” SCIENCE VOL 288 7 APRIL 2000

[10] Satyanarayana, S; Karnik, R. N.; Majumdar, A. “Stamp-and-stick room-temperature bonding technique for microdevices” J. Microelectromech. Syst. 14 392–9 2005

[11] Samel, B.; Chowdhury, M K; Stemme, G “The fabrication of microfluidic structures by means of full-wafer adhesive bonding using a poly(dimethylsiloxane) catalyst” J. Micromech. Microeng. **17** 1710–4 2007

[12] Go, J. S.; Shoji, S. “A disposable, dead volume-free and leak-free in-plane PDMS microvalve” Sensors Actuators A 114 438–44 2004

[13] Kim, K.; Park, S.W.; Yang, S.S. “The optimization of PDMS-PMMA bonding process using silane primer” BioChip J. 4(2): 148 – 154 2010

Chapter 7: Development and testing of the TIR-based device as a pH-sensor

7.1 Introduction

The TIR-based chip discussed in chapter 6 can be developed into a pH-sensor by depositing a pH-sensitive dye layer on PMMA core surface. As discussed earlier, fluorescenamine is a pH sensitive dye. And different deposition methods for a pH-sensitive dye fluorescenamine are discussed in chapter 5. The deposition method that uses polyvinyl alcohol as a substrate is proved to be the best method of all which are tried and tested for adequacy. But, as discussed in chapter 5, the dye layers deposited using this method lift off the surface sometimes. So, a couple of other methods of deposition were tried and tested, one using Si-adhesive gel and the other using HydroThane (polyurethane elastomer). These new deposition methods and their test results are discussed in section 7.2. For both methods, experiments were done to investigate how the amount (concentration) of dye used for dye deposition affect the fluorescence of deposited layers. The results of the experiments are discussed in Section 7.3. In section 7.4, the procedure of developing pH-sensors using these two deposition techniques and their operating principles are discussed. Moreover, some primary experiments to demonstrate the working of the sensors as a proof of concept were carried out. The experimental setup and procedure for these experiments are discussed in section 7.4. The results of the experiments are discussed in section 7.6.

7.2 Two more deposition methods for fluorescenamine

7.2.1 Use of Si clear adhesive gel (Devcon)

A deposition method for Ru(dpp) using Si clear adhesive gel is discussed in chapter 5. In this section, use of the same method for fluorescenamine deposition is given. For that, some PMMA slabs of 10mm x 20mm dimensions were prepared by laser cutting them from 0.09” (2.2mm) thick PMMA sheet. A deposition conjugate was made by mixing solution-A and

solution-B in 1:2 proportions. Solution-A was 1% (w/v) solution of fluoresceinamine (201626 ALDRICH) in acetone and solution-B was 20% (w/v) solution of Si-adhesive gel (Devcon) in chloroform. Deposition samples were made by depositing 5 µl of the deposition conjugate on five PMMA slabs. These PMMA samples were tested for adequacy following the standard protocol using the standard criteria as discussed in chapter 5. The spectra were measured for all the samples using the standard protocol. The spectrum for one such sample is given in figure 7.1.

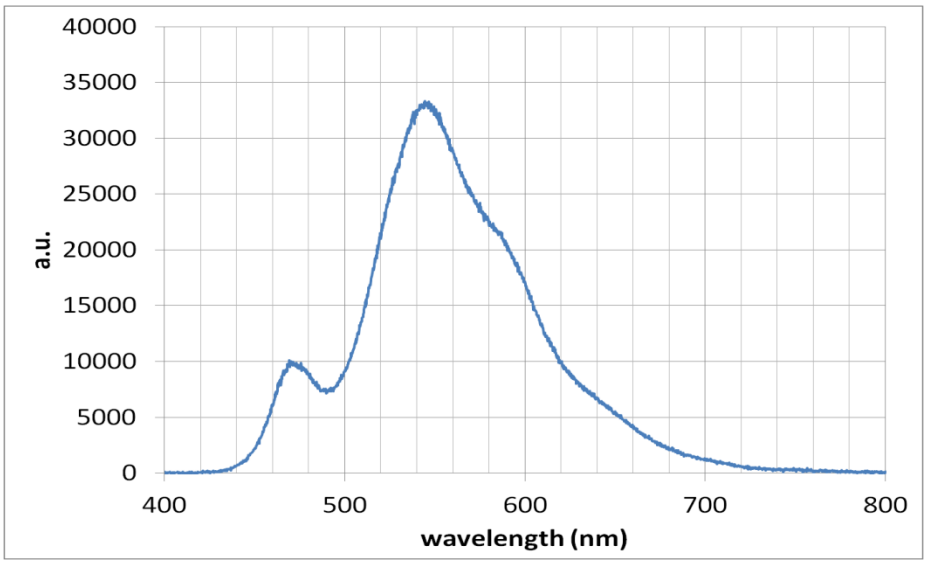

Figure 7.1, spectrum of Si clear adhesive gel based fluorescenamine deposition

In figure 7.1, the 470nm peak is of the scattered excitation light and the 520nm peak is the fluorescence peak. No other peak related to the auto-fluorescence of the substrate Si-gel is observed in the spectrum. Moreover, all five samples were treated by DI water by keeping the samples sunk in a beaker of water to check for possible lifting off of the deposited layers. After 3 hours of water treatment, the deposition layers on all five samples were found intact and firmly immobilized. Also, scattered excitation light intensity to fluorescence ratio is 0.28 without filtering which shows significant reduction in scattered excitation light. So, based on these

results, the deposition method for fluoresceinamine using Si clear adhesive gel was considered adequate for TIR-based application.

7.2.2 Use of HydroThane as a substrate for fluorescenamine deposition

One more deposition method using HydroThane (hydrophilic thermoplastic polyurethane elastomer, AdvanSource Biomaterials) was investigated. The HydroThane material was bought in the form of pellets with 15% porous structure from AdvanSource Biomaterials. A deposition conjugate was made by mixing solution-A and solution-B in 1:1 proportions. Solution-A was 2% (w/v) solution of fluoresceinamine (201626 ALDRICH) in acetone and solution-B was 10% (w/v) solution of hydrothane in toluene. Deposition samples were made by depositing 5 μl of the deposition solution on five PMMA slabs. These PMMA samples were tested for adequacy following the standard protocol using the standard criteria as discussed in chapter 5. The spectra were measured for all the samples using the standard protocol. The spectrum for one such sample is given in figure 7.2. In figure 7.2, the 470nm peak is of the scattered excitation light and the 520nm peak is the fluorescence peak. No other peak related to the auto-fluorescence of the substrate hydrothane is observed in the spectrum.

Moreover, all five samples were water treated by keeping the samples sunk in a flask of DI water to check for possible lifting off of the deposited layers. After 3 hours of water treatment, the deposition layers on all five samples were found intact and firmly immobilized. During the treatment, the fluorescenamine dye was found to leach out from the deposited layer in small amount. But, it did not affect the fluorescence characteristics of the samples. Also, scattered excitation light intensity to fluorescence ratio is 0.04 without filtering which shows significant reduction in scattered excitation light. So, based on these results, the deposition

method for fluoresceinamine using Si clear adhesive gel was considered adequate for TIR-based application.

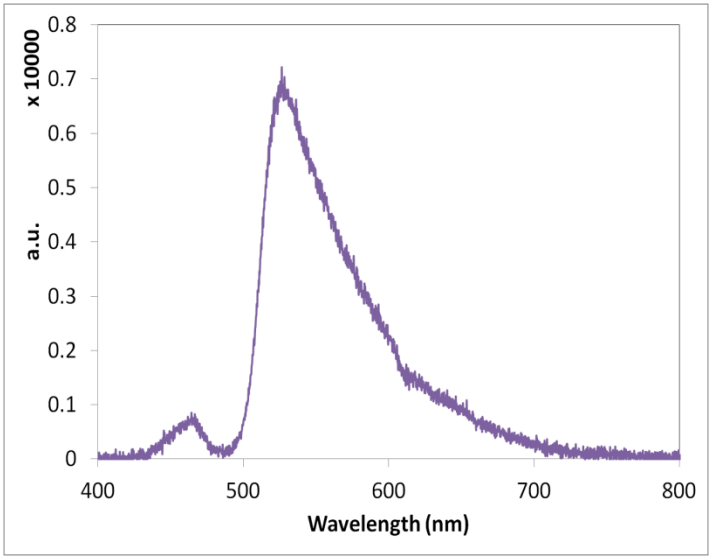

Figure 7.2, spectrum of hydrothane based fluorescenamine deposition

7.3 Effect of concentration of dye on fluorescence emission

Results of the experiments done to investigate how the concentration of dye used for dye deposition affect the fluorescence emission of deposited layers are discussed in this section for both Si-based and hydrothane based deposition methods. Amount or concentration of dye was changed by changing the % (w/v) concentration of solution-A in the deposition conjugate for both the methods.

For the hydrothane based deposition technique solution-A was prepared in five different concentrations of 0.5% (w/v), 1.0% (w/v), 1.5% (w/v), 2.0% (w/v) and 2.5% (w/v) of fluorescenamine in acetone. Five different deposition conjugates were made by mixing these solutions with 2% (w/v) solution-B of hydrothane in toluene. Then, 3µl of one of the deposition conjugates was deposited on the core surface of one TIR-based device with tapered channel through the collection fiber hole and vice versa. Thus, five such devices were made with each

one having a different concentration of dye in the deposited layer. Then, spectra of deposited layers for all five devices were measured using a fluorescence spectrometer (USB4000-FL, OceanOptics). For each spectrum, an absolute intensity of scattered excitation light (I_s) was calculated by integrating the spectrum over 400nm-490nm and an absolute intensity of fluorescence emission (I_f) was calculated by integrating the spectrum over 490nm-700nm. Scattered excitation intensity to fluorescence emission intensity ratio was calculated for each device.

This procedure was repeated for the Si-based deposition method as well, but for solution-A concentrations of 0.5% (w/v), 1.0% (w/v), 1.5% (w/v) and 2.0% (w/v). And the conjugates were made by mixing solution-A and solution-B in 1:1 proportions for this experiment.

Figure 7.3(a) shows spectra taken for hydrothane based devices for all five solution-A concentrations. Figure 7.3(b) plots absolute scatter to absolute fluorescence emission ratio versus corresponding solution-A concentrations. The absolute excitation scatter intensity and the absolute fluorescence emission intensity plotted versus respective solution-A concentrations are given in figure 7.3(c) and figure 7.3(d).

It is evident that the I_s/I_f ratio decreases with increase in dye concentration, and absolute scatter intensity and absolute fluorescence emission also decreases with increase in dye concentration. As shown in figure 2.1 (in chapter 2), absorption and emission spectra for fluorescein coincide at around 500nm. Also, absorption of the excitation light increases with increase in the concentration of dye. Therefore, the absolute scatter intensity decreases with increase in dye concentration. For 2.0% concentration, the absolute intensity of the scattered excitation light captured by the collection fiber reaches its minimum possible value so at 2.5%

concentration it does not decrease further but the fluorescence emission decreases increasing the I_s/I_f ratio.

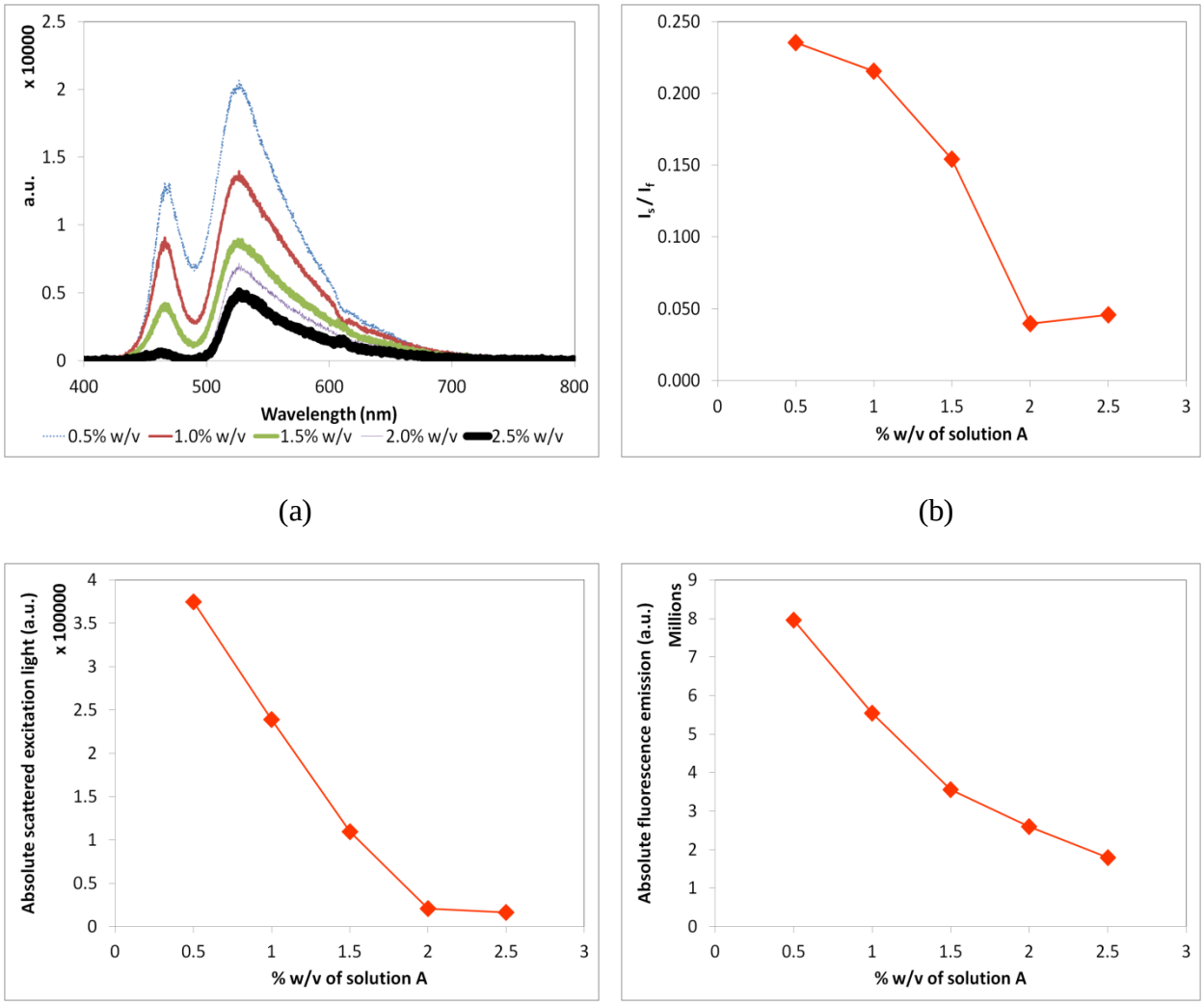

Figure 7.3, effect of fluoresceinamine concentration on fluorescence emission of deposited layers (using hydrothane based deposition, for pH 7.4) (a) spectra of deposited layers (b) absolute intensity of scattered excitation to absolute intensity of fluorescence emission ratio for different dye concentrations (c) absolute scattered excitation light for different dye concentrations (d) absolute fluorescence emission for different dye concentrations

Figure 7.4 shows similar plots for Si-adhesive based deposition for all four solution-A concentrations.

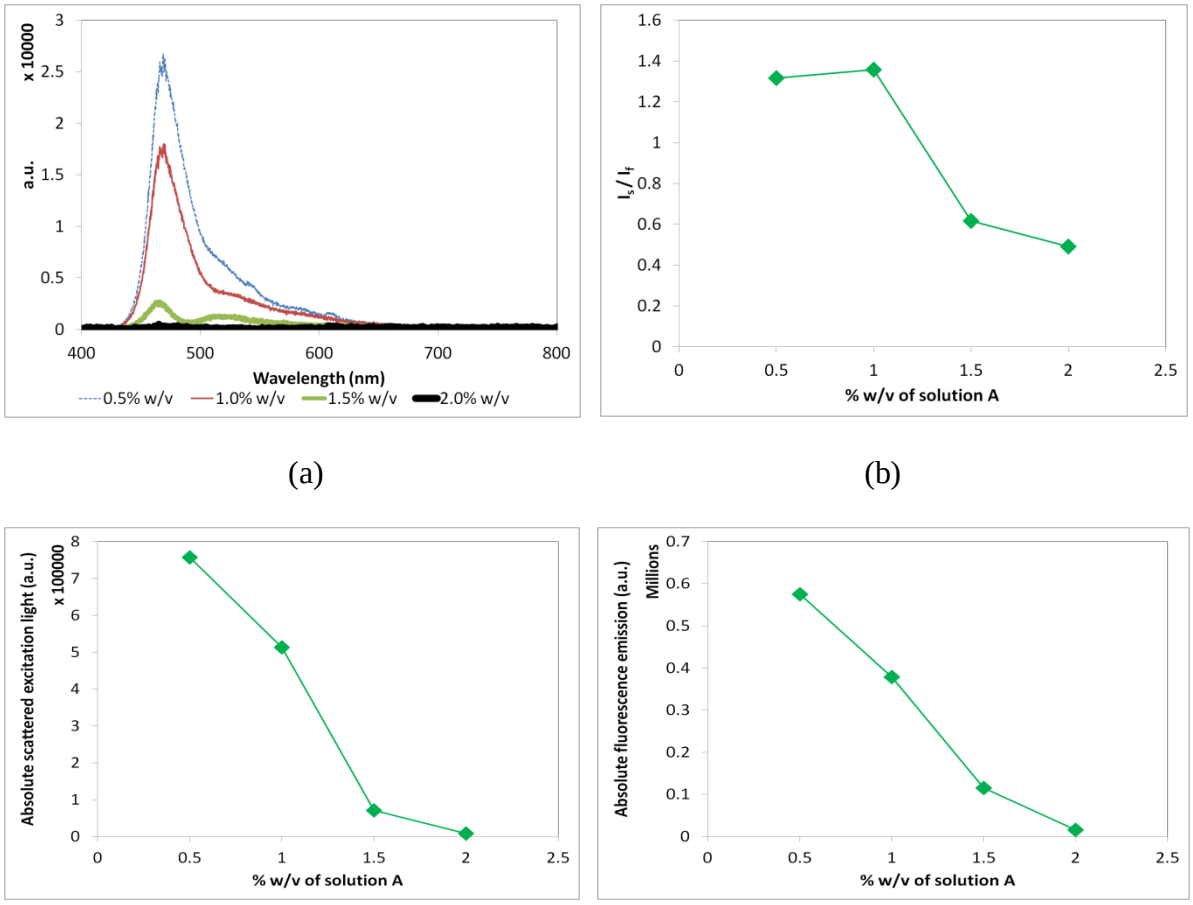

Figure 7.4, effect of fluoresceinamine concentration on fluorescence emission of deposited layers (using Si-gel based deposition, for pH 7.4) (a) spectra of deposited layers (b) absolute intensity of scattered excitation to absolute intensity of fluorescence emission ratio for different dye concentrations (c) absolute scattered excitation light for different dye concentrations (d) absolute fluorescence emission for different dye concentrations

The Si-based deposition gives the results similar to that of the hydrothane based deposition. For both deposition methods the absolute fluorescence decreases with increase in concentration, which is due to the increase in non-radiative fluoresceinamine-to-fluoresceinamine transfer. The distance between two fluoresceinamine groups decreases with increase in concentration increasing the nonradiative energy transfer. But, the absolute intensity of fluorescence emission for the Si-based deposition is observed to be lower than that for the hydrothane based deposition. The reason for that can be explained based on how the dye

molecules are embedded in deposited layers. Figure 7.5 shows how the dye embedding scheme of Si-gel employs more re-absorption of fluorescence emission compared to that of hydrothane. Figure 7.5 (a) shows hydrathane based dye layer deposited on a core surface for relatively low dye concentration, wherein a schematic of a porous structure of hydrothane is shown. Dye molecules are usually embedded in the pores of the hydrothane structure as shown. At very low concentration of dye molecules, the pores are partially filled with some pores left unfilled as shown. The filled pores situated near one another contribute to the non-radiative energy transfer. The fluorescence which is uninterrupted reached the surface and gets emitted. As shown in figure 7.5 (c), at relatively high concentration almost all the pores with close proximity are filled with dye and there is very less amount of uninterrupted fluorescence that reach the surface and get emitted.

On the contrary, the Si-based deposition embeds dye molecules by sticking them to the adhesive substrate. As shown in figure 7.5 (b) and figure 7.5 (d), more dye molecules are stuck on the top surface and at the core interface of the layers than in the bulk adhesive substrate. The dye molecules stuck in the layer are situated very closely to one another causing greater amount of non-radiative energy transfer. In this scenario, most of the fluorescence gets quenched resulting in a very weak emission of fluorescence at the surface, for relatively high concentration (figure 7.5 (d)). The I_s/I_f ratio as low as observed for hydrothane based deposition is not observed for Si-based deposition, as evident from figure 7.4(b). It is due to the large amount of scattering at the interface.

However, the amount of dye stuck on the surface and at the interface can be reduced by properly choosing the proportions of solution-A and solution-Bin the deposition conjugate. The results shown in figure 7.4 are observed for 1:1 proportion of solution-A and solution-B. In

attempt to increase the I_s/I_f ratio, a 1.5% (w/v) solution of fluoresceinamine (solution-A) was mixed with 20% (w/v) solution of Si-gel in 1:2 proportions to make a deposition conjugate.

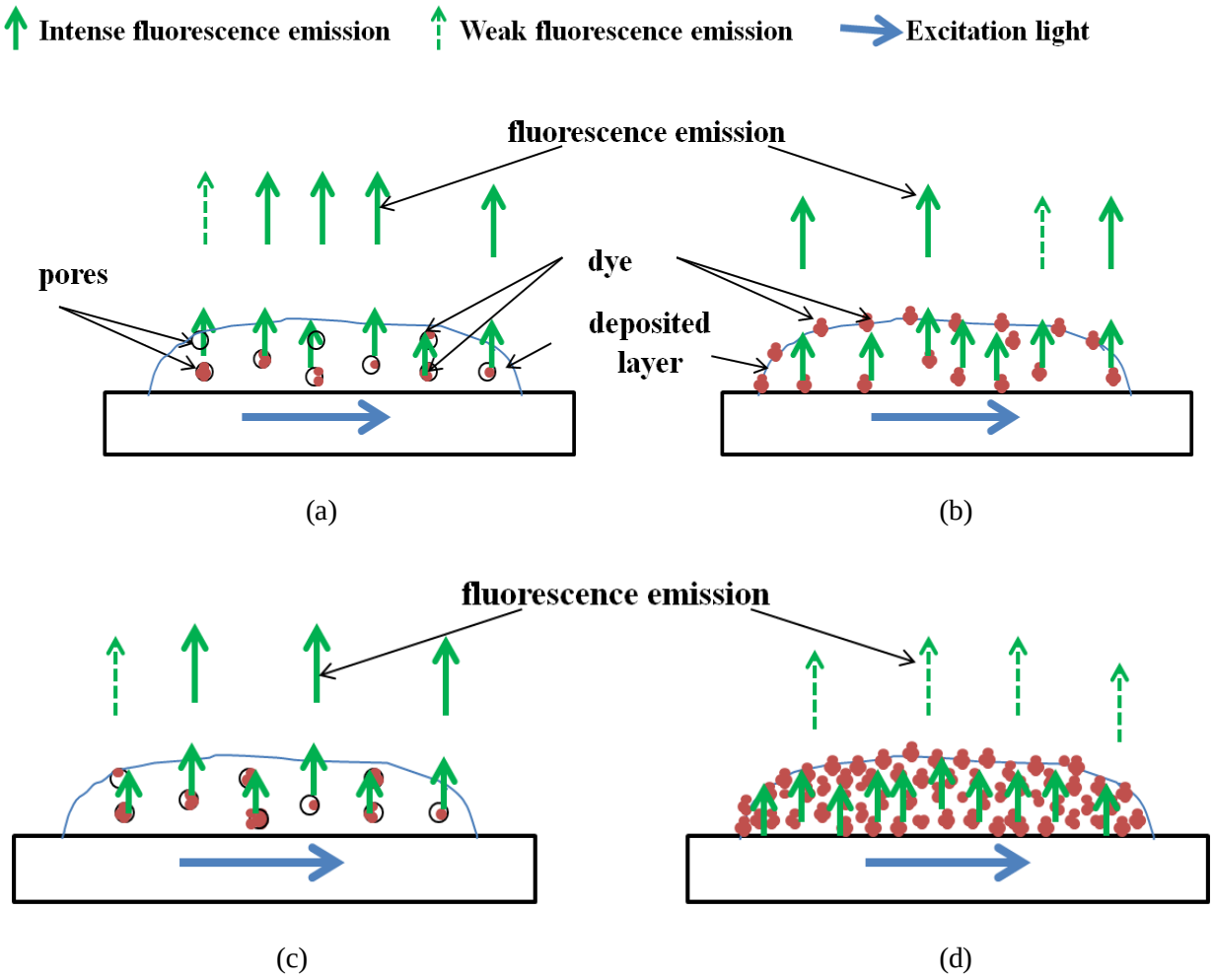

Figure 7.5, (a) schematic of hydrothane deposited dye layer for relatively small concentration (b) schematic of Si-gel deposited dye layer for relatively small concentration (a) schematic of hydrothane deposited dye layer for relatively large concentration (a) schematic of Si-gel deposited dye layer for relatively small concentration

Then, 3µl of the deposition conjugate was deposited and the resultant layer's spectrum was measured. Two identical layers were measured for their spectra and the results are given in

figure 7.6. The 1:2 proportion of solution-A and solution-B improved the I_s/I_f ratio by a factor of 3, as shown in figure 7.6, which is a significant improvement over the 1:1 deposition technique.

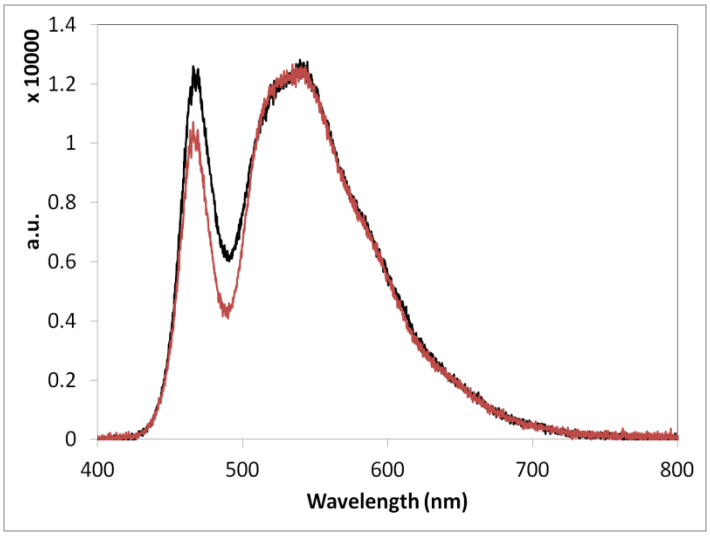

Figure 7.6, Spectra of Si-gel deposited dye layers for 1:2 proportion of solution-A and solution-B

7.4 Development of a pH-sensor using the TIR-based device

Two different pH-sensors were made with each sensor made using a different method of dye deposition. Type-I pH-sensor was made by depositing 3µl of type-I deposition conjugate and vice versa. Type-I deposition conjugate was made by mixing 2% (w/v) solution of fluoresceinamine (201626 ALDRICH) in acetone (solution-A) and 10% (w/v) solution of hydrothane in toluene (solution-B). Type-II deposition solution was made by mixing 1% (w/v) solution of fluoresceinamine (201626 ALDRICH) in acetone (solution-A) and 20% (w/v) solution of Si-adhesive gel (Devcon) in chloroform (solution-B). The sensors were made using the revised design-III (with tapered channel) of TIR-based device discussed in chapter 6.

Operating principle

A pH-sensor works on the principle of quenching of fluorescence of fluorescenamine in the presence of protons (H^+). The amount of quenching of the fluorescence is linearly proportional to the proton (H^+) concentration for moderate values of proton

concentrations. So, the value of proton concentration in the substrate solution and hence the pH value of the substrate solution can be measured by measuring the fluorescence and then by computing the corresponding value of proton concentration from the measured value of fluorescence using the calibration curve. Calibration curve is a graph of measured fluorescence intensity versus corresponding H^+ concentrations. At relatively high values of H^+ concentration, the calibration becomes non-linear. These could be due to couple of reasons. First, all the dye molecules are fully quenched so that there is no more quenching with increase in H^+ concentration. Second, the increase in H^+ concentration does not significantly increase the number of protons diffusing into the deposited layer, diffusion saturation. Also, at very low H^+ concentrations as well, the calibration curve becomes non linear and it is due to non ideal stern-volmer characteristics [1]. The linear part of the calibration curve is of more interest. It is used to determine some characteristic parameters of the sensor device like sensitivity, linear range, and limit of detection (LoD).

7.5 Primary demonstration of pH-sensor devices: experimental setup and procedure

Fluorescence response of the pH sensors was measured for different pH-buffer solutions to check their working as a proof of concept. For a right behavior, the devices should exhibit change in fluorescence intensity with change in H^+ concentration; i.e. change in pH value. For that, buffer solutions with different values of pH were run through the fluidic channels of all three devices. For each pH-buffer solution the fluorescence intensity of the deposited layer was measured using fluorescence spectrometer. All the fluorescence intensity values for each such device were plotted versus their corresponding pH values. The plots obtained like this were different than calibration curves in the sense that these plots might not include both the end point pH values of the linear range. It is because the aim of obtaining this plot is just to check if the

sensor behaves properly according to the working principle and not to find out important characteristic parameters of the sensor.

The buffer solutions with different pH values were made using phosphate buffered saline (PBS) solution with pH 7.4. First of all, one liter of PBS solution was made by dissolving a PBS buffer tablet in one liter of DI water contained in a beaker. Then, 20ml of 1 liter solution was taken and kept in a separate vial. After that, by adding proper amount of hydrochloric acid or/and sodium hydroxide in the PBS-containing beaker the pH value of the PBS buffer solution was changed step by step to be 7.7, 6.16, 5.35, 4.20 and 3.15 respectively in this order. For that, HCl and/or NaOH were added in small drops while monitoring the pH of the buffer solution using a pH probe, which was permanently placed in the beaker. HCl was added to decrease the pH value and NaOH was added to increase the pH value. Each time when a particular desired value of pH was obtained for the solution in the beaker, 20ml of the solution was taken and kept in separate vial. Thus, buffered solutions of pH values 3.15, 4.20, 5.35, 6.16, 7.40 and 7.70 were made and provided in separate 20ml vials.

Then, the experimental apparatus was setup for each pH-sensor as shown in figure 7.7. The TIRF chip was attached to the table top using a double sided transparent tape. It was excited using an end-fire fiber coupled 470nm LED. The firing end of the fiber was fit in the fiber groove of the chip. The LED was driven by 30mA current through a current supply. A plastic optical fiber was set in the collecting fiber hole to collect the fluorescence of the dye layer. The other end of the collecting fiber was connected to a fluorescence spectrometer (USB4000 FL, ocean optics). The spectrometer was set to record the fluorescence intensity trace with one sample point every second. Each sample point was an integrated value of fluorescence intensity over the spectral range of 490nm – 700nm. An inlet tube and a syringe were used to run

pH buffer solutions through the fluidic channel, as shown in the figure. For each pH buffer solution the spectrometer was made to record the trace for 60s recording 60 sample points for every pH value. The fluorescence intensity for each pH buffer solution was reckoned as an average of these 60 sample points. All the buffer solutions were reckoned one by one starting from the maximum pH value, i.e., pH 7.7.

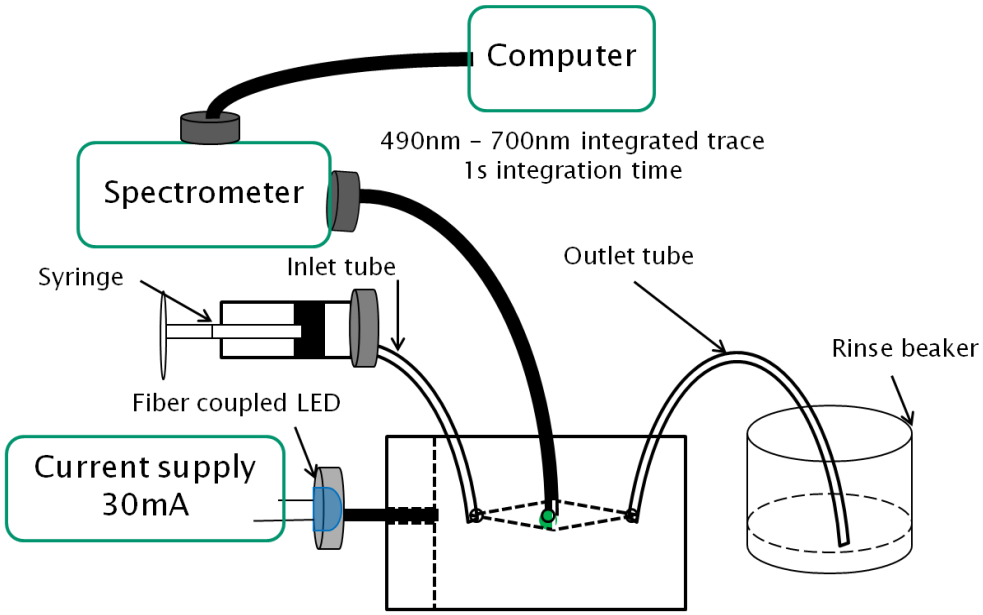

Figure 7.7, apparatus setup for experiments to measure sensor performance parameters

The spectrometer was made to record the trace continuously throughout the experiment for all pH buffer solutions. The syringe was disconnected from the inlet tube after the fluorescence intensity trace was recorded for each pH buffer solution, and then it was reloaded with a different pH buffer solution. Then, the syringe was reconnected to the inlet tube to push the new pH buffer solution through the channel until the old pH solution was completely forced out of the channel. The old pH solution got forced out of the channel through the outlet tube into the rinse beaker. After the pH buffer solution was changed each time, enough time was given for the spectrometer trace to settle down at a new fluorescence intensity level for the new pH buffer

solution. This time was recorded in seconds whenever a new pH buffer solution was measured. This time was the response time of the pH-sensor. At each new level of fluorescence intensity the trace was recorded for 60 sample points.

7.6 Primary demonstration of pH-sensor devices: experimental results

For both devices (type – I, II), the normalized intensity values of fluorescence were plotted versus their corresponding pH values. The fluorescence intensity at pH 7.7 (I_o) was decided as a factor for normalization. This I_o was then divided by the fluorescence intensity for each pH value (I) to obtain normalized intensity of fluorescence (I_o/I). Also, a plot of absolute intensity versus time was also produced for each device.

The plot of normalized intensity versus corresponding pH values for type-I pH-sensor device is given in figure 7.8 (a). Figure 7.8 (b) is a plot of absolute intensity versus time. The intensity points I_o and I_x were reckoned as averages of their corresponding 60 sample points recorded by the spectrometer. Each normalized intensity point was calculated by dividing I_o with the corresponding absolute point. There is not any significant change in fluorescence intensity between pH 3.15 and pH 4.20. And the intensity changes about 75% from pH 7.7 to pH 4.20. The plot is seen to be linear for the range of pH between 4.20 and 6.16. In figure 7.8 (b), the fluorescence intensity is found to change with the change in pH, which proves the concept. The response time is found to be about 3s.

The hydrothane based deposition method was used for the type-II pH-sensor device. The plot of normalized intensity versus corresponding pH values for type-II pH-sensor device is given in figure 7.9 (a). 7.9 (b) is a plot of absolute intensity versus time.

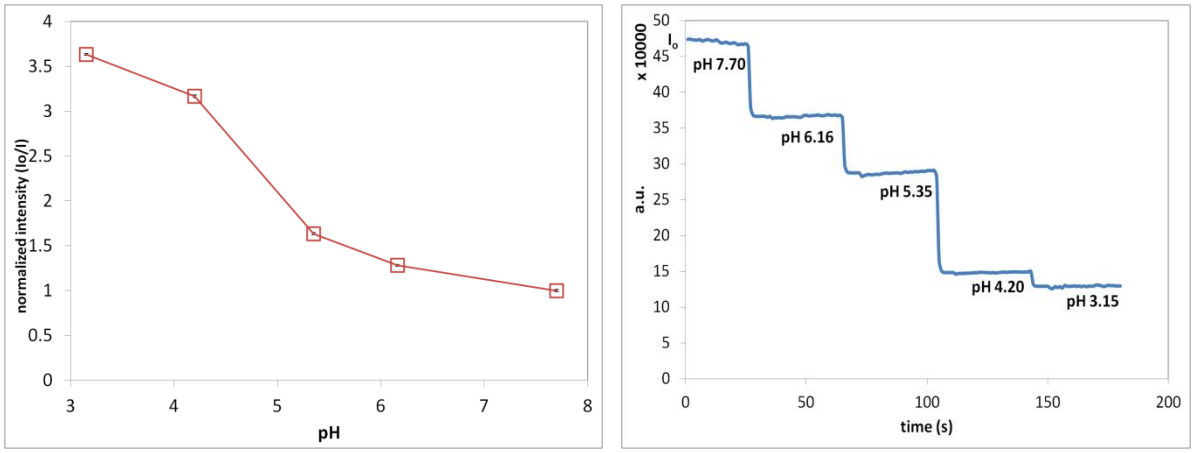

(a) (b)

Figure 7.8, (a) normalized intensity versus corresponding pH values for type-I pH-sensor (Si-gel) (b) plot of absolute intensity versus time

The normalized intensity changes about 60% from pH 7.7 to pH 3.15. Also, the plot is seen to be linear in the range of pH between pH 4.2 and pH 5.15. The plot confirms that the TIRF device configuration with type-II deposition method would also work as a pH-sensor. The response time is found to be about 3s.

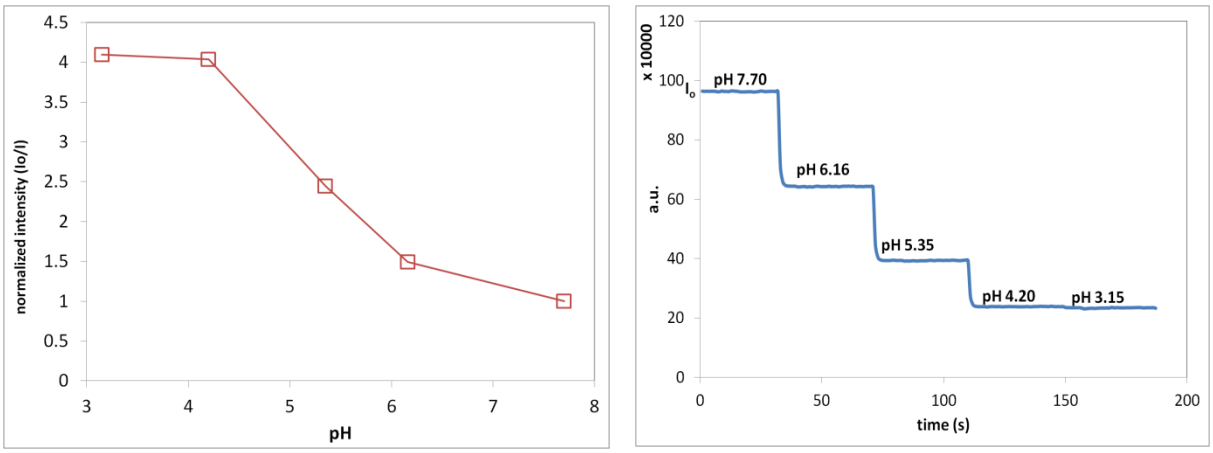

(a) (b)

Figure 7.9, (a) normalized intensity versus corresponding pH values for type-II pH-sensor (hydrothane) (b) plot of absolute intensity versus time

References

[1] J. R. Lakowicz, "Quenching of Fluorescence," in *Principles of Fluorescence Spectroscopy*, New York, Springer, 2006, pp. 277-330.

Chapter 8: Development and testing of the TIR-based device as O_2-based enzymatic H_2O_2 and lactose sensors

8.1 Introduction

The plastic TIR-based device discussed in chapter 6 can be developed into an O_2-based biosensor by using an O_2 sensitive dye and proper enzyme. As discussed earlier in chapter 5, $Ru(dpp)^3$ is an O_2 sensitive dye. The deposition method for $Ru(dpp)^3$ that uses Si-gel is discussed in chapter 5. The method of converting the TIRF chip into O_2 sensor and testing of it is discussed in section 8.2. The method of making H_2O_2 and lactose sensors from these O_2 sensors is presented in section 8.3. The apparatus setup, experimental procedure and results for the primary demonstration of the H_2O_2 sensor are given in section 8.4. The apparatus setup, experimental procedure and results for the primary demonstration of the lactose sensor are conveyed in section 8.5. In section 8.6, the apparatus setup, experimental procedure and results of the experiments done to find out important sensor parameters like limit of detection (LOD), sensitivity, linear range and response time for H_2O_2 sensor are discussed.

8.2 Development and testing of O_2 sensor

An O_2 sensor was made out of the original TIR device (given in chapter 6) using Si-adhesive gel based deposition method. For that, the deposition solution was made by mixing 200mg Si gel, 1mg $Ru(dpp)^3$ and 0.5ml chloroform. The dye layer was deposited by putting 3µl of this deposition solution on the core surface through the collection fiber hole. Using this method three such O_2 sensors were made. These O_2 sensors work on the principle of quenching of phosphorescence of $Ru(dpp)^3$. The phosphorescence intensity of $Ru(dpp)^3$ is quenched in proportion to the O_2 concentration. The O_2 concentration can be indirectly sensed by measuring the quenching of phosphorescence.

These O_2 sensor devices were tested to check if they worked to sense different O_2 concentration levels. For that, the phosphorescence levels for phosphate buffer solutions with two different O_2 concentrations were measured. One of the two solutions was anoxic and the other had O_2 concentration of 6.85 ppm. The later one was made by sparging air through a beaker of 1 liter phosphate buffer solution for 2 hours. The O_2 concentration was measured using an RDO probe (In-Situ Inc.). An oxidation reaction was used to make the anoxic solution. The oxidation of sodium sulfite (Na_2SO_3) is catalyzed by cobalt chloride ($CoCl_2$). In this reaction sodium sulfite eats up O_2 from its surrounding transforms into sodium sulfate (Na_2SO_4). Based on this reaction, a beaker of 1 liter phosphate buffer saline solution was made anoxic. For that, 100µl of $CoCl_2$ was mixed in the beaker and then 1ml of Na_2SO_3 was mixed in the PBS solution. The Na_2SO_3 ate up all the oxygen from the solution to make it anoxic, the RDO probe measured the O_2 concentration to be 0.05ppm.

The apparatus was setup as shown in figure 8.1. The TIRF O_2 sensor chip was attached to the table top using a double sided transparent tape. It was excited using an end-fire fiber coupled 470nm LED. The firing end of the fiber was fit in the fiber groove of the chip. The LED was driven by 30mA current through a current supply. A plastic optical fiber was set in the collecting fiber hole to collect the phosphorescence of the dye layer. The other end of the collecting fiber was connected to a fluorescence spectrometer (USB4000 FL, ocean optics). The spectrometer was set to record the phosphorescence intensity trace with one sample point every second. Each sample point was an integrated value of phosphorescence intensity over the spectral range of 610nm – 850nm. An inlet tube and a syringe were used to run the anoxic and 6.85ppm O_2 concentration solutions through the fluidic channel in that order. For each solution the spectrometer was made to record the trace for 200s recording 200 sample points for every trace.

The phosphorescence intensity point for each pH buffer solution was reckoned as an average of these 200 sample points. The spectrometer was stopped after recording phosphorescence intensity trace for the anoxic solution. Then, the channel was rinsed using DI water before it was refilled by the 6.85ppm [O_2] solution. Then, the phosphorescence intensity point for the 6.85ppm [O_2] solution was measured. This procedure and apparatus setup was repeated for all three O_2-sensor devices. The values of phosphorescence intensity were plotted versus their corresponding O_2 concentrations for all three sensors in a single chart. The chart is given in figure 8.2.

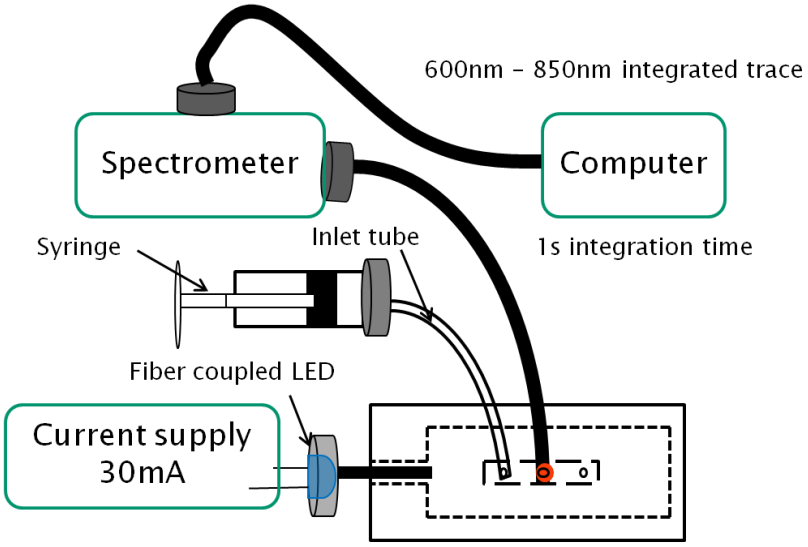

Figure 8.1, schematic of apparatus setup for testing the working of O_2 sensors

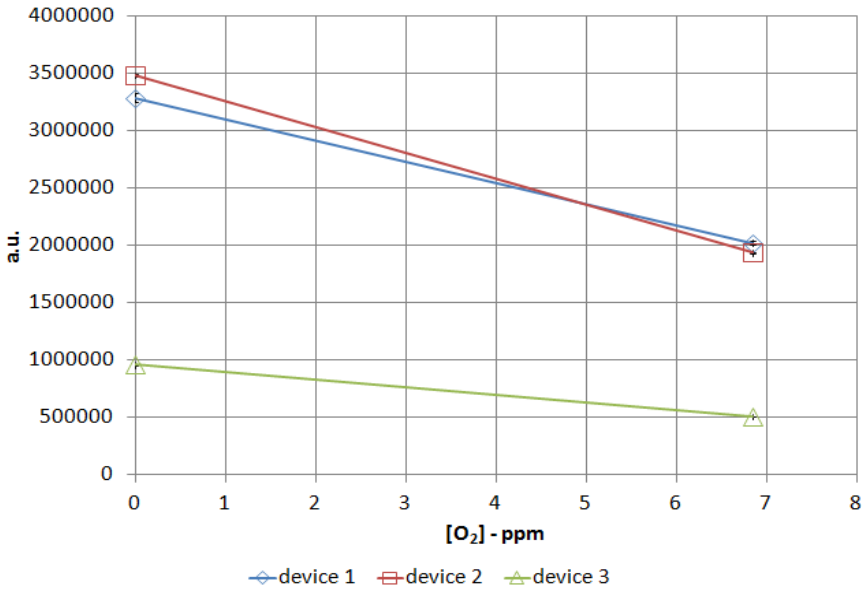

Figure 8.2, results of test of working of three O_2 sensor devices

All three devices showed about 40-50% change in phosphorescent intensity. As shown in figure 8.2, devices 1, 2 and 3 exhibited 38.47%, 44.43% and 47.05% change in phosphorescent intensity respectively from the anoxic solution to the 6.85ppm [O_2] solution. The differences in the %change values among the devices were due to some uncontrolled experimental parameters like device to device variability, drifts in fiber alignments and temperature difference. But importantly, all three devices showed significant amount of change in phosphorescence intensity. So, TIRF devices can be used as O_2 sensors or O_2-based biosensors. And the use of such sensors can be made more repeatable and efficient with proper control over the experimental parameters.

8.3 Development of H_2O_2 and lactose sensor

H_2O_2 and lactose sensors are O_2-based enzymatic biosensors and they work on the principles of catalysis of quenching molecules and quenching of phosphorescence of Ru(dpp)^3. Development of H_2O_2 and lactose sensors using TIR devices requires deposition of an enzyme layer (bio-component) above the dye layer. Quenching molecules (O_2 molecules) are catalysed

by the enzyme layer with concentration in proportion to the concentration of the target analyte molecules (H_2O_2 and lactose molecules). The catalyzed quenching molecules (O_2) diffuse through the enzyme layer and reaches to the dye layer ($Ru(dpp)^3$ layer) to quench the photoluminescence of the dye molecules ($Ru(dpp)^3$ molecules) in proportion to their concentration. The concentration of the target analyte molecules ([H_2O_2], [lactose]) can be measured by measuring the amount of quenching of the photoluminescence.

The enzyme used to make H_2O_2 sensor was catalase. The catalase causes catalytic decomposition of H_2O_2 molecules. Two H_2O_2 molecules get decomposed in two H_2O molecules and one O_2 molecule. In this way, the catalase generates O_2 molecules in proportion to the H_2O_2 concentration. In this scheme the phosphorescence intensity decreases with increase in H_2O_2 concentration. A layer of catalase should be immobilized on the dye layer to convert the TIRF O_2 sensor into a H_2O_2 sensor. Albumin from bovine serum (A9418 SIGMA) was used to immobilize the catalase enzyme on the deposited dye layer. For that, a mixture of aqueous solutions of enzyme and albumin was crosslinked using proper amount and concentration of gluteraldehyde and glycerol. A protocol was developed for making catalase-albumin solution for enzyme deposition. Accordingly, the solution was made by mixing 5µl of catalase enzyme, 45 µl of BSA (56mg/ml - bovine serum albumin), 1.19 µl of glycerol and 25 µl of 2.5% gluteraldehyde. Immediately after making the solution, 1.5µl of it was deposited on the dye layer and was cured for 30 minutes at room temperature before it crosslinked to provide the enzyme layer.

The enzyme used to make lactose sensor was lactose oxidaze. The oxidaze enzyme causes catalytic oxidation of lactose molecules. One molecule of O_2 oxidizes one molecule of lactose. In this scheme the phosphorescence intensity increases with increase in lactose concentration. The enzyme-albumin solution for deposition of lactose oxidaze enzyme was made

by mixing 20 µl Lox [100 mg/mL], 30 µl BSA [160mg/mL], 1.19 µl glycerol, 25µl 2.5% gluteraldehyde. Immediately after making the solution, 1.5µl of it was deposited on the dye layer and was cured for 30 minutes at room temperature before it crosslinked to provide the enzyme layer.

8.4 Primary demonstration of H_2O_2 sensor

The H_2O_2 sensor for primary demonstration of its working was made using the revised design-II of TIR chip. The experimental apparatus setup used for the experiment is shown in figure 8.3. The TIR device was attached to the table top using a double sided transparent tape. . It was excited using an end-fire fiber coupled 470nm LED. The firing end of the fiber was fit in the fiber groove of the device. The LED was driven by 30mA current through a current supply. A plastic optical fiber was set in the collecting fiber hole to collect the phosphorescence of the dye layer. The other end of the collecting fiber was connected to a fluorescence spectrometer (USB4000 FL, ocean optics). The spectrometer was set to record the phosphorescence intensity trace continuously with one sample point every second. Each sample point was an integrated value of phosphorescence intensity over the spectral range of 600nm – 850nm.

The dimensions of the channel for the revised design-II are 5mm x 15mm x 2.2mm, as discussed in chapter 6. Accordingly, the volume of the channel would be 165 mm^2, the channel could contain 165µl of fluid. As shown in the figure, a pipette was used to fill 165 µl of anoxic solution in the channel. The anoxic solution was prepared as discussed in section 8.2. After the spectrometer recorded considerable number of sample points of the trace for the anoxic solution, the H_2O_2 concentration in the channel was increased by 4mM step by step until no further decrease in the phosphorescence intensity was found with increase in H_2O_2 concentration. The H_2O_2 concentration in the channel fluid was increased in steps of 4mM by adding 2µl of 300mM

aqueous solution of H_2O_2 for each step. For each step, after increasing the concentration by 4mM, enough time was given for the spectrometer trace to settle down at a new intensity level. At each new intensity level, the trace was recorded at least for 60s before the concentration was again increased by 4mM. Figure 8.4 shows the trace recorded during the experiment.

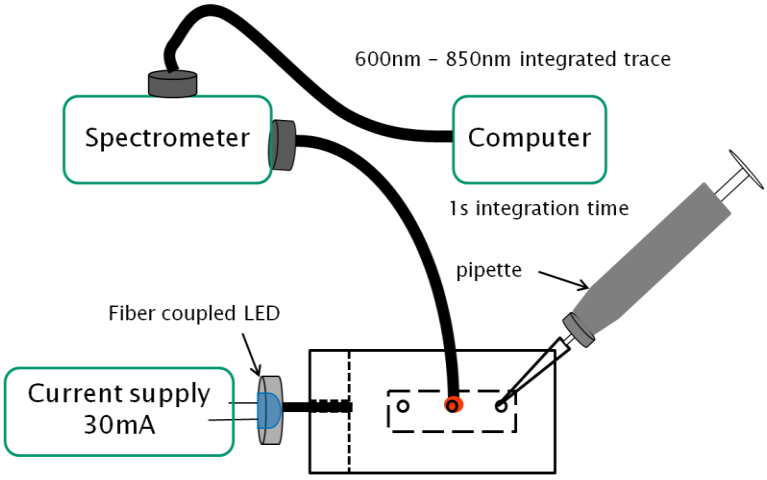

Figure 8.3, experimental apparatus setup for primary demonstration of H_2O_2 and lactose sensors

Adding 2µl of 300mM H_2O_2 solution in each step increases the H_2O_2 concentration in the channel fluid by 4mM only when addition on 2µl in the total amount of fluid in the channel is ignored. When this addition in the total amount of fluid is considered for each step, the actual concentration of H_2O_2 after each step is not a multiple of 4mM but it is different. The actual H_2O_2 concentration after each step is given in figure 8.4. In the figure, the settled intensity traces for the anoxic solution, for 28mM [H_2O_2] and 36mM [H_2O_2] are seen to ramp with positive slope with time (intensity increases with time). For other concentrations, the settled traces remain horizontal (constant with time). The linear increase in the phosphorescence intensity with time could be attributed to the decrease in O_2 concentration at a constant rate. There are several

mechanisms that affect the O_2 concentration in the fluid during the experiment. Diffusion of atmospheric O_2 into the channel fluid and catalytic decomposition of H_2O_2 increase the concentration of O_2 in channel fluid. The rate of decomposition of H_2O_2 depends on a few factors like the number of active sites on deposited enzyme layer, concentration of H_2O_2 in the fluid and amount of diffusion of H_2O_2 into the enzyme layer. All these factors together affect the rate and amount of increase of O_2 concentration in the channel fluid, and hence affect the amount of quenching of the dye layer. On the other side, the catalytic oxidation of Na_2SO_3 remains decreases the concentration of O_2 in the channel fluid. The steady state integrated trace of phosphorescence intensity for each step is due to the resultant effect of all these mechanisms.

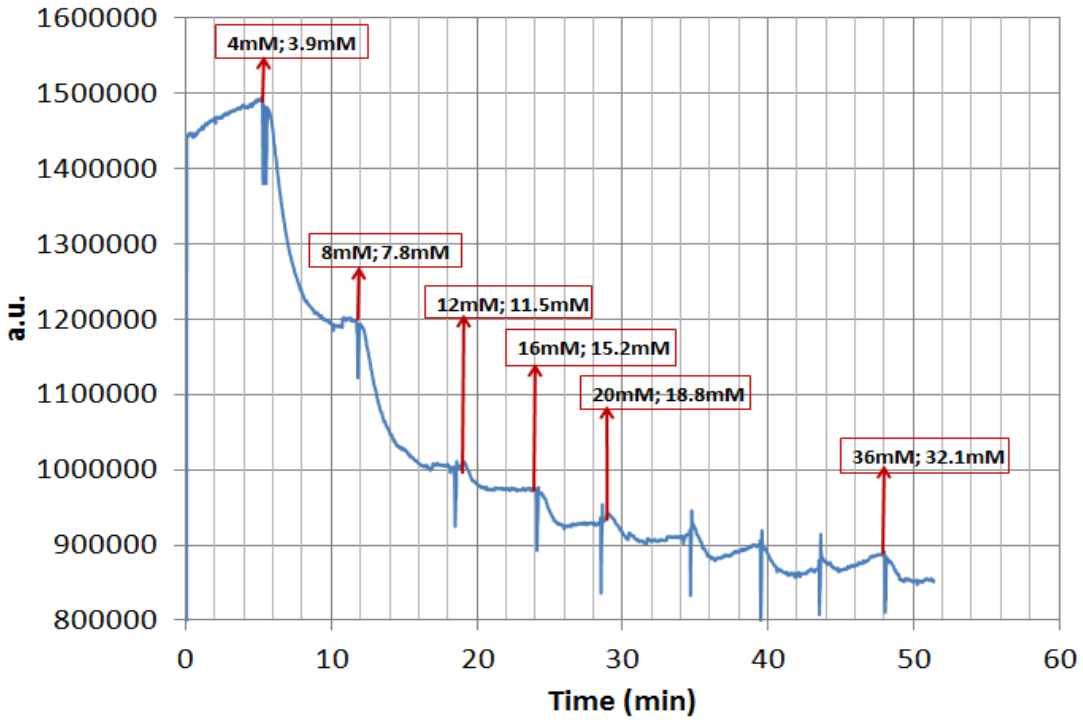

Figure 8.4, integrated trace of phosphorescence intensity for primary demonstration of H_2O_2 sensor

For the anoxic solution, there is no H_2O_2 available in the fluid. Therefore, the O_2 diffusing into the channel fluid from the atmosphere is the only source for increase of O_2

concentration. Since, the rate and amount of O_2 diffusion into the channel fluid through the PDMS channel-ceiling is very low, the mechanism of catalytic oxidation of Na_2SO_3 dominates for the anoxic solution. Therefore, the figure 8.4 showed a ramping trace for the anoxic solution, depicting a gradual decrease in O_2 concentration and quenching of phosphorescence. Moreover, for each step of H_2O_2 concentration above 28mM, the increase in $[H_2O_2]$ does not increase quenching of phosphorescence. It could be because of dye layer saturation, enzyme layer saturation or diffusion saturation. But, the ramping trace of intensity is still observed for 28mM $[H_2O_2]$ and 36mM $[H_2O_2]$. The cause of this phenomenon is not known, but it can be conceived as the effect of domination of Na_2SO_3 oxidation over all other mechanisms that can decrease O_2 concentration.

8.5 Primary demonstration of lactose sensor

A lactose sensor was made from the revised design type-II of the TIR device and was demonstrated to measure lactose concentrations in a range of 0.2mM to 0.9mM as a proof of concept. For the experiments the apparatus were set up the same way they were set up for H_2O_2 sensor demonstration as shown in figure 8.3.

The sensor works on a principle of dequenching of Ru(dpp)3 phosphorescence due to O2 consumption in the oxidation process of lactose molecules in the presence of oxidase enzyme. Therefore, the channel was filled with 165µl oxygenated DI water to start with, which was prepared as discussed in section 8.2. Then, 5µl of 300mM lactose solution was added step by step to increase the lactose concentration in the channel in 10mM steps. For each step the phosphorescence intensity trace was recorded as discussed in section 8.3. The resultant trace is shown in figure 8.5.

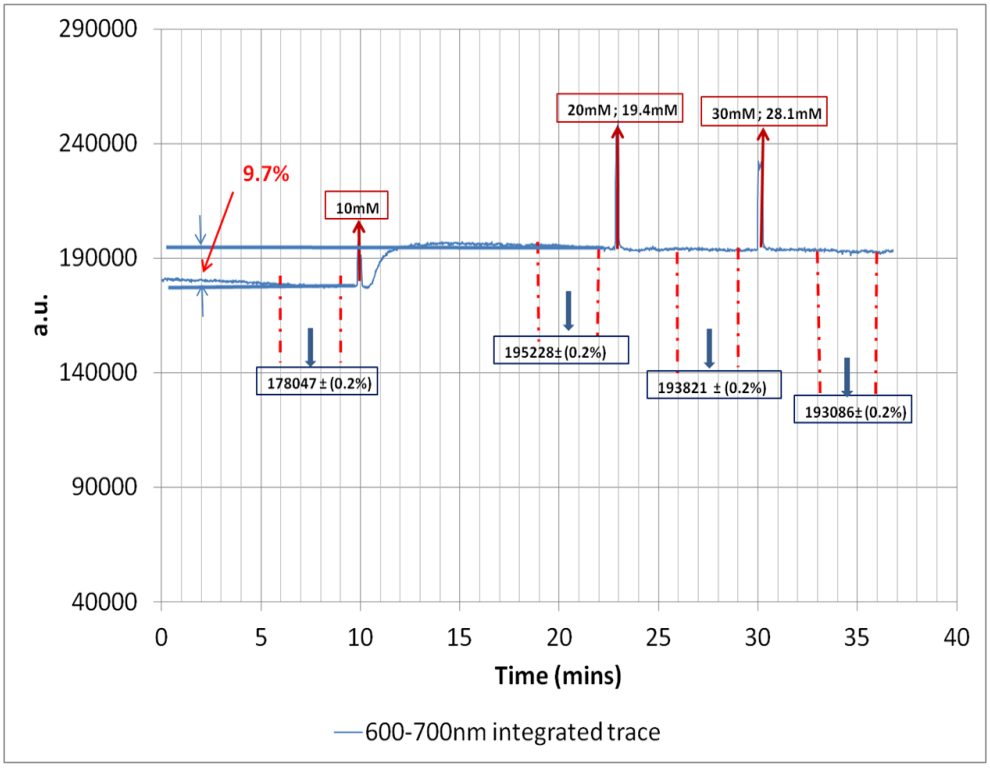

Figure 8.5, phosphorescence intensity trace for 10mM steps of lactose

As evident from the figure, the intensity increases by about 9.7% for first 10mM step, but it remains constant for two consecutive 10mM steps. It is because the 10mM step was larger than the detection range of the lactose sensor. Therefore, the lactose concentration was decided to be increased in smaller steps of 3mM by adding 1.5µl of 300mM lactose solution step by step. The phosphorescence intensity trace obtained for that is given in figure 8.6. The intensity was found to increase by 9.9% for first 3mM step increase but it was found constant for three consecutive 3mM steps, as shown in the figure. So, the detection range was smaller than 3mM as well. For that reason, the lactose concentration was increased in 0.2mM steps by adding 3µl of 10mM lactose solution step by step. Figure 8.7 shows the intensity trace for that, which shows step by step increase in intensity for lactose concentrations from 0.2mM to 1.0mM.

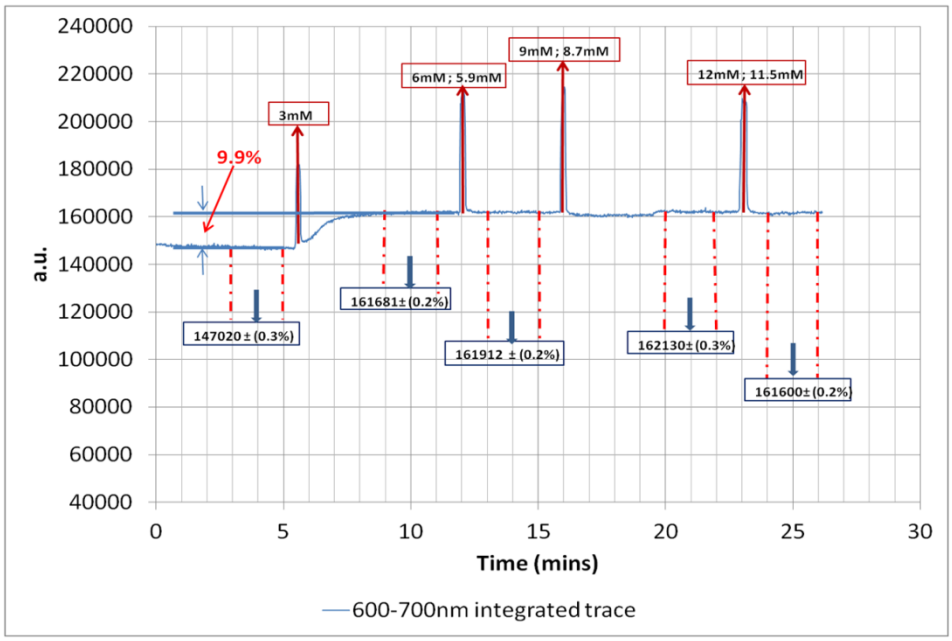

Figure 8.6, phosphorescence intensity trace for 3mM steps of lactose

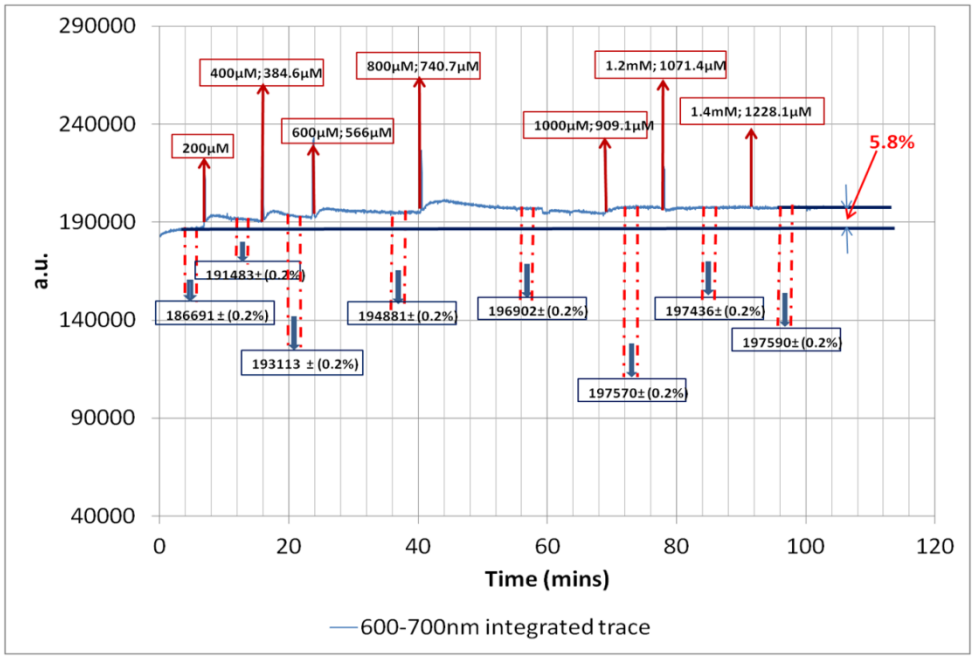

Figure 8.7, phosphorescence intensity trace for 0.2mM steps of lactose

A data point was calculated by averaging 120 sample points for each step between 0.2mM and 1.0mM as shown in figure 8.7. Using these data points, a plot of %change in

intensity values versus corresponding lactose concentrations was produced which is given in figure 8.8. It is seen that the sensor gave a linear response from 0.2mM to 1.0 mM.

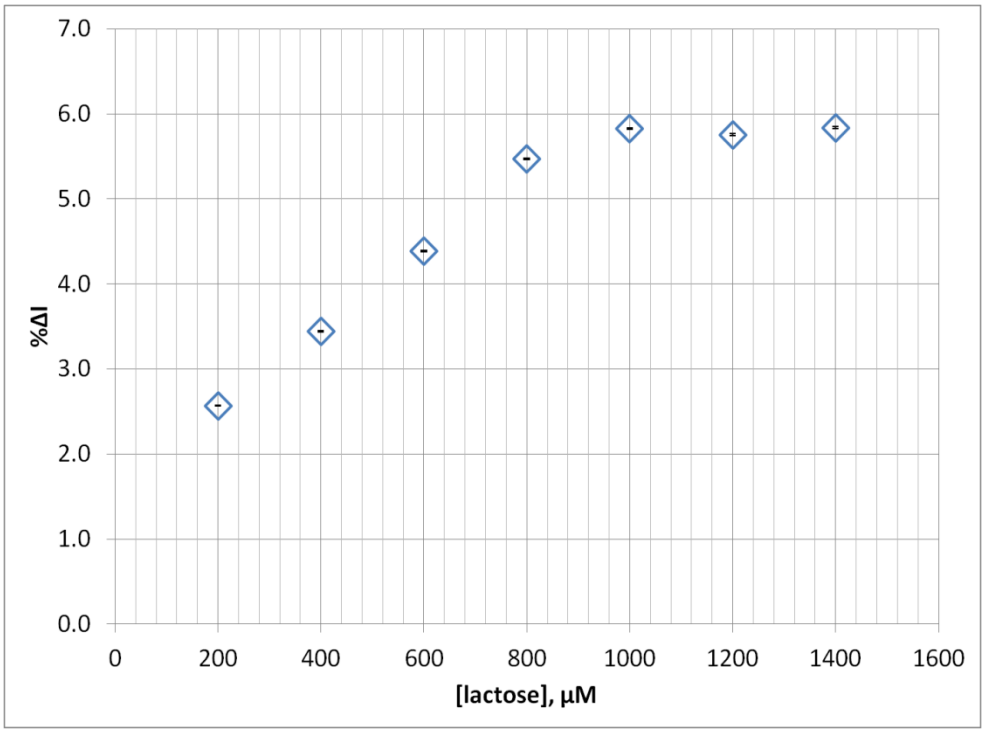

Figure 8.8, a plot of %change in phosphorescence intensity versus corresponding lactose concentration

The increase in the total fluid amount in the channel was ignored while calculating the step increase in lactose concentrations. So, actual lactose concentration after each step increase , which were calculated by considering the increase in the total fluid amount after each step, are labeled in the plots given in figure 8.5, figure 8.6 and figure 8.7.

All of the O2 dissolved in the channel fluid gets used up at 1mM lactose concentration by the oxidase enzyme. Therefore, for larger lactose concentrations there remains no O2 in the channel to be consumed any further. And that's the reson for such a small detection range of lactose sensor. However, the detection range of the sensor can be improved if the O2 in the channel fluid can be replenished after each step. A flow-cell based device design with fluid

reservoir was made to replenish the channel fluid indirectly replenishing O2. Detailed information about the design and functioning of such a device is presented in chapter 9 of this thesis.

8.6 Measurements of performance parameters of H_2O_2 sensor

The usefulness of the TIR-based device as an enzymatic biosensor application was investigated by combining it with catalase to realize an enzymatic H_2O_2 sensor. H_2O_2 sensor was chosen because a large number of enzymatic and non-enzymatic H_2O_2 sensors are available to compare their performance to the TIR-based device. The H_2O_2 sensor was made by depositing a layer of catalase enzyme on top of the $Ru(dpp)^3$ layer as presented in section 8.3. But, for this study, the $Ru(dpp)^3$ layer was deposited using HydroThane (a hydrophilic thermoplastic polyurethane elastomer, AdvanSource Biomaterials). HydroThane has the ability to rapidly absorb water while maintaining high tensile strength and high elongation, resulting in a permanently lubricious polymer [1], which makes it biodurable and biocompatible and hence very appropriate to use as a substrate for depositing dye in biosensor applications. HydroThane, with 15% water absorption capacity, was dissolved in chloroform to produce 2% (w/v) solution (solution-A). Ru(dpp) dye was dissolved in chloroform to produce 0.5% w/v solution (solution-B). Solution-A and Solution-B were mixed in a 1:1 proportion to make the deposition solution. The deposition solution in 3µl volume was taken using a pipette and was deposited on the core surface through the excitation fiber hole of the TIR device. The chloroform evaporated in about 10 minutes after deposition and a film of HydroThane attached the dye firmly to the core surface.

8.6.1 Apparatus setup and experimental procedure for measuring calibration curves

Figure 8.9 shows the apparatus setup used for the experiment. The collected phosphorescence was fed to the spectrometer without using any optical filter. The spectrometer was set to record the phosphorescence intensity trace continuously with one sample point every

second. Each sample point was an integrated value of the spectrum over the range of 400nm – 850nm and therefore considering the scattered excitation light as a part of signal.

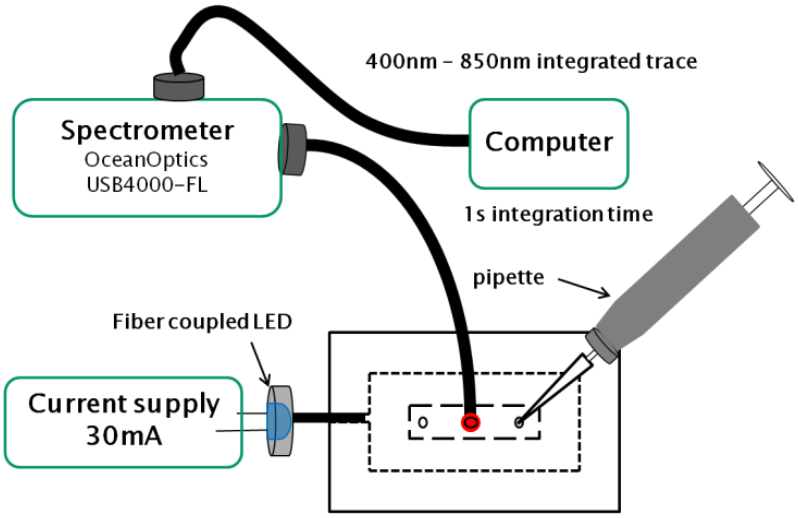

Figure 8.9, apparatus setup used to measure calibration curves for the Hydrogen Peroxide sensor

The calibration curve was obtained by measuring and plotting the phosphorescence intensity for different concentrations of H_2O_2. The experimental procedure was designed to extract the device-performance parameters including limit of detection, linear range, sensitivity and response time from a single experiment. Phosphate buffered saline (PBS) was used as a substrate to make analyte solutions for the blank measurements (to measure detection limit) and for the measurements of the calibration curve. Since, the quenching of the phosphorescence is O_2 sensitive, the substrate solution (PBS) was made anoxic (null content of dissolved O_2) before it was used to make analyte (H_2O_2) solutions. The expedited oxidation reaction of sodium sulphite (Na_2SO_3) in the presence of cobalt chloride ($CoCl_2$) was used to consume all dissolved O_2 in the PBS solution making it anoxic. Cobalt chloride and sodium sulphite were added in PBS solution in 1:10000 and 1:1000 proportions respectively. The dissolved O_2 content of the anoxic PBS solution was measured to be 1.0±0.2 nM over 15minutes using an RDO probe from Insitu Inc.

The anoxic PBS solution thus made was used to make analyte (H_2O_2) solutions with different concentrations of 1.5mM, 15mM, 37.5mM and 150mM respectively. These solutions were packed in air-tight vials immediately after they were made.

The device has a fluid cell with dimensions 5mm x 15mm x 2.2mm, which is equal to a volume of 165mm^2. So, the cell's fluid capacity is 165µl. Therefore, 165µl of the anoxic PBS substrate solution was used to obtain blank measurements. A total of 7 such measurements were taken. For each blank measurement, the spectrometer trace was recorded for 60s. The spectrometer software recorded one sample point every second giving 60 sample points for each such trace. The 60 sample points were averaged to obtain one corresponding data point. An average of seven data points was considered the blank measurement.

Then, the spectrometer was made to record the trace continuously without stopping. The concentration of H_2O_2 in the fluid cell was increased in 5µM steps by adding 0.5µl of 1.5mM anoxic H_2O_2 solution using a pipette step by step. For each new step, the spectrometer trace was monitored to see if perceivable decrement in the intensity was found. No decrease in phosphorescence intensity level was found for 5µM H_2O_2 concentration, but it was observed for 10µM H_2O_2 concentration. Therefore, the H_2O_2 concentration corresponding to the first such perceivable decrement was 7.5 ± 2.5 µM, which was the experimental detection limit.

After finding the experimental LOD, the H_2O_2 concentration was increased in approximately 20µM steps by mixing 2µl of 1.5mM H_2O_2 solution until the total concentration in the fluid cell was 200µM. Then, the concentration was increased in approximately 200µM steps by mixing 2µl of 15mM H_2O_2 solution till the total concentration was 1mM. Then, the concentration was increased in 3mM steps until no further change (decrease) in the phosphorescence intensity with increase in concentration was found. The increase in the volume

of the fluid in fluid cell due to mixing of H_2O_2 solution during each step was not considered while estimating the step value of increase. So, the actual step increase in H_2O_2 concentration would be different than 20µM/200µM/3mM for each step. For each step, enough time (about 15minutes) was given to the spectrometer trace to settle down to a new intensity level (quenched/decreased intensity level). The trace was recorded for 60s after it settled down for each step and then the concentration was increased by the next step. For each steady trace, the 60 sample points were averaged to obtain a single corresponding data point. Each such data point represented phosphorescence intensity at corresponding H_2O_2 concentration. Normalized phosphorescence intensity values were obtained by dividing the blank measurement value (I_0) by the data points (I). The normalized phosphorescence intensity values (I_0/I) were plotted against the corresponding H_2O_2 concentrations to obtain calibration curves. The standard deviations in the data points on the calibration curves were obtained from standard deviations in the corresponding blank measurement and phosphorescence intensity values.

Three iterations of the experiment were done to obtain three calibration curves for one such H_2O_2 sensor.

8.6.2 Results and discussion

The increase in the volume of the fluid in the fluid cell due to mixing of H_2O_2 solution in each step was considered while calculating the actual H_2O_2 concentration after each step. Figure 8.10 shows the calibration curves obtained for three iterations plotted with the actual concentration values on horizontal axis. The vertical error bar for each data point on the calibration curves represents two times the standard deviation in the data point. The calibration curves exhibited non-linearity for very small H_2O_2 concentrations as well as for relatively large H_2O_2 concentrations, as shown in the figure.

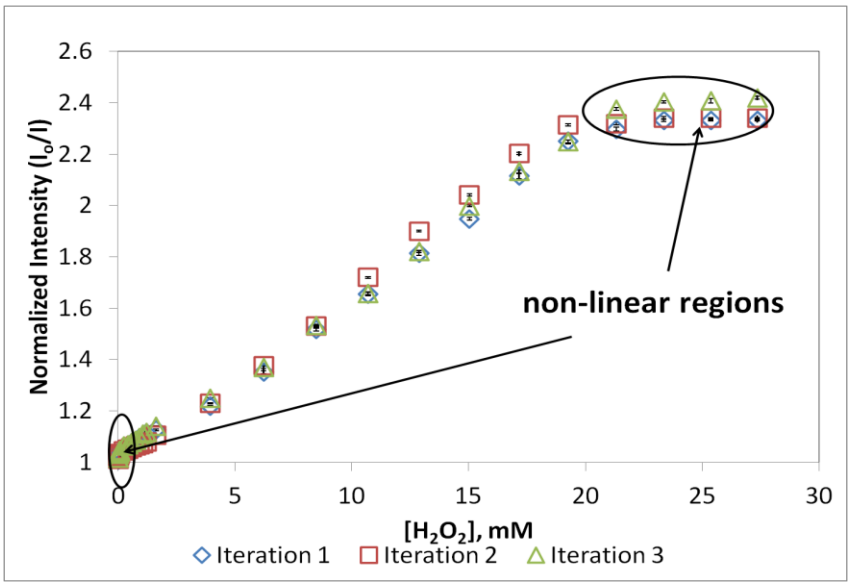

Figure 8.10, calibration curves for all three iterations of the H_2O_2 sensor

By the visual inspection, the enzyme layer was found to cover only 90-95% of the dye layer. Remaining 5-10% dye layer is easily accessible to the quencher molecules (O_2) catalyzed by the enzyme active sites on the surface of the enzyme layer. At very small concentrations the enzyme-covered dye layer remains inaccessible to the quencher molecules, which differs the quenching dynamics of easily accessible dye from that of the "difficult to access" dye producing non-linearity of the calibration carve at very small concentrations.

To elaborate further, the easily accessible dye is likely to have more sensitivity to O_2 molecules than the "difficult to access" dye would have at small concentrations. In this scenario, the resultant phosphorescence is contributed by both the parts of the dye layer. But, at just a little large concentration, all of the easily accessible dye gets maximally quenched contributing zero sensitivity to O_2 molecules then onwards. And then, the O_2 sensitivity of the phosphorescence is totally governed by the "difficult to access" dye. Thus, the non-linearity at very small H_2O_2 concentrations is hypothesized to be due to the non-ideal behavior of the enzyme-dye layer

interface. The nonlinearity at higher concentrations was due to the combined effect of quenching of all the dye molecules and diffusion saturation of the enzyme layer.

The non-linearity at small concentrations was modeled by a two site model [2, 3] available in literature. This model is represented by a modified stern-volmer equation 8.1.

$$\frac{I_0}{I} = \frac{1}{\frac{f_1}{1+K_{sv1}[Q]}+\frac{f_2}{1+K_{sv2}[Q]}} \tag{8.1}$$

Accordingly, the easy to access part of the dye layer was modeled to contribute 0.05 fraction ($f_1 = 0.05$) of the total phosphorescence and the "difficult to access" part of the dye layer was modeled to contribute 0.95 fraction ($f_2 = 0.95$) of the total phosphorescence. Using this fraction model, the equation 8.1 was fit to all three calibration curves for small concentration. Figure 8.11 gives the non-linear part of the calibration curves and best fitted trendlines to it according to equation 8.1. The linear part of the calibration curves was also modeled by the same fraction model, but for that the stern-volmer sensitivity of the "easy to access" dye was considered to be zero ($K_{sv2} = 0$, to model zero sensitivity to O_2) according to the aforementioned elaboration. Figure 8.12 gives the linear part of the calibration curves and best fitted trendlines to it. Fitting parameters of the trendlines with R^2 values for both parts of the calibration curves are listed in Table 8.1. The values of the fitting parameters prove the hypothesis about the fraction model to be true.

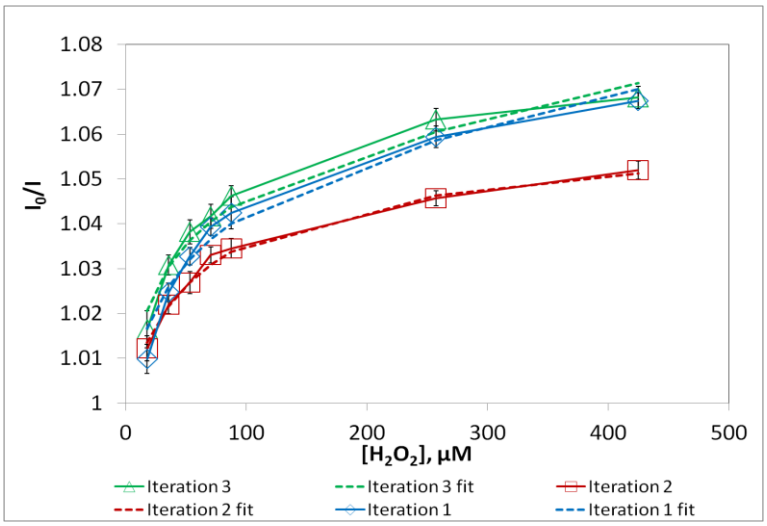

Figure 8.11, non-linear part of the calibration curves for small H_2O_2 concentrations

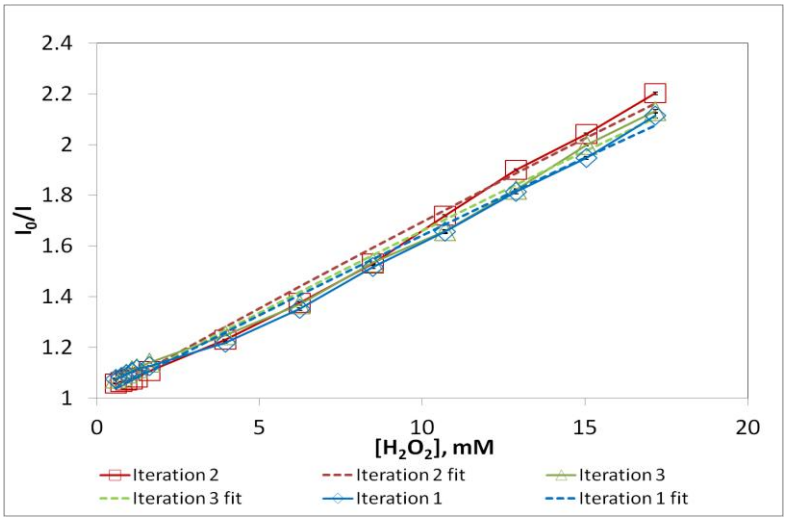

Figure 8.12, linear part of the calibration curves for relatively large H_2O_2 concentrations

Detection limits for all three iterations were calculated from the fitted trends to the non-linear calibration curves. They are 1.7µM, 2.9µM and 2.1µM for iteration 1, iteration 2 and iteration 3 respectively. So, the average detection limit for the H2O2 sensor is 2.2±0.6 µM. Moreover, the linear detection range of the sensor is found to be 0.1mM – 20mM. According to the occupational health and safety administration, inhalation of H_2O_2 vapor in 7ppm (i.e.,

0.2mM) concentration causes lung irritation. This permissible H_2O_2 concentration can be measured by the linear detection range of the designed H_2O_2 sensor.

Table 8.1, fitting parameters for non-linear and linear parts of the calibration curves

	Iteration #	**f_1**	**f_2**	**K_{sv1} $(\mu M)^{-1}$**	**K_{sv2} $(\mu M)^{-1}$**	**R^2**
Non-linear	1	0.05	0.95	0.025	0.00005	0.9667
	2			0.020	0.00001	0.9912
	3			0.035	0.00005	0.9749
Linear	1	0.05	0.95	0	0.000070	0.9921
	2				0.000076	0.9933
	3				0.000072	0.9921

The linear range and limit of detection values of the plastic TIR-based hydrogen peroxide sensor were compared to those of some enzymatic hydrogen peroxide sensors reported. Table 8.2 gives this comparison. The detection limit of the present H_2O_2 sensor device is among the best in available luminescence-based enzymatic hydrogen peroxide sensors. This detection limit is obtained without using any optical filters, which corroborates very strong reduction of excitation light in the signal.

Table 8.2, detectable range and detection limit for several luminescence based enzymatic H_2O_2 sensors

Reference	**Detectable range**	**Detection limit**
TIR-based	10µM – 20mM	2.2 ± 0.6 µM
Mills et al [4]	0.01M – 1M	0.1 mM
Ortega et al [5]	0.1 mM – 1 mM	-
Voraberger et al [6]	0.03M – 0.6M	-
He et al [7]	4.4 µM – 0.53 mM	-
Arnold et al [8]	-	10 µM
Uchiyama et al [9]	5µM – 0.2mM	2.0 µM

References

[1] AdvanSource biomaterials, [Online]. Available: http://www.advbiomaterials.com/pdf/HydroThane%20Factsheet.pdf.

[2] E. R. Carraway, J. N. Demas, B. A. DeGraff and J. R. Bacon, "Photophysics and Photochemistry of Oxygen Sensors Based on Luminescent Transition-Metal Complexes," *Analytical Chemistry,* no. 63, pp. 337-342, 1991.

[3] W. Xu, R. C. McDonough III, B. Langsdorf and B. A. DeGraff, "Oxygen Sensors Based on Luminescence Quenching: Interactions of Metal Complexes with the Polymer Supports," *Analytical Chemistry,* no. 66, pp. 4133-4141, 1994.

[4] A. Mills, C. Tommons, R. T. Bailey, M. C. Tedford and P. J. Crilly, "Reversible, fluorescence-based optical sensor for hydrogen peroxide," *Analyst,* no. 132, pp. 566-571, 2007.

[5] E. Ortega, S. d. Marcos and J. Galban, "Fluorometric enzymatic autoindicating biosensor for H2O2 determination based on modified catalase," *Biosensors and Bioelectronics,* no. 41, pp. 150-156, 2013.

[6] H. S. Voraberger, W. Trettnak and V. Ribitsch, "Optochemical hydrogen peroxide sensor based on oxygen detection," *Sensors and Actuators,* no. 90, pp. 324-331, 2003.

[7] F. He, F. Feng, S. Wang, Y. Li and D. Zhu, "Fluorescence ratiometric assays of hydrogen peroxide and glucose in serum using conjugated polyelectrolytes," *Material Chemistry,* no. 17, pp. 3702-3707, 2007.

[8] S. Uchiyama and Y. Sano, "Hydrogen Peroxide Sensor with Bienzyme Membrane Based on Antagonism of Peroxidase Reaction to Tyrosinase Reaction Using Common Substrate," *Electroanalysis,* vol. 12, no. 11, pp. 817-820, 2000.

[9] M. A. Arnold, X. Zhou and R. S. Petsch, "Gas-sensing Internal Enzyme Fiber Optic Biosensor for Hydrogen Peroxide," *Talanta,* vol. 41, no. 5, pp. 783-787, 1994.

Chapter 9: Miscellaneous work

9.1 Introduction

This chapter covers some miscellaneous work done during the progress of this thesis work. Section 9.2 describes the design and fabrication of TIR-based multi-channel device with four channels. The multi-channel device was designed to investigate its use for simultaneous sensing of multiple analytes. In section 9.3, the design of a single channel device with COC as the waveguide core is discussed. A pH-sensor made of COC-core is demonstrated as a proof of concept using the PVA-based deposition method of fluoresceinamine. Section 9.4 talks about a flow-cell based device design with fluid reservoir, which was proposed to increase the linear range of the lactose sensor discussed in Chapter 8. Section 9.5 covers the results of the experiments done to investigate wavelength dependence of quenching of Ru(dpp).

9.2 Multi-channel sensor device

A multi-channel device was made using the same fabrication technique and processes as were used to fabricate the single channel device. But, multi-channel molds for PDMS upper cladding and PDMS lower cladding were designed. Figure 9.1 shows an acrylic mold designed for PDMS lower cladding. It consists of features for four sockets for waveguide cores of 5mm x 20mm dimensions and four grooves of 2mm x 5mm dimensions for excitation fibers. Figure 9.2 shows an acrylic mold designed for PDMS upper cladding. It consists of features of 2mm x 10mm dimensions for four fluid channels. Four PMMA slabs of 5mm x 20mm dimensions were cut by a commercial plastic supplier from a 3mm thick PMMA sheet using CO_2 laser. Then, these core slabs were put together with the PDMS lower cladding and upper cladding using air-Corona discharge technique, similarly as it was done for the single channel model discussed in Chapter 6. Two holes for inlet-outlet and one hole for collection fiber were punched in the ceiling of each fluid channel. Figure 9.3 shows schematic top view of the multi-channel design.

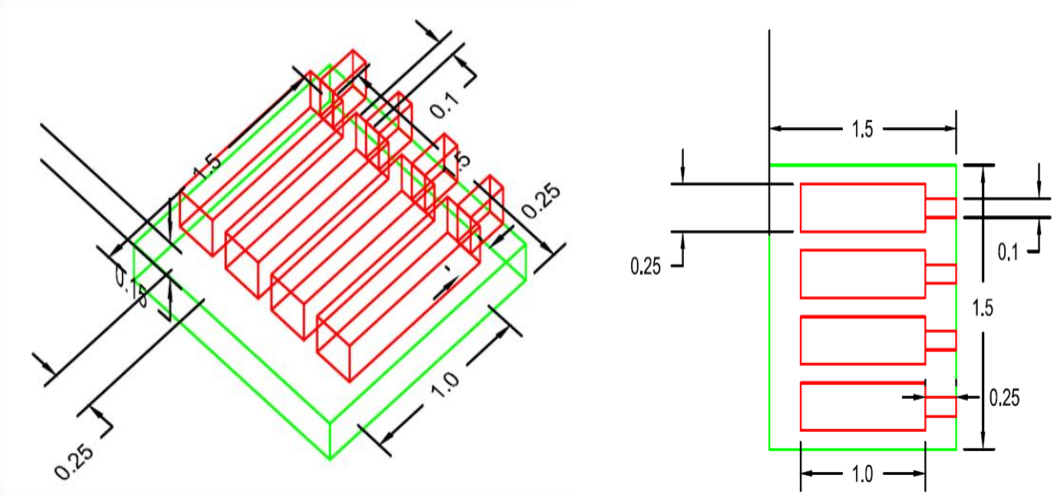

Figure 9.1, (a) AutoCAD home view of the mold for PDMS lower cladding consisting of features for sockets and grooves (b) AutoCAD top view of the mold for PDMS lower cladding

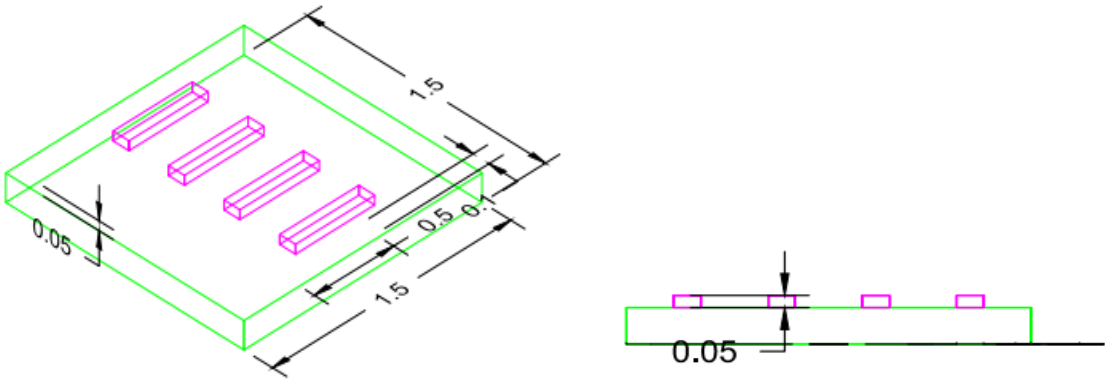

Figure 9.2, (a) AutoCAD home view of the mold for PDMS upper cladding consisting of features for fluid channels (b) AutoCAD side view of the mold for PDMS upper cladding

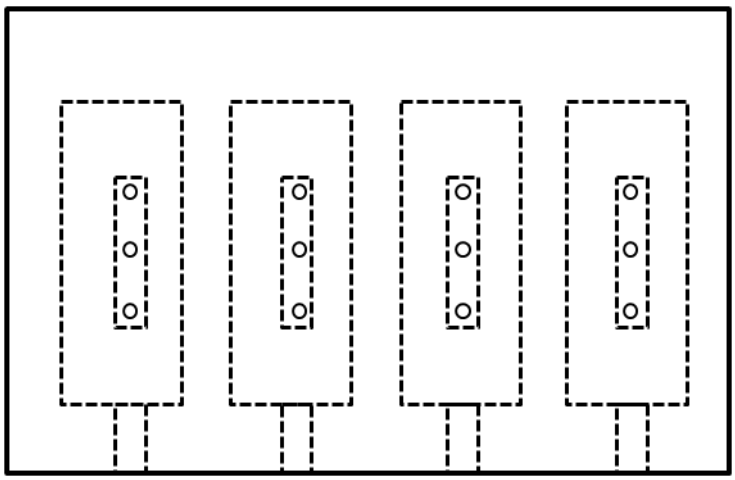

Figure 9.3, schematic top view of the multi-channel TIR-based device showing punched holes in the channels' ceilings

9.3 Single channel device with COC as the waveguide core material

Auto-fluorescence and thermoplastic properties of COC material are similar to that of PMMA, as discussed in Chapter 4. Unlike PMMA, COC exhibits excellent chemical resistance to Ketones and Esters. In contrast, COC is significantly costlier than PMMA. So, due to the superior chemical resistance and comparable auto-fluorescence of COC, it can be used as the waveguide core material of TIR-based device for the applications where resistance to Ketones and Esters is more important than the cost of the final device. With this motivation, a single channel device with TIRF design geometry with smaller interface area (discussed in Chapter 6) using COC as the waveguide core was fabricated. For that, a slab of 10mm x 20mm was saw-cut from an injection molding grade of COC (from Topas). The COC grade was found to melt with use of CO_2 laser on it at all power levels. Therefore, it was saw-cut. Then, the saw-cut edges were polished using sandpapers with 30μm, 15 μm, 3 μm, 1 μm, 0.3 μm and 0.03 μm grits respectively. The COC waveguide core with polished edges was then bonded with PDMS claddings using the technique of 3-APTES treating the COC slab followed by air corona

discharge [1]. As discussed in Chapter 6, the same technique was used to bond PMMA to PDMS.

A pH-sensor was designed by depositing fluoresceinamine on the COC waveguide core using the polyvinyl alcohol-based method. This method of deposition is discussed in Chapter 5. The pH-sensor was demonstrated by measuring the fluorescence intensity of the sensor for pH buffer solutions with pH 3.15, 4.20, 5.15, 6.16 and 7.42 respectively. The fluorescence intensity at pH 7.42 (I_0) was considered baseline reading, and using that the % change (%ΔI – [{(I_0-I)/I_0}*100]) in fluorescence intensity was measured for all other pH buffer solutions. Figure 9.4 gives a plot of %ΔI versus pH for the COC-based pH sensor.

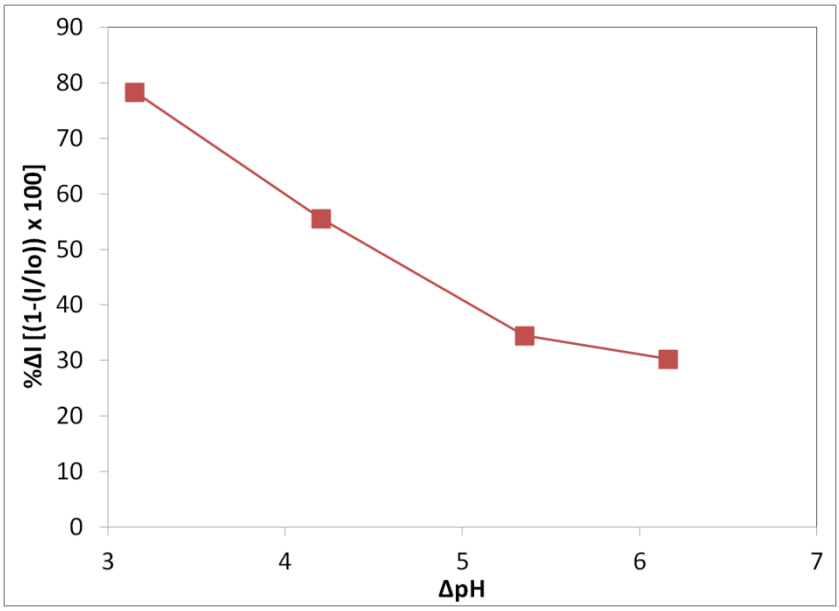

Figure 9.4, a plot of %ΔI versus pH for the COC-based pH sensor for proof of concept

The figure shows that the sensor gives successive decrease in fluorescence intensity going from pH 7.42 to pH 3.15. This proves that the device can be used as fluorescence/photoluminescence based biosensor.

9.4 A flow-cell based TIR device with fluid reservoir

As discussed in Chapter 8, the enzymatic lactose sensor based on oxidase enzyme demonstrated a linear range up to 750μM, which is very low for its applications in industrial flow control and breweries. For these applications, a linear range of up to 70-80mM is desired. The low linear range of the lactose sensor is attributed to the depletion limited mechanism of sensing. The oxidase enzyme consumes the dissolved O_2 from the fluid in the fluid cell and oxidizes lactose molecules. The amount of dissolved O_2 in the fluid cell is limited due to the limited amount of fluid. And all of the dissolved O_2 gets consumed for 750μM lactose concentration, which gives very low linear range. To increase the linear range, the O_2 content in the fluid must be replenished. O_2 can be replenished continuously by continuously replenishing the fluid in the fluid cell. Optimum rate of O_2 replenishment depends on O_2 diffusion and O_2 consumption dynamics. For easy modeling and handling of dynamics, it is required to have homogeneous flow of fluid through the fluid cell.

Continuous flow of fluid with a constant flow rate can be obtained using external injection pump. And fluid can be injected into fluid cell through inlet hole. The device designs (Revised design-I and II, Chapter 6) have very large dimensions of fluid cell compared to the dimensions of inlet hole. Therefore, an attempt to have a continuous flow of fluid creates dead zones in the fluid cell. The fluid in dead zones is never replenished, which affects the modeling and handling of O_2 replenishment dynamics making them more difficult.

To simplify the modeling and handling of O_2 replenishment dynamics, a flow cell-based device with a fluid reservoir was designed and fabricated. The schematic views of the design are given in figure 9.5. The device consists of a fluid reservoir with 4.4ml fluid capacity, which opens up in its base to a flow cell of 150μl capacity as shown in figure 9.5(b). The flow rate of fluid through the flow cell is controlled by controlling the height of the fluid column in the

reservoir. The column height could be maintained constant by replenishing the reservoir at desired rate using injection pump. This design could facilitate homogeneous flow of fluid through the flow cell at desired flow rate.

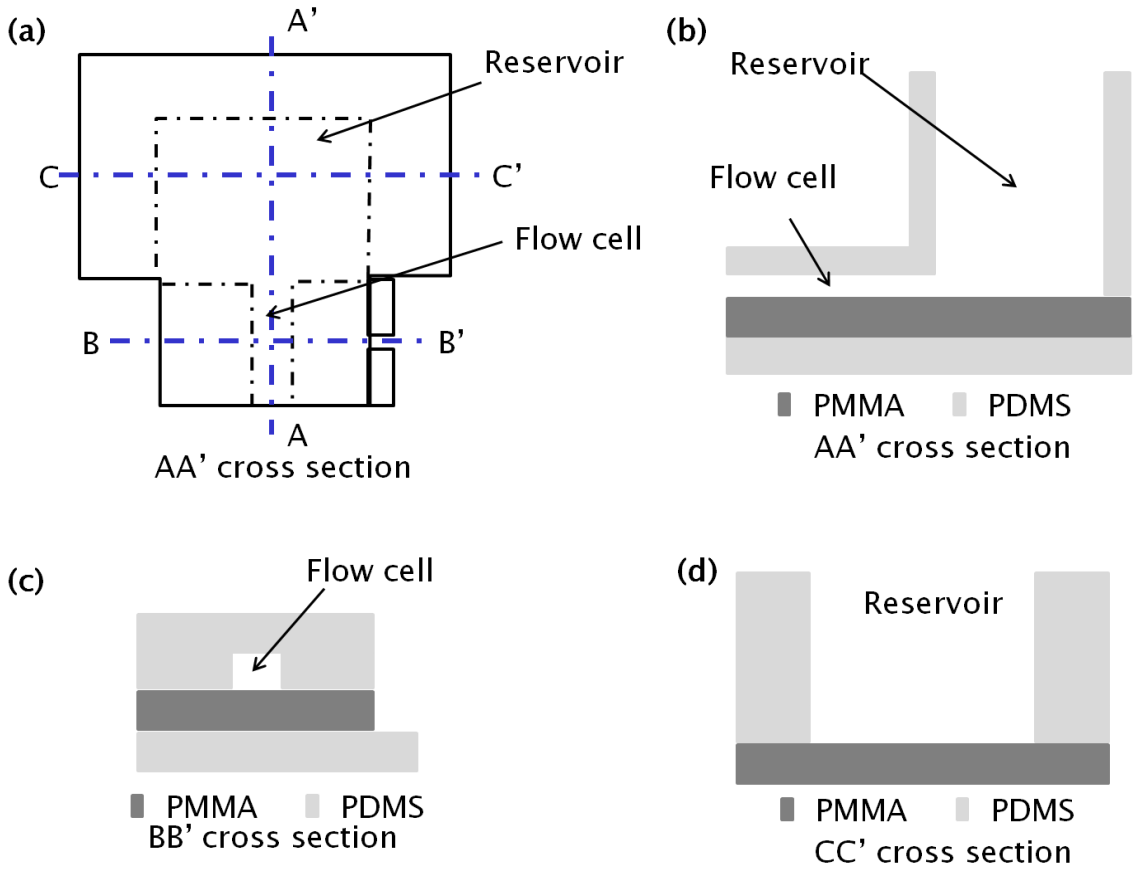

Figure 9.5, (a) Schematic top view of the flow cell based TIR device with fluid reservoir (b) AA' cross section of the device showing the flow cell and the fluid reservoir (c) BB' cross section of the device showing the flow cell (d) CC' cross section of the device showing the reservoir

The flow cell and the reservoir were molded in PDMS cladding. The bottom floor of the flow cell and the reservoir was a PMMA slab, which also acted as the waveguide core. Figure 9.5 (c) shows PDMS lower cladding consisting of a fiber groove. A layer of photoluminescent dye and enzyme can be deposited on the bottom of the flow cell to use this design as an enzymatic biosensor.

9.5 Wavelength dependence of quenching of Ru(dpp) phosphorescence

In this section, it is investigated that on which wavelengths of the wide spectrum of Ru(dpp) phosphorescence the quenching by O_2 molecules have dominant effect. For that, the phosphorescence spectrum of Ru(dpp), which spans from 550nm to 850nm, was divided in multiple narrow width windows and then signal to noise ratios for change in phosphorescence intensity upon quenching were investigated for all the windows. As discussed in Chapter 8, the catalyzed oxidation process of sodium sulphite in presence of cobalt chloride was used to change O_2 level to obtain a change in phosphorescence level due to quenching/dequenching.

Figure 9.6 shows the apparatus setup used for the experiment. Device design type-II was used with Si-gel based deposition of Ru(dpp) for the experiments. The fluid cell was filled with 150µl of DI water mixed with 1µl of $CoCl_2$. Then, the spectrometer was set to collect and save the phosphorescence spectrum every second. It was made to do it for 600s. Then, 15µl of Na_2SO_3 was added in the fluid of the fluid cell while the spectrometer was collecting. After 600 more seconds the spectrometer was stopped. So, at the end of data collection, we had 1200 files collected every second with each containing phosphorescence spectrum. The files were named spectrum1 to spectrum1200, each file name representing the time it was collected on. Then using the MATLAB program, each of the spectra was divided in 20nm windows between 550nm to 850nm. The spectrum was integrated over each such window giving one integrated value corresponding to each such window. Figure 9.7 shows how a spectrum was divided in 20nm windows. As shown, the windows were named window#1, window#2 and so forth.

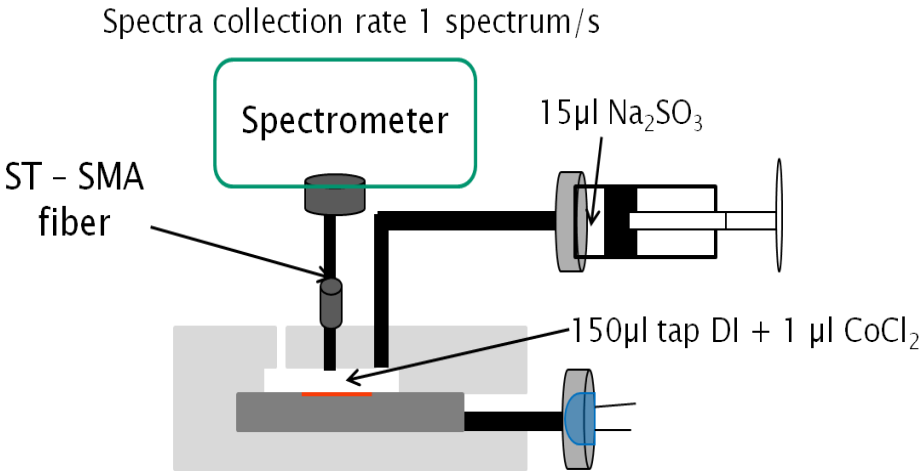

Figure 9.6, Apparatus setup for the experiment investigating wavelength dependence of quenching

The integrated values corresponding to windo#1 for all 1200 spectra were plotted versus the time they were collected on. It was done for all the 20nm windows. The resultant plots are shown in figure 9.8. The effect of dequenching of phosphorescence on each of the windows can be seen by the step increase in intensity.

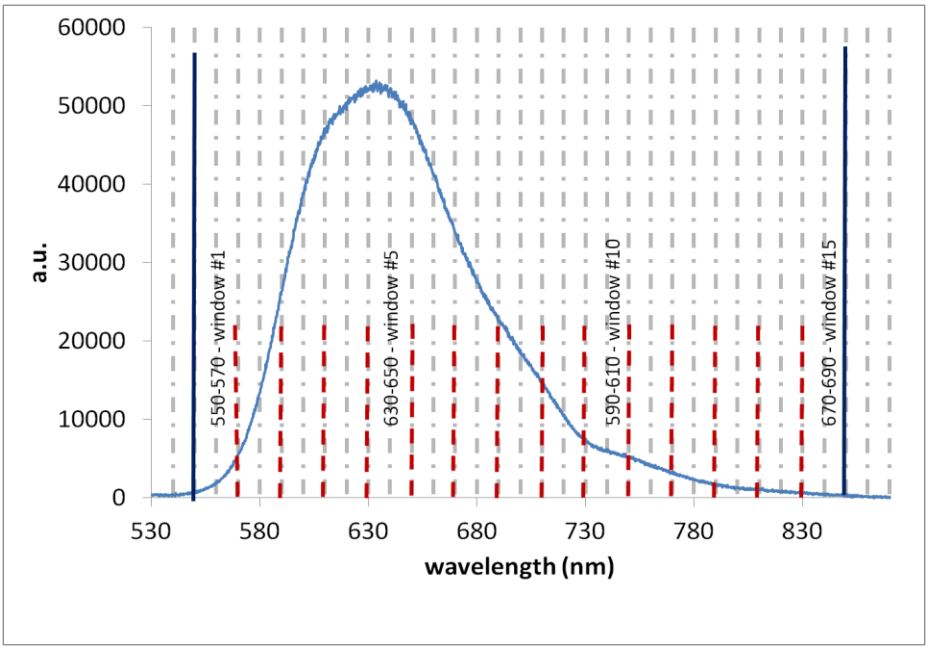

Figure 9.7, Ru(dpp) phosphorescence spectrum with fifteen 20nm windows between 550nm and 850nm

For each window, 200 points before the step change were averaged to give absolute quenched intensity value and 200 points after the step change were averaged to give absolute dequenched intensity value. The normalized standard deviations for the quenched and dequenched intensities were obtained by dividing the standard deviations of corresponding 200 sample points with corresponding absolute intensities. The change/difference in the absolute phosphorescence intensities was considered a signal and was measured for each window. The normalized standard deviation corresponding to the change in the absolute phosphorescence intensities was reckoned for each window. The reciprocal of the normalized standard deviation gave signal to noise ratio.

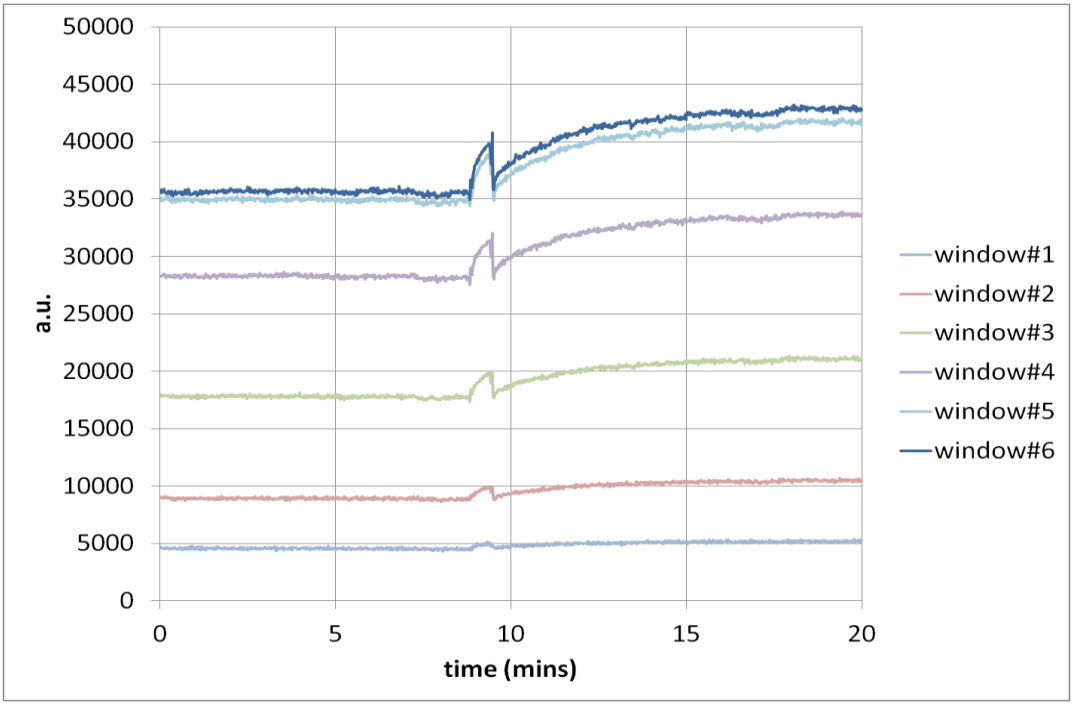

Figure 9.8, integrated values Vs time plot for six 20nm windows

Similarly all the spectra were divided in 30nm, 40nm and 50nm windows. Following the same procedure mentioned here for 20nm windows, the signal to noise ratio values for all the 30nm, 40nm and 50nm windows were calculated. Figure 9.9(a) shows the SNR values plotted at

the mid-point wavelengths of corresponding windows. For example, the SNR value shown with the diamond shaped marker at 560nm corresponds to the 20nm window from 550nm to 570nm. And the SNR value shown with the circular marker at 565nm corresponds to the 30nm window from 550nm to 580nm. A similar kind of plot for another nominally identical device was produced, which is given in figure 9.9(b).

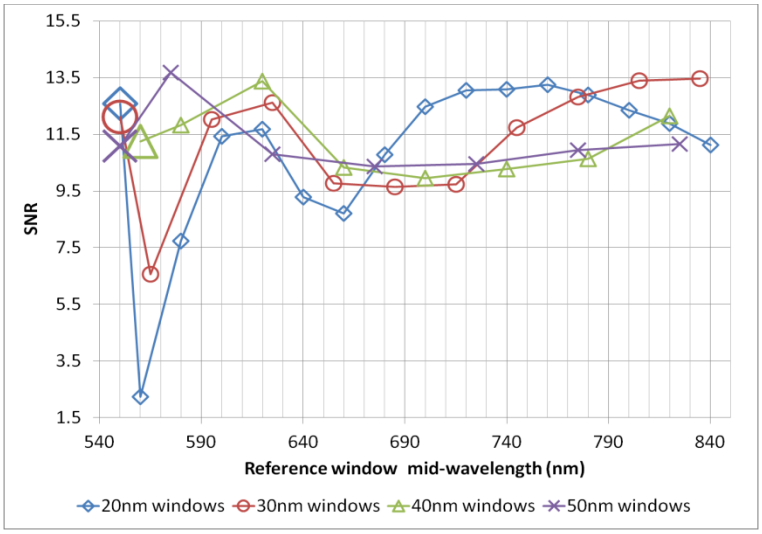

(a)

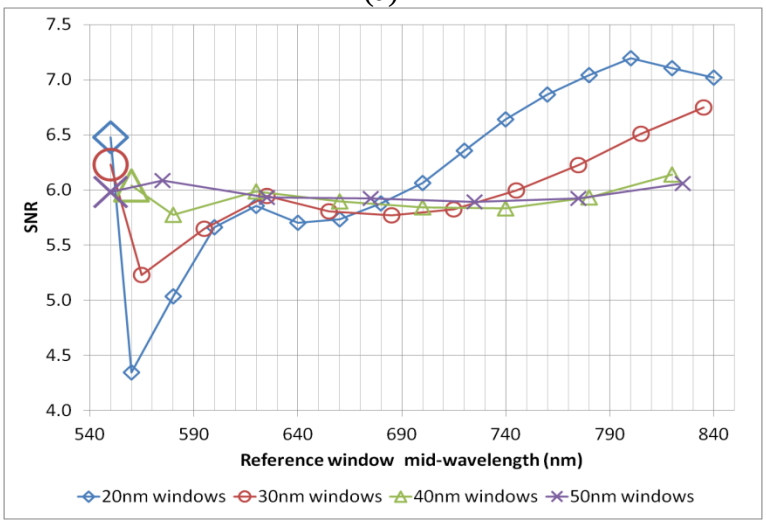

(b)

Figure 9.9, (a) SNR values corresponding to all the reference windows for device 1 (b) SNR values corresponding to all the reference windows for nominally identical device 2

The SNR values shown at 550nm are average of all SNR values for respective window widths. All window widths exhibit lowest SNR at 600nm to 650nm. It is true for both the devices. It can be explained easily by inspecting the spectrum given in figure 9.7. The spectrum shows more wiggles at the peak (600nm-640nm) than it gives at two falling edges (550nm-600nm and 640nm-700nm).

References

[1] V. Sunkara, D.-K. Park, H. Hwang, R. Chantiwas, S. A. Soper and Y.-K. Cho, "Simple room temperature bonding of thermoplastics and poly(dimethylsiloxane)," *Lab on a Chip,* vol. 11, pp. 962-965, 2011.

Chapter 10: Conclusions and future work

10.1 Conclusions

A TIR-based photoluminescence sensing device was proposed to provide a novel cost-effective, field-portable, mass-producible and low scatter enzymatic biosensor for efficient monitoring of contaminants in water, food and beverages and for industrial or bioprocess monitoring. PMMA and PDMS were selected as the most appropriate materials to fabricate such a device due to their properties such as high optical transmittance, high chemical resistance, low cost, ease of fabrication and low background fluorescence (auto-fluorescence). A PMMA-based optical waveguide core was fabricated. Novel types of acrylic molds were developed to produce PDMS-based macro-features facilitating a very simple and cost-effective architecture to support fluidics and excitation and collection fiber-optics. The PMMA core surface was modified with 3-APTES to have a self-assembled layer on it for irreversible PMMA-PDMS bonding incorporating the PMMA-based waveguide with the PDMS-based macro-features into a single device.

Several techniques of robustly depositing photoluminescent dyes on PMMA core surface were developed. Both a pH-sensitive fluorescent dye, fluoresceinamine, and an O_2-sensitive phosphorescent dye, Ru(dpp) were successfully deposited using Si-adhesive gel-based as well as HydroThane-based deposition methods. Two different types of pH-sensors using two different techniques of depositing fluoresceinamine were demonstrated. Also, the effect of concentration of fluoresceinamine-dye molecules on fluorescence intensity and scattered excitation light intensity was investigated. The fluorescence intensity to the scattered excitation light intensity ratio for dye deposition increased with dye concentration. However, both the absolute fluorescence intensity and absolute scatter intensity were found to decrease in different amounts

with increased dye concentration. The absolute fluorescence intensity decreases with increased dye concentration due to increased self-quenching of dye molecules.

An enzymatic lactose sensor ws designed and characterized using Si-adhesive gel based Ru(dpp) deposition and oxidase enzyme. The lactose sensor exhibited a linear range of up to 0.8mM, which was too small for its application in industrial process control. So, a flow cell-based sensor device with a fluid reservoir was proposed and fabricated to increase the linear range of the sensor. Also, a multi-channel pH-sensor device with four channels was designed and fabricated for simultaneous sensing of multiple analytes.

An enzymatic hydrogen peroxide sensor was made to demonstrate the usefulness of the device as an enzymatic biosensor. The O_2-sensitive phosphorescence of ruthenium based dye Ru(dpp) was used as a transduction signal and the catalase-enzyme was used as a bio-component for the sensor. The TIR-based device demonstrated a phosphorescence intensity to the scattered excitation light intensity ratio of 100.0±17.6. The hydrogen peroxide sensor exhibited the detection limit of (2.2±0.6) μM with the linear range from 0.1mM to 20mM.

The TIR-based device is made of low cost, shock resistant materials such as PMMA and PDMS using simple fabrication techniques without photolithography or etching, which makes the device cost-effective and less fragile. Also, the device is compact with 3.5cm x 2.5 cm x 0.6 cm dimensions. Thus, the plastic TIR-based photoluminescence sensing device proves to be a promising device for cost-effective and field-portable enzymatic biosensors with low detection limit and large linear range.

On the other hand, the device has some weaknesses. Firstly, the collection fiber is just held in a hole in the PDMS. Due to the elastic properties of PDMS, the collection fiber is prone to vibrations while measurements producing noisy signal. Secondly, the current design employs

a spectrometer for signal detection requiring a rather costly computer based data acquisition. Some other limiting aspects of the device can be improved to have a better device performance, which is presented in the next section.

10.2 Future work

This section overviews some aspects of the TIR-based enzymatic biosensor project that can potentially be improved in the future. Some aspects suggest improvements in the characterization of the designed device and some other suggest improvements in the design itself. All such aspects with possible improvements are discussed in this section.

The current design incorporates an asymmetric waveguide with multimode collection fiber collecting the photoluminescence at an angle normal to the waveguide surface. The collection fiber picks up the photoluminescence as well as some scattered excitation light, and how well it picks up photoluminescence over scattered excitation light depends on the collection efficiency. Collection efficiency of the collection fiber as a function of alignment angle, its distance from dye and its numerical aperture has not been investigated. So, experiments can be carried out to investigate the effect of collection angle, distance of collection fiber from dye and collection fiber's numerical aperture on collection efficiency.

The multi-channel device discussed in Chapter 9 is a multi-source device, where each channel can be excited by a different light source. The device is fabricated but a real simultaneous multi-analyte sensing using the device was not yet demonstrated. So, experiments can be done to investigate the performance of the device as a multi-analyte sensor. Channel to channel variability and inter-channel interference should be investigated as well to determine the operation of the device.

Improvements in the linear range of the lactose sensor using the flow cell based device with fluid reservoir (discussed in Chapter 9) could be investigated. So, experiments should be

done to determine the required fluid column height for optimum flow rate to get adequate O_2 replenishment rate. Then, experiments can be done to measure the performance parameters of the sensor such as detection limit and linear range.

Also, the current design of the system requires using a spectrometer for photoluminescence measurements, which necessitates a computer based data acquisition system. A self-contained hand-held device independent of computer based acquisition system can be developed by integrating the device with a photodetector, a data acquisition PCB and a display. Such a device can be very useful as field portable, economical chemical sensor or enzymatic biosensor. Also, more experiments can be done to confirm the results on wavelength dependence of quenching. Based on the results, a narrow linewidth optical filter can be integrated to choose a part of the spectrum with the highest SNR to improve the system performance. Moreover, a broadband metallic mirror can be integrated on the bottom of the PDMS lower cladding to reflect some of the photoluminescence for more collection.

The device provides an excellent platform for low excitation scatter and economical enzymatic biosensors. Therefore, the utility of the device for enzymatic biosensing of other aromatic or aliphatic chemicals can be investigated. As discussed in Chapter 4, COC exhibits very good resistance to chlorinated solvents, so a COC based device design can be used to make enzymatic biosensors for chlorinated solvents.

Thus, the TIR-based enzymatic biosensor project can be improved and investigated in many aspects in future as discussed in this section.

Appendix A: Device fabrication

A.1 Fabrication of acrylic molds for cladding (for device design type-I)

- Obtain PMMA slabs of dimensions 5mm x 15mm (for fluid cell), 15mm x 25mm (waveguide core socket), 1mm x 6mm (fiber groove), and 25mm x 31mm (base, 2 such slabs) by laser cutting them to size using CO_2 laser from 0.090" thick PMMA sheet by commercial plastic vendor (e.g., Fort Collins Plastics)
- Apply transparent tape on bottom surface of both 25mm x 31mm base-slabs
- Draft 5mm x 15mm rectangle on the tape of one of the base-slabs
- Use this rectangle as a blueprint and place the 5mm x 15mm PMMA slab on the un-tapped surface of the base-slab
- Using pipette, apply 20µl of WeldOn -3 liquid (acrylic cement) to one of the bottom edges of the 5mm x 15mm slab. The cement will spread over the entire interface due to capillary action
- Keep it at room temperature for 30minutes and then remove the tape from the bottom surface before a mold for PDMS upper cladding is ready to use
- Draft a blue print for waveguide core socket and fiber groove on the tape of the other base-slab
- Use this blueprint and place the 15mm x 25mm and 1mm x 6mm slabs on the un-tapped surface of the other base-slab
- Apply about 10µl of WeldOn – 3 liquid on each edge of both the slabs.
- Keep it at room temperature for 30minutes and then remove the tape from the bottom surface before a mold for PDMS upper cladding is ready to use

A.2 Molding the PDMS claddings

- Place the molds for PDMS upper cladding and lower cladding in a petri dish. Multiple molds can be put in a single dish to reduce PDMS waste and to produce multiple chips in one batch. Rectangular/square petri dish is recommended to reduce PDMS waste
- Prepare 10:1 mixture of PDMS base and curing agent
- Pour the mixture in the petri dish to fill it to the brim
- Keep the petri dish at room temperature for 24 hours for curing
- Using a razor blade and a needle, separate the cured PDMS from the petri dish
- Using the edges of the base-slabs of the molds as guide, cut the cured PDMS slabs by razor blade
- Peel the cured cut to size PDMS slabs off the molds
- Draft the blueprint of the fluid cell on a paper. Include circles representing inlet-outlet holes near two ends and collection fiber hole in the center
- Place the cured PDMS upper cladding slab on the blueprint and accordingly punch the holes in the slab using hollow punching tubes
- PDMS upper cladding and PDMS lower cladding slabs are ready to use

A.3 Preparation of PMMA core slabs

- Cut the PMMA core slabs in 15mm x 25mm dimensions from a 0.090" thick PMMA sheet using a CO_2 laser by a commercial plastic vendor
- Prepare 5% solution of 3-APTES (3-aminopropyl triethoxysilane)
- Activate the solution by heating it at 85° C for 5 minutes

- Meanwhile, place the slabs in the plasma chamber of the Micro RIE facility. Place each slab in standing position so that both flat surfaces of each slab do not touch anywhere in the chamber
- Treat the slabs with O_2 plasma at 200W RF power, 50sccm O_2 flow rate and 50mTorr pressure for 60 seconds
- Immediately after that, dip the slabs in the activated 3-APTES solution for 2 minutes
- N_2-blow dry the slabs and bake them at 65°C for 10 minutes to stabilize the self-assembled layer of 3-APTES on the slabs

A.4 Bonding PDMS claddings with PMMA core

- Place the PMMA core slab and PDMS upper cladding slab in the Plasmaline chamber
- Treat the slabs with air corona discharge at 50W RF power and 0.9Torr air pressure for 60 seconds
- Immediately after vent, bring the treated surfaces of the slabs together in firm contact for 30 seconds to obtain irreversible bonding
- Place the upper cladding bound PMMA slab and the PDMS lower cladding slab in the plasma chamber
- Treat the slabs with air corona discharge at 50W RF power and 0.9Torr air pressure for 60 seconds
- Immediately after vent, bring the treated surfaces of the slabs together in firm contact for 30 seconds to obtain irreversible bonding
- TIR-based device is ready to use

- The highest bonding strength is achieved with time. Keeping the device at room temperature for at least 24 hours before using produces best results

A.5 Methods for depositing photoluminescent dye layers

A.5.1 Si-gel based Ru(dpp)^3 deposition

- Prepare a deposition solution by mixing
    - 200mg Si clear adhesive gel (Devcon), 0.5ml chloroform, 1mg Ru(dpp)3
- Put 3µl of deposition solution on PMMA core surface through collection fiber hole by pipette
- Keep for 3 hours at room temperature before use

A.5.2 Hydrothane-based Ru(dpp)3 deposition

- Prepare solution-A : 0.5% (w/v) Ru(dpp)3 in chloroform
- Prepare solution-B : 10% (w/v) HydroThane in toluene
- Prepare a deposition conjugate by mixing solution-A and solution-B in 1:1 proportions
- Put 3µl of deposition conjugate on PMMA core surface through collection fiber hole by pipette
- Keep for 30 minutes at room temperature before use

A.5.3 Si-gel based fluoresceinamine deposition

- Prepare solution-A : 1.5% (w/v) fluoresceinamine (201626 ALDRICH) in acetone
- Prepare solution-B : 20% (w/v) Si-adhesive gel (Devcon) in chloroform
- Prepare a deposition conjugate by mixing solution-A and solution-B in 1:2 proportions
- Put 3µl of deposition conjugate on PMMA core surface through collection fiber hole by pipette
- Keep for 3 hours at room temperature before use

A.5.4 Hydrothane based fluorescenamine deposition

- Prepare solution-A : 2 % (w/v) fluoresceinamine (201626 ALDRICH) in acetone
- Prepare solution-B : 10 % (w/v) HydroThane in toluene
- Prepare a deposition conjugate by mixing solution-A and solution-B in 1:2 proportions
- Put 3µl of deposition conjugate on PMMA core surface through collection fiber hole by pipette
- Keep for 30 minutes at room temperature before use

A.6 Deposition protocols for enzymes

A.6.1 Deposition protocol for catalase

- Prepare a deposition solution by mixing
    - 5µl of catalase enzyme, 45 µl of BSA (56mg/ml - bovine serum albumin A9418 SIGMA), 1.19 µl of glycerol and 25 µl of 2.5% gluteraldehyde
- Put 1.5µl of deposition solution on deposited dye layer
- Keep for 30 minutes at room temperature before use

A.6.2 Deposition protocol for lactose oxidase

- Prepare a deposition solution by mixing
    - 20 µl Lox [100 mg/mL], 30 µl BSA [160mg/mL], 1.19 µl glycerol, 25 µl 2.5% gluteraldehyde
- Put 1.5µl of deposition solution on deposited dye layer
- Keep for 30 minutes at room temperature before use